

X-ray emission from laser-produced plasmas

DANILO GIULIETTI⁽¹⁾(*) and LEONIDA A. GIZZI⁽²⁾(**)

⁽¹⁾ Dipartimento di Fisica, Università di Pisa
Piazza Torricelli 2, 56100 Pisa, Italy

⁽²⁾ Istituto di Fisica Atomica e Molecolare, Consiglio Nazionale delle Ricerche
Via del Giardino 7, 56100 Pisa, Italy

(ricevuto il 22 Gennaio 1998)

3	1.	Introduction
4	2.	Laser-produced plasmas
4	2'1.	Basic concepts
6	2'2.	Semi-analytical modelling of laser plasmas
8	2'3.	Hydrodynamic simulations
8	2'3.1.	Lagrangian coordinates
9	2'3.2.	Modelling long-scalelength laser-plasma experiments
11	3.	Laser-plasma interactions
11	3'1.	Absorption mechanisms
11	3'1.1.	Inverse bremsstrahlung absorption
12	3'1.2.	Ion turbulence absorption
12	3'1.3.	Resonance absorption
13	3'1.4.	Brunel effect
13	3'2.	Parametric instabilities
14	3'2.1.	Stimulated Brillouin scattering (SBS)
14	3'2.2.	Stimulated Raman scattering (SRS)
15	3'2.3.	Two-plasmon decay (TPD)
16	3'2.4.	Filamentation
17	3'2.5.	Surface plasma waves (SPW)
18	3'2.6.	Hot electrons
20	3'3.	Femtosecond interactions
20	3'3.1.	Basic features of femtosecond interactions
22	3'3.2.	Propagation of laser light in overdense plasmas

(*) giulietti@dfi.unipi.it

(**) leo@risc.ifam.pi.cnr.it

- 22 4. X-ray emission from laser plasmas
- 22 4.1. Fundamental emission processes
 - 23 4.1.1. Bremsstrahlung
 - 24 4.1.2. Recombination
 - 25 4.1.3. Lines
- 27 4.2. Radiation transport in plasmas
 - 27 4.2.1. Basic definitions
 - 28 4.2.2. Limit approximations: thin and thick plasmas
- 28 4.3. Equilibria in laser-produced plasmas
 - 29 4.3.1. Thermal equilibrium (TE)
 - 30 4.3.2. Local thermal equilibrium (LTE)
 - 31 4.3.3. Non-LTE plasmas
 - 31 4.3.4. Coronal equilibrium (CE)
 - 33 4.3.5. Collisional-radiative equilibrium (CRE)
- 33 4.4. Atomic physics: temporal scale and related calculations
 - 33 4.4.1. Limits of the steady-state approximation
 - 34 4.4.2. Transient ionisation in Al plasmas
 - 36 4.4.3. Transient ionisation in low-Z plasmas
- 36 4.5. Characteristics of laser-plasma X-ray sources
 - 37 4.5.1. Spectral distribution
 - 40 4.5.2. X-ray pulse duration
 - 42 4.5.3. Source size and angular distribution
 - 43 4.5.4. X-ray conversion efficiency
- 48 4.6. X-ray emission in ultra-short pulse interactions
 - 48 4.6.1. Femtosecond X-ray sources
 - 49 4.6.2. High harmonics generation
- 52 4.7. X-ray lasers
 - 52 4.7.1. Motivation
 - 52 4.7.2. Basic principles
 - 53 4.7.3. Pumping schemes
- 54 5. X-rays as plasma diagnostics
- 55 5.1. X-ray spectroscopy
 - 55 5.1.1. Spectroscopic techniques
 - 58 5.1.2. Time-resolved analysis
 - 59 5.1.3. Temperature measurements from X-ray spectra
- 62 5.2. Plasma opacity
 - 62 5.2.1. Opacity effects in temperature measurements
 - 63 5.2.2. Laser reheating of preformed plasmas
- 65 5.3. Plasma density
 - 65 5.3.1. Interferometer set up for phase shift measurements
 - 66 5.3.2. Experimental results
 - 66 5.3.3. Basic principles of time-resolved interferometry
 - 68 5.3.4. Electron density profiles
- 69 5.4. X-ray imaging of plasmas
 - 69 5.4.1. Basic X-ray imaging techniques
 - 71 5.4.2. Spectral selection in X-ray imaging
 - 71 5.4.3. Time-resolving techniques
 - 74 5.4.4. An illustrative example of fast X-ray imaging
- 76 5.5. Particles and high energy photons
 - 76 5.5.1. Ions, electrons and alpha-particles
 - 77 5.5.2. Hard X-rays and γ -rays from super-hot electrons

80	6.	Applications
80	6.1.	X-rays in science, technology and medicine
80	6.1.1.	X-ray microscopy
81	6.1.2.	Advantages of LPP X-ray sources
82	6.1.3.	Progress in the design of LPP X-ray sources
82	6.1.4.	Examples of applications of LPP X-rays
83	6.2.	Main X-ray sources
84	6.2.1.	X-ray tubes
84	6.2.2.	Synchrotron radiation
86	6.2.3.	Comparison of X-ray sources
88	7.	Conclusions

1. – Introduction

Since the first experiments on laser interaction with matter it was clear that laser-produced plasmas are bright sources of electromagnetic radiation in the X-ray spectral region. The electron density of the plasmas produced in such interactions can be as high as $\approx 10^{23}$ electrons/cm³ and temperatures of several keV can be achieved. These high values of density and temperature make laser plasmas ideal media for an efficient X-ray emission. In fact, since laser absorption is very high, the conversion efficiency of laser energy into X-ray energy can also be quite high (see [1] and references therein).

X-ray pulses produced in these conditions may have energies up to several joules, and a duration ranging between $\approx 10^{-18}$ s and $\approx 10^{-9}$ s. Therefore, the power delivered in the X-ray region in the entire solid angle ($\Omega = 4\pi$) can be as high as a few TW. In addition, the size of these X-ray sources is very small, typically of the order of the focal spot of the plasma-generating laser beam ($\phi = 10 - 100 \mu\text{m}$). The resulting brightness of these sources is considerably high, up to $10^{17} \text{W/cm}^2 \text{sr}$, with the peak spectral brightness in a 0.01% bandwidth being as high as $10^{19} \text{ph s}^{-1} \text{mm}^{-2} \text{mr}^{-2}$.

Beside being sources of thermal, incoherent X-ray emission, laser plasmas have also been recognised as media for the generation of coherent X-ray radiation. Coherent emission in the soft X-ray region can indeed be obtained either via population inversion with consequent laser emission [2] or via high order harmonics generation [3, 4]. To date, X-ray laser emission from laser plasmas has been the brightest source ever achieved in a laboratory, its peak spectral brightness in a 0.01% bandwidth being as high as $10^{23} \text{ph s}^{-1} \text{mm}^{-2} \text{mr}^{-2}$. Accessible laser emission in the X-ray spectral region is one of the more attractive goals of the scientific community due to the great impact that such an intense and coherent source of X-ray radiation can have in scientific and technological applications on a subnanometer scale. However, due to the large separation of electronic levels involved in the laser transition, the enormous power required to achieve population inversion can only be delivered by the most powerful lasers available today.

Among all the possible applications of laser-produced plasma X-rays (LPP X-rays), Inertial Confinement Fusion (ICF) is one of the most relevant. In ICF experiments, X-rays are employed not only to diagnose the physical properties of the plasma, but also to reach ignition conditions. In fact, in one of the schemes currently pursued to achieve ICF, the pellet (micro-spheres filled with deuterium and tritium) is illuminated by the X-rays produced by the interaction of laser light (or the charged-particle beams)

with the walls of a cavity made of high- Z material surrounding the pellet. On the other hand, laser-plasma X-ray sources are extensively used in a wide range of advanced scientific and technological applications including X-ray microscopy, nano-lithography, dynamic studies of mechanical properties of materials, X-ray time-resolved radiography.

The present work is devoted to the description of all the aspects mentioned above and to discussing the implications of these studies in applications requiring X-ray radiation. The following section is devoted to a brief description of the basic plasma physics concepts in view of their application to laser-produced plasmas. Simple models of laser plasmas are introduced to study their temporal evolution. A closer look at basic laser-plasma interaction mechanisms, including absorption mechanisms and laser-induced instabilities of particular relevance to X-ray emission, are presented in sect. 3. An entire section is devoted to the introduction of basic processes in laser-plasma interactions in the femtosecond regime. The properties of X-ray emission from laser plasmas are discussed in details in sect. 4 with particular attention to atomic physics processes and to plasma equilibrium conditions relevant to laser plasmas. X-ray emission from femtosecond interactions and X-ray lasers are also discussed in detail. The experimental approach to X-ray emission from laser plasmas is dealt with in great detail in sect. 5. Illustrative examples of X-ray diagnostic techniques of laser plasmas including spectroscopy and fast imaging are described and discussed. A separate section is devoted to electron density measurements due to their relevance in X-ray emission studies. Generation of particles and high-energy photons is also discussed in view of the latest findings in ultrafast interactions. Finally, an overview of present and forthcoming applications of X-rays from laser-produced plasmas is given in sect. 6, along with a comparison with other X-ray sources.

2. – Laser-produced plasmas

2.1. Basic concepts. – Laser radiation of high intensity impinging on a solid target rapidly produces a plasma on its surface. Figure 1 shows typical profiles of density, temperature and expansion velocity of the plasma generated by irradiating a solid target with a powerful, $1 \mu\text{m}$ wavelength, nanosecond laser pulse.

The propagation of laser light in the plasma is dominated by the presence of free electrons, and follows the dispersion relation

$$(2.1a) \quad \omega_L^2 = \omega_P^2 + k_L^2 c^2 .$$

In this expression, ω_L and k_L are the angular frequency and the wave number of the laser light, c is the speed of light in the vacuum and

$$(2.1.b) \quad \omega_P = \sqrt{4\pi n_e e^2/m}$$

is the plasma frequency, e and m being the charge and the mass of the electron respectively and n_e the plasma electron density. The group velocity $v_g = c(1 - \omega_P^2/\omega_L^2)^{1/2}$ decreases as the electron density increases, down to the limit value $v_g = 0$, at the critical density $n_c = m\omega_L^2/4\pi e^2 = 1.1 \times 10^{21} \lambda_L^{-2} (\mu\text{m}) \text{ cm}^{-3}$. Basically laser light cannot propagate at densities $n_e > n_c$ and consequently the interaction develops in the underdense plasma, while the light wave becomes evanescent in the overdense region.

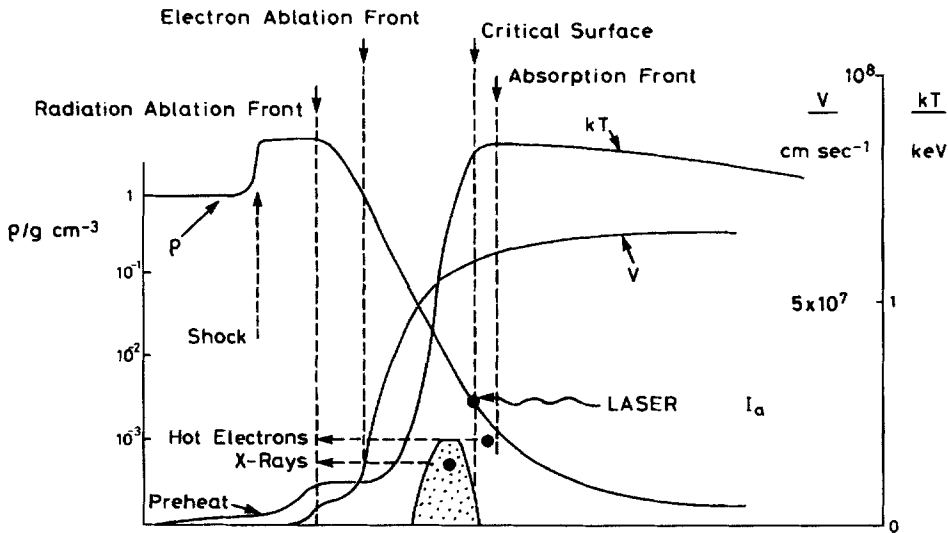


Fig. 1. – Typical temperature, density and expansion velocity profiles of a plasma generated by irradiation of a solid target by a nanosecond laser pulse focused on target at an irradiance of 10^{14} W/cm^2 [5].

An estimate of the temperature of laser-produced plasmas can be obtained by equating the absorbed laser intensity I_{abs} to the electron heat flux

$$I_{\text{abs}} \approx f \left(\frac{k_B T_e}{m} \right)^{1/2} n_e k_B T_e,$$

where T_e is the electron temperature, k_B is the Boltzmann constant and $f < 1$ is the “flux limiter” parameter (see subsect. 2.3.1) that accounts for flux inhibition effects due to deviations from the classical Spitzer description of heat conduction [6]. Solving for the temperature gives

$$(2.2) \quad T_e \approx \left(\frac{I_{\text{abs}}}{f n_e} \right)^{2/3} \frac{m^{1/3}}{k_B} \approx 3 \times 10^7 \left(\frac{I_{\text{abs}} (\text{W/cm}^2)}{f n_e} \right)^{2/3} \text{ eV},$$

that for typical parameters $I_{\text{abs}} = 10^{13} \text{ W/cm}^2$, $f = 0.1$, $n_e = 10^{21} \text{ cm}^{-3}$, gives $T_e = 0.6 \text{ keV}$. This simple model does not include energy loss mechanism like radiation emission and plasma expansion. Therefore, eq. (2.2) tends to overestimate the electron temperature.

The plasma produced by the impinging laser radiation develops and expands in the vacuum. The blow-off velocity is roughly equal to the local sound speed

$$(2.3) \quad v \approx c_s = \sqrt{\frac{3 k_B T_i + Z k_B T_e}{M}},$$

where T_i , Z and M are the ion temperature, the charge number, the mass of the ion, respectively. Typical values for the blow-off velocity range between 10^7 and 10^8 cm/s . For relatively short laser pulses, provided that the laser focal spot is not too small, the

expansion velocity determines the longitudinal (perpendicular to the target surface) density scale length of the plasma produced. In the general case, such a scalelength is given by $L_n \equiv n_e / \nabla n_e \approx \min [c_s \tau, \phi]$, where τ and ϕ are the laser pulse length and the focal spot diameter on the target, respectively. The temperature scalelength $L_T \equiv T_e / \nabla T_e$ is very long for $n_e < n_c$, due to the high electron thermal conduction in the underdense, hot plasma. However when plasmas are produced by interaction with massive solid targets the temperature scalelength is extremely short in the overdense region behind the critical density where a cooler plasma is in contact with the solid target material.

The basic parameter that characterises the plasma (collective) behaviour of an ensemble of ions and electrons is the Debye screening length

$$(2.4) \quad \lambda_D \equiv \left(\frac{k_B T_e}{4\pi n_e e^2} \right)^{1/2} = \left(\frac{v_{th}}{\omega_p} \right)^{1/2} \approx 7.43 \times 10^2 \left(\frac{T_e(\text{eV})}{n_e} \right)^{1/2} \text{cm},$$

where $v_{th} = (k_B T_e / m)^{1/2} \approx 4.19 \times 10^7 (T_e(\text{eV}))^{1/2}$ cm/s is the thermal electron velocity. This parameter gives a measure of the range of action of the electric field of an individual charged-particle in the plasma, and sets a lower limit to the scalelength of a given electron density perturbation. The basic conditions for the existence of a collective behaviour are that $\lambda_D \ll L$, where L is the typical macroscopic size of the particle ensemble and that the number of particles in the Debye sphere is very high, i.e. $N_D \gg 1$, where

$$(2.5) \quad N_D = \frac{4}{3} \pi \lambda_D^3 n_e = 1.72 \times 10^9 (T_e^{\text{eV}})^{3/2} n_e^{-1/2}.$$

As a consequence of these conditions, plasma waves with a wave vector k can exist in the plasma provided that $k\lambda_D \ll 1$. Finally, the degree of coupling of the electrons in a plasma is given by the parameter

$$(2.6) \quad \Gamma = \frac{e^2 n_e^{1/3}}{k_B T_e} = 1.4 \times 10^{-7} \frac{n_e^{1/3}}{T_e(\text{eV})},$$

that is, by the ratio between the Coulomb potential energy e^2/r at the average inter-particle distance $r = n_e^{-1/3}$ and the mean thermal kinetic energy $k_B T_e$. As an example we consider the case of a plasma of interest as an X-ray source with an electron density $n_e = 10^{21} \text{ cm}^{-3}$ and an electron temperature $T_e = 500 \text{ eV}$. In these conditions the Debye screening length is $\lambda_D = 50 \text{ \AA}$, the number of particles in the Debye sphere is $N_D = 600$, and $\Gamma \approx 3 \times 10^{-3}$. Typical plasma collective phenomena are expected in such conditions while, since the coupling parameter is small, the electron gas can be treated within the ideal gas approximation.

2.2. Semi-analytical modelling of laser plasmas. – The kind of plasma produced by focusing a laser pulse on a given target can be predicted by different types of numerical simulations. However, analytical or semi-analytical models based on very simple physical assumptions have also been developed which describe plasma formation and hydrodynamic expansion. These models allow to quickly get the parameters of the plasma in given geometrical and physical interaction conditions.

A simple analytical hydrodynamic model of laser-heated exploding foils [7] has been developed which predicts the conditions of the plasma (temperature, density, scale

length, etc.), for a given set of experimental parameters (laser intensity, laser pulse duration, target thickness and target composition, etc.). The model assumes inverse bremsstrahlung as the dominant mechanism of absorption of the impinging laser radiation and is based on a self-similar solution of single fluid, ideal hydrodynamic equations that describe the isothermal, homogeneous expansion of a plasma in plane-parallel geometry. The laser pulse is assumed to be flat-top, *i.e.* with constant intensity for the entire pulse duration t_L . The spatial solution for the plasma mass density is found to be

$$(2.7) \quad \rho = \frac{m}{L\sqrt{2\pi}} \exp\left[-\frac{x^2}{2L^2}\right]$$

m being the column density of the foil and L the time-dependent scale length, defined by the relation $v = x(\partial L/\partial t)/L$. Analytical solutions of the self-similar equations, as useful scaling laws for the plasma variables can be derived for three distinct temporal intervals marked by two characteristic times, *i.e.* the laser pulse duration t_L and the transparency time t_{trans} , *i.e.* the time at which the inverse bremsstrahlung optical depth through the foil is equal to one. After a time of the order of the target sound crossing time at the initial temperature, up to $t < t_{\text{trans}}$, the following power law functions describe the main plasma variables:

$$T = 11.1 \times \left(\frac{IAt}{mZ} \right) \text{ keV}, \quad L = 6.67 \times 10^{-2} \left(\frac{I^{1/2}t^{3/2}}{m^{1/2}} \right) \text{ cm},$$

$$n_{e,\text{max}} = 1.12 \times 10^{20} \left(\frac{m^{3/2}Z}{I^{1/2}At^{3/2}} \right) \text{ cm}^{-3},$$

where $n_{e,\text{max}}$ is the maximum value of the electron density distribution, I is the laser intensity in units of 10^{14} W/cm^2 , A the atomic number normalised to 80, Z the average charge per ion normalised to 25, t is the time from the beginning of the pulse normalised to 1ns and m is the foil column density normalised to 10^{-4} g/cm^2 . Also the inverse bremsstrahlung optical depth τ_{ib} and the transparency time can be expressed as power laws

$$\tau_{\text{ib}} = 9.52 \times 10^{-3} \left(\frac{\lambda^2 m^2 Z^3 \Lambda}{A^2 T^{3/2} L} \right), \quad t_{\text{trans}} = 1.57 \times 10^{-1} \left(\frac{\lambda^{2/3} m^{4/3} Z^{3/2} \Lambda^{1/3}}{I^{2/3} A^{7/6}} \right) \text{ ns},$$

where λ is the laser wavelength normalised to $0.53 \mu\text{m}$, *i.e.* the frequency doubled Nd:Yag laser wavelength. The temperature at the transparency time is given by

$$T_{\text{trans}} = 1.74 \left(\frac{I^{1/3} \lambda^{2/3} m^{1/3} Z^{1/2} \Lambda^{1/3}}{A^{1/6}} \right) \text{ keV},$$

where Λ is the Coulomb logarithm normalised to 5. For times $t_{\text{trans}} < t < t_L$ the temperature remains constant at T_{trans} , while the scalelength and the density are given by

$$L = 4.20 \times 10^{-2} \left(\frac{I^{1/3} \lambda^{1/6} Z^{3/8} \Lambda^{1/12} t^{5/4}}{m^{1/6} A^{7/24}} \right) \text{ cm},$$

$$n_e = 1.78 \times 10^{20} \left(\frac{m^{7/6} Z^{5/8}}{I^{1/3} \lambda^{1/6} A^{17/24} \Lambda^{1/12} t^{5/4}} \right) \text{cm}^{-3}.$$

Finally, after the laser is turned off, *i.e.* for $t > t_L$, the foil continues to expand according to the following laws:

$$T = T_{\text{trans}} \left(\frac{t_L}{t} \right)^{2/3}, \quad L = 4.20 \times 10^{-2} \left(\frac{I^{1/3} \lambda^{1/6} Z^{3/8} \Lambda^{1/12} t_L^{1/4} t}{m^{1/6} A^{7/24}} \right) \text{cm},$$

$$n_e = 1.78 \times 10^{20} \left(\frac{m^{7/6} Z^{5/8}}{I^{1/3} \lambda^{1/6} A^{17/24} \Lambda^{1/12} t_L^{1/4} t} \right) \text{cm}^{-3}.$$

We note that the model relies on the isothermal and linear velocity approximations and therefore it is not expected to be valid at very early times, but only for times longer than t_{trans} . In addition, two-dimensional effects may be important in particular circumstances thus invalidating the basic assumptions of the model when the scale length equals or exceeds the width of the laser spot, W . Finally, at very high laser intensities, several laser-plasma instabilities set in, which may play an important role in the interaction.

2.3. Hydrodynamic simulations. – A more detailed description of laser-plasma interactions can be obtained by means of numerical simulation. Once suitable approximations have been made, the set of differential equations that describe the motion of plasma can be solved numerically and the main properties of the plasma can be calculated and compared with the experimental ones. The one-dimensional Lagrangian code MEDUSA [8, 9] will be briefly described here and examples of simulations of real experiments will be given to describe the benefits and the limits of this approach.

2.3.1. Lagrangian coordinates. In a hydrodynamic simulation code the plasma is usually described as a two component (electrons and ions) fluid characterised by four main variables, the plasma mass density $\varrho(x, t)$, the fluid velocity $u(x, t)$, the electron temperature $T_e(x, t)$, and the ion temperature $T_i(x, t)$. For the specific purpose of describing laser plasmas, ions behave as a perfect gas, while electrons are described either by an ideal gas equation of state (EOS) or by a Thomas-Fermi EOS. For plasmas produced by relatively long pulses (up to a few nanosecond), a perfect gas EOS satisfactorily models the generated plasma. In contrast, in the case of shorter laser pulses (down to a few picoseconds), a non-ideal electron gas EOS based on the Thomas-Fermi model can be used and degeneracy effects should also be taken into account. Charge neutrality requires that the electron fluid and the ion fluid share the same velocity. In this case, neglecting internal electric and magnetic fields, the equation of motion becomes

$$\varrho \frac{du}{dt} = - \frac{dp}{dx},$$

where ϱ is the mass density and $p = p_i + p_e$ is the hydrodynamic pressure. Each subsystem is also governed by an *energy equation* which is obtained by balancing the rate at which laser energy enters the subsystem and the rate at which this energy goes

into modifications of the thermodynamic and kinetic state according to

$$(2.8) \quad C_V \frac{dT}{dt} + B_T \frac{d\varrho}{dt} + p \frac{dV}{dt} = S ,$$

where S is the rate of energy input per unit mass, $C_V = (\partial U / \partial T)_\varrho$ is the specific heat per unit volume, $B_T = (\partial U / \partial \varrho)_T$ describes the variation of the internal energy due to the interaction between particles within the same subsystem, and $U = pV/(\gamma - 1)$ is the internal energy per unit mass. Electrons can exchange energy via thermal conduction, electron-ion collisions, bremsstrahlung emission and absorption, while ions exchange energy via thermal conduction, electron-ion collisions, and viscous shock heating. Energy is exchanged between ions and electrons by means of electron-ion collisions rate. Inverse bremsstrahlung absorption of laser light is modelled using classical coefficients (see subsect. 3'1.1). The thermal conductivity is modelled in terms of the classical [6] conductivity. The heat flux is limited, for high temperature gradients, to the so-called free-streaming limit, $F_{e,\max} = f v_{th} n_e k_B T_e$, according to the expression $F_{e,\text{limited}} = (F_e^{-1} + F_{e,\max}^{-1})^{-1}$ where f is the flux limiter parameter ($f < 1$). The electron heat flux, according to the usual definition, is proportional to the electron temperature gradient, *i.e.* $F_e = \kappa_{SH} \nabla T_e$, where κ_{SH} is the Spitzer-Härm conductivity.

2'3.2. Modelling long-scalelength laser plasma experiments. In the simulation code, a target can be specified by giving atomic number, atomic mass, mass density, thickness and boundary conditions. Laser pulse parameters can be specified including wavelength, intensity, pulse length, temporal shape and timing relative to the start time of the hydrodynamic simulation.

Many physical processes can be accounted for and controlled by means of other input logical switches including resonance absorption (see subsect. 3'1.3), hot electrons and ponderomotive force effects. The ionisation equilibrium can be calculated by the code using Saha ionisation model.

As an illustrative example, we now consider an experiment [10, 11] in which the plasma is pre-formed by irradiating a target consisting of a small disk of aluminium (400 μm diameter, 500 nm thick). Four laser beams (600 ps FWHM, 1.053 μm wavelength) are superimposed on the target, two on each side of the disk, focused in a 600 μm diameter focal spot. In such a configuration the irradiation geometry is symmetric with respect to the plane of the target. Therefore simulations can be performed by keeping fixed the rear boundary of the target and assuming a single-side irradiation, with a target thickness equal to half of the original thickness.

The code predicts the temporal evolution of the main hydrodynamic variables including electron and ion temperature, mass density, hydrodynamic velocity and pressure and average ionisation relative to each cell in which the plasma is spatially sampled according to the numerical implementation of the Lagrangian scheme. Radiation losses due to bremsstrahlung emission are also accounted for although, for low- and medium- Z plasma, they are usually negligible.

Our attention is focused on the plasma formation, heating and initial stage of cooling, when intense X-ray emission occurs and can be investigated experimentally by means of X-ray spectroscopy as described in the following sections. Figure 2 shows the results of the simulations in terms of the electron temperature and density profiles in eV and cm^{-3} , respectively, at the peak of the heating laser pulses. Taking into account that the critical density at 1.053 μm is $n_{cr} \cong 10^{21} \text{ cm}^{-3}$, fig. 2 shows that,

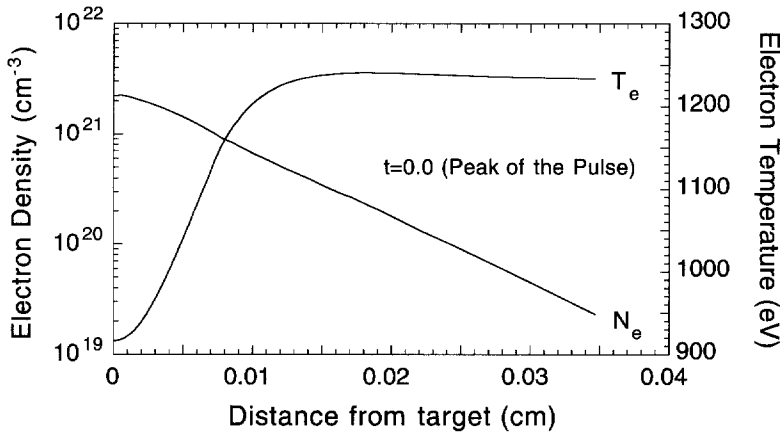


Fig. 2. – Electron density and temperature profiles obtained from the hydrodynamic simulation at the peak of the heating laser pulse. A 250 nm thick Al target is irradiated at a wavelength of $1.053 \mu\text{m}$ and at an intensity of $3 \times 10^{13} \text{ W/cm}^2$. The electron conductivity is limited to 10% of the free streaming value.

at the peak of the pulse, the plasma is still overdense over a $50 \mu\text{m}$ long plasma column.

The electron temperature is uniform over the subcritical region, where it is expected to be greater than 1.2 keV, decreasing to approximately 0.9 keV into the higher-density region, where laser light cannot propagate. Figure 3 shows the electron temperature and density profiles calculated using the same conditions as in fig. 2 but relative to later times, *i.e.* 2.2 ns, 3.0 ns and 4.3 ns after the peak of the heating pulse.

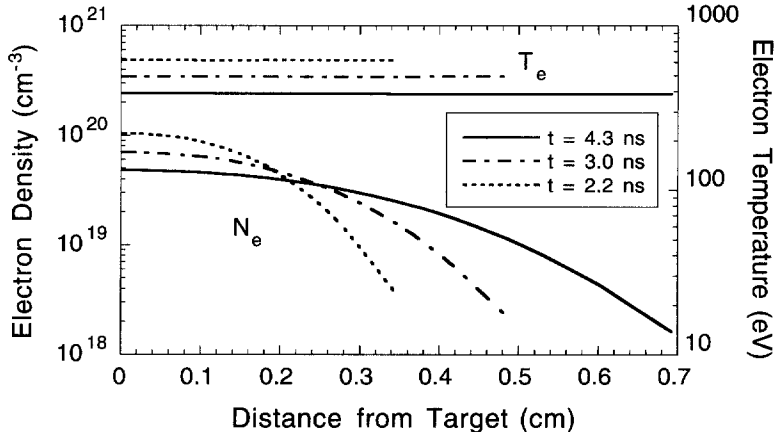


Fig. 3. – Electron density and temperature profiles obtained from the same simulation of fig. 2 at three different times after the peak of the heating laser pulse. A 250 nm thick Al disk target is irradiated at a wavelength of $1.053 \mu\text{m}$ and at an intensity of $3 \times 10^{13} \text{ W/cm}^2$.

Approximately 2 ns after the peak of the heating pulse the plasma is fully underdense, the peak density being approximately $n_{\text{cr}}/10$ and the electron temperature, uniform over the whole plasma, being approximately 600 eV.

3. – Laser-plasma interactions

3.1. Absorption mechanisms. – As laser light propagates in the plasma, several mechanisms can account for transfer of energy from the e.m. wave to the plasma, according to the interaction regime.

3.1.1. Inverse bremsstrahlung absorption. The electrons, while oscillating under the action of the laser electric field, collide with the ions giving rise to transfer of electromagnetic energy to the plasma. The fraction of absorbed laser energy after a propagation over a distance L in a uniform plasma is given by

$$(3.1) \quad \alpha_{\text{abs}} = 1 - \exp[-k_{\text{ib}}L],$$

where

$$(3.2) \quad k_{\text{ib}} = 3.10 \times 10^{-7} Z n_e^2 \ln \Lambda \omega_L^{-2} \left[1 - \left(\frac{\omega_p}{\omega_L} \right)^2 \right]^{-1/2} (T_e(\text{eV}))^{-3/2} \text{ cm}^{-1}$$

is the inverse bremsstrahlung coefficient, *i.e.* the imaginary part of the laser wave vector k , and $\ln \Lambda$ is the Coulomb logarithm for electron-ion collisions which, for $T_i m_e / m_i < 10 Z^2 \text{ eV} < T_e$ is given by $\ln \Lambda \approx 24 - \ln(n_e^{1/2} / T_e(\text{eV}))$.

It is clear from eq. (3.2) that collisional absorption is higher for lower temperatures, higher densities, higher- Z plasmas. Consequently, in the case of interaction with inhomogeneous plasmas (see fig. 1) most of the absorption takes place in the proximity of the critical density n_c , provided that the density scalelength is not too short. In fact, several processes can lead to shortening of the density profile near n_c (steepening), thus strongly reducing inverse Bremsstrahlung absorption [12]. On the other hand, for sufficiently large scalelengths, strong absorption may occur in the well underdense plasma ($n_e \ll n_c$) preventing laser energy from reaching the critical density layer.

At high laser intensities the electron-ion collision frequency is dominated by the oscillatory motion of the electrons in the laser electric field. In fact, the effective electron velocity is in this case given by

$$v_{\text{eff}} = \sqrt{v_{\text{th}}^2 + (eE_L/m\omega_L)^2},$$

where E_L is the laser electric field. Due to the strong dependence of the cross-section of electron-ion collisions on the electron velocity, $\sigma_{ei} \approx 4\pi Z^2 e^4 m^{-2} v_{\text{th}}^{-4}$, the inverse bremsstrahlung coefficient reduces to the effective value

$$(3.3) \quad k_{\text{ib}}^{\text{eff}} = k_{\text{ib}} \left[1 + \frac{3}{2} \left(\frac{v_q}{v_{\text{th}}} \right)^2 \right]^{-1}$$

where $v_q = eE_L/m\omega_L \approx 25\lambda(\mu\text{m}) \sqrt{I(\text{W/cm}^2)} \text{ cm/s}$ is the electron quiver velocity.

An additional cause of reduction of collisional absorption is the deviation from the Maxwellian electron distribution that occurs at high laser irradiances [13]. In fact,

when the rate of the energy gain of an electron from the laser field ($\approx \nu_{ei} v_q^2$) is larger than the rate at which electrons can share energy with each other ($\approx \nu_{ee} v_{th}^2$) to form a Maxwellian, there is a lack of low-energy electrons in the distribution compared with the case of a Maxwellian. Since low-velocity electrons are mainly responsible for collisional processes, collisional absorption is consequently reduced. This condition can be expressed by the following relation:

$$(3.4) \quad Z \left(\frac{v_q}{v_{th}} \right)^2 > 1$$

where $\nu_{ei} = 3 \times 10^{-6} Z n_e \ln \Lambda(T_e(\text{eV}))^{-3/2} \text{s}^{-1}$ and $\nu_{ee} \approx \nu_{ei}/Z$ are the electron-ion and the electron-electron collision frequency, respectively.

The equations given above can be used to estimate the expected absorption for a given set of interaction parameters including laser wavelength, pulse length and intensity and plasma charge state, provided that other plasma parameters like density, temperature and their scalelength are introduced self-consistently. In general, this can only be done by numerical hydrodynamic simulations. In particular cases like long scalelength plasmas, inverse bremsstrahlung absorption can be easily estimated and measured as discussed in subsect. 5.4.4.

3.1.2. Ion turbulence absorption. The inverse bremsstrahlung absorption coefficient reported in subsect. 3.1.1 has been evaluated assuming a completely random ion motion. However, it has been shown [14] that in the case of correlated motion of the ions, the absorption coefficient can increase significantly. Considering a coherent ion turbulence with a fluctuation spectrum $\delta n_i(k)$, the energy damping rate of laser radiation becomes

$$(3.5) \quad v_{\text{eff}} = \frac{\omega_L}{2} \sum_{\vec{k}} \left(\frac{\delta n_i(\vec{k})}{n_c} \right)^2 \text{Im} \left[\frac{1}{\epsilon(\vec{k}, \omega_L)} \right] \cos^2(\theta_i),$$

where θ_i is the angle between the wave vector \vec{k} and the laser electric field \vec{E}_L , and $\epsilon(\vec{k}, \omega_L)$ is the complex dielectric constant of the plasma. In the case of short ($\tau < 100 \text{ ps}$) pulse experiment and under ideal conditions, ion-acoustic fluctuations can cause an increase of the absorption up to 20%. For long pulse experiments, low-Z targets and $\lambda_L > 1 \mu\text{m}$, ion turbulence absorption can exceed inverse bremsstrahlung.

3.1.3. Resonance absorption. Laser radiation obliquely incident on a plasma and with a component of the electric field in the plane of incidence ($\vec{E}_L \cdot \vec{\nabla} n_e \neq 0$) can excite resonant longitudinal plasma oscillations at critical density surface. The damping of the excited electron waves leads to conversion of electromagnetic laser energy into thermal energy. The turning point for a light wave impinging on a plasma density gradient at an incident angle θ , occurs at a density n_e^{tp} given by the classical theory

$$(3.6) \quad n_e^{\text{tp}}(\theta) = n_c \cos^2(\theta).$$

Therefore, the component of laser electric field parallel to the density gradient has to tunnel through the plasma to reach the critical density region and drive resonantly electron plasma waves. Consequently, there is an optimum angle of incidence that maximises the absorption. In fact, for $\theta \rightarrow \pi/2$ the electromagnetic wave has to tunnel

through a too large distance and the plasma wave is not driven efficiently. On the other hand, for $\theta \rightarrow 0$ the component of laser electric field parallel to the density gradient vanishes and once again the electron wave is not driven efficiently. It can be shown that [15] the resonance absorption coefficient maximises at $\approx 50\%$ for an angle of incidence given by $\sin(\theta) \approx 0.8(\omega_L L/c)^{-1/3}$, where L is the density scalelength and ω_L is the laser angular frequency.

There is a simple way to show the dependence of the resonance absorption on laser polarisation and turning point position. By expressing the plasma dielectric constant in terms of the electron density,

$$(3.7) \quad \epsilon = 1 - \left(\frac{\omega_P}{\omega_L} \right)^2 = 1 - \frac{n_e}{n_c}$$

the Poisson equation in a plasma, $\vec{\nabla} \cdot (\epsilon \vec{E}) = 0$, can be written as follows:

$$\vec{\nabla} \cdot \vec{E} = - \frac{\vec{\nabla} \epsilon \cdot \vec{E}}{\epsilon} = \frac{\vec{\nabla} n_e \cdot \vec{E}}{n_c - n_e} .$$

On the other hand $\vec{\nabla} \cdot \vec{E} = -4\pi e \delta n_e$, where δn_e is the electron density perturbation of the plasma wave. By equating the right member of the two last equations, we have

$$(3.8) \quad \delta n_e = \frac{\vec{\nabla} n_e \cdot \vec{E}}{4\pi e(n_e - n_c)} .$$

The last equation shows in particular that “s” polarised laser radiation, for which $\vec{\nabla} n_e \cdot \vec{E} = 0$, cannot drive Langmuir waves, while for “p” polarised radiation, for which $\vec{\nabla} n_e \cdot \vec{E} \neq 0$, the electron density perturbation of the plasma wave increases when the critical density is approached.

3.1.4. Brunel effect. Very intense laser radiation, obliquely incident on a metallic surface or a sharply bounded overdense plasma, pulls electrons into the vacuum and drives them back into the plasma with a velocity $v_q = eE_L/m\omega_L$. Since the electric field inside the plasma is zero, one can see that a large part of the kinetic energy acquired by the electrons in the vacuum is lost when electrons re-enter the plasma [16]. This mechanism is more efficient than the usual resonance absorption for $v_q/\omega > L$, L being the density scalelength. Since the absorption due to the Brunel effect is proportional to v_q/c , it plays an important role at relativistic laser intensity and is of particular interest in femtosecond interactions where sharply bounded plasmas may be achieved.

3.2. Parametric instabilities. – When laser light propagates over a long region of underdense plasma with $L \gg \lambda_L$, many physical processes can take place, which may produce electron and ion plasma waves and scatter laser light. The damping of these waves produces plasma heating, while the scattering reduces laser absorption in the plasma. In addition, self-focusing and filamentation may give rise to local enhancement of the laser intensity, making it easier to achieve instability threshold conditions. In the following, we briefly report the main conclusions relative to the most important instabilities occurring in laser-plasma interactions, with particular attention to matching conditions and laser intensity thresholds.

3.2.1. Stimulated Brillouin scattering (SBS). Laser radiation propagating in long scalelength, underdense plasmas produces a transverse current $\vec{J} \propto \delta n \vec{E}$, acting on an initial low-frequency density perturbation δn . A reflected light wave is generated which, interfering with the incident light, produces a variation in the wave pressure, $\vec{\nabla}(\vec{E}_L \cdot \vec{E}_B)/4\pi$, which can in turn reinforce the density perturbation. This feed-back loop gives rise to an instability, provided that the frequency and wave number matching conditions are satisfied

$$\omega_L = \omega_B + \omega_i, \quad \vec{k}_L = \vec{k}_B + \vec{k}_i,$$

where (ω_L, k_L) , (ω_B, k_B) and (ω_i, k_i) are the angular frequency and the wave vector of the impinging laser radiation, the scattered radiation and the ion plasma wave, respectively. In the typical conditions of interaction in a well underdense plasma and in the case of the backward SBS we have

$$\omega_L \gg \omega_i, \quad \vec{k}_L \parallel -\vec{k}_B,$$

therefore, according to the matching conditions one finds

$$k_i \approx 2k_L \approx 2 \frac{\omega_L}{c}, \quad k_B \approx -k_L \approx -\frac{\omega_L}{c}, \quad \omega_B = \omega_L - 2k_L c_s = \omega_L - 2\omega_L \frac{c_s}{c}.$$

In general, SBS can cause large rejection of the incident laser radiation leading to a strong reduction of plasma heating. In the case of homogeneous plasmas the threshold intensity of the SBS instability is set by the damping rates of the output waves. However, a more realistic case is the interaction of laser light with plasmas characterised by a longitudinal electron density scalelength L . In this case, the SBS instability threshold in terms of the electron density scalelength $L(\mu\text{m})$, the plasma electron temperature $T_e(\text{eV})$, and the laser light wavelength $\lambda_L(\mu\text{m})$, is [17]

$$(3.9) \quad I_{t, \text{SBS}} = 7 \times 10^{12} \frac{T_e}{L\lambda_L} \frac{n_e}{n_c} \text{ W/cm}^2.$$

Gradients in the expansion velocity of the plasma can also be effective in limiting the region of coupling [15]. The above equation can be modified in the presence of a velocity gradient by replacing L with $L_v \omega_p^2 / 2\omega_L^2$, where $L_v = v/(\partial v/\partial x)$ is the velocity scalelength.

3.2.2. Stimulated Raman scattering (SRS). We consider a plasma whose density is rippled by a density fluctuation δn_e associated with an electron plasma wave. Laser radiation propagating through this plasma generates a transverse current $\vec{J} \propto \vec{E}_L \delta n_e$. If the wave number and frequency matching conditions

$$\omega_L = \omega_R + \omega_e, \quad \vec{k}_L = \vec{k}_R + \vec{k}_e$$

are fulfilled, this transverse current produces a scattered radiation which, in turn, interferes with the incident laser radiation and reinforces the density fluctuations via the wave pressure $\vec{\nabla}(\vec{E}_L \cdot \vec{E}_R)/4\pi$. This positive feedback produces the Raman instability. One can easily verify that wave number and frequency matching conditions

can only be satisfied for densities $n_e < n_c/4$. By combining the frequency matching condition and the electron plasma wave dispersion relation $\omega_e^2 = \omega_p^2 + 3k_e^2 v_{th}^2 = \omega_p^2(1 + 3\lambda_D^2 k_e^2)$, one can obtain the frequency shift of the Raman scattered radiation:

$$\frac{\omega_R - \omega_L}{\omega_L} = - \left(\frac{n_e}{n_c} \right)^{1/2} [1 + 3\lambda_D^2 k_e^2]^{1/2}.$$

On the other hand, by using both matching conditions and dispersion relations for the two electromagnetic waves and for the plasma wave, one gets the wave vector of the plasma wave, in the condition of weak damping, $k_e \lambda_D \ll 1$:

$$\frac{k_e}{k_L} = 1 \pm \left(\frac{1 - 2N^{1/2}}{1 - N^{1/2}} \right)^{1/2},$$

where $N = n_e/n_c$ and + and - refer to the backward and forward SRS respectively. Again, in the case of inhomogeneous plasma and in the limit of $n_e \ll n_c/4$, the (back-scattering) threshold intensity is [17]

$$(3.10) \quad I_{t, \text{SRS}} = \frac{4 \times 10^7}{L \lambda_L} \text{ W/cm}^2 \quad (n_e \ll n_c/4).$$

We observe that, in contrast with the SBS threshold, the SRS threshold does not depend upon the electron temperature. This equation holds provided that the electron density is sufficiently small compared to the upper limit density at which the instability can occur, i.e. $n_c/4$. When this condition is not fulfilled a more accurate analysis is required [15] which predicts a reduction of the above threshold intensity by a factor of $(\lambda_L/2\pi L)^{1/3}$.

For sufficiently long scalelength, experiments show that a significant fraction ($\approx 10\%$) of the laser energy can be converted by SRS into hot electrons [18]. As discussed below in subsect. 3.2.6, these electrons, besides providing valuable information on the instability itself, give rise to intense emission of hard X-rays. Stimulated Raman scattering can therefore be exploited to enhance emission of hard X-rays in LPP X-ray sources.

3.2.3. Two-plasmon decay (TPD). Near the quarter critical density, $n_e = n_c/4$, laser light can *decay* into two electron plasma waves (plasmons). The plasma waves satisfy the energy and momentum conservation equations

$$\omega_L = \omega_B + \omega_R, \quad \vec{k}_L = \vec{k}_B + \vec{k}_R,$$

where ω_B and ω_R are the plasmon frequencies, while k_B and k_R are the corresponding wave vectors. In the limit of weak Landau damping of the electron waves, $k_{B,R}^2 \lambda_D^2 < 0.1$ and taking into account the dispersion relations for photons and plasmons, one gets the electron density at which the instability occurs:

$$\frac{n_e}{n_c} \approx \frac{1}{4} \left(1 - \frac{3}{2} (k_B^2 + k_R^2) \lambda_D^2 \right).$$

The minimum electron density for TPD is determined by the Landau damping condition $k_{B,R}^2 \lambda_D^2 \approx 0.1$, whereas the maximum density is given by the minimum value for $(k_B^2 + k_R^2)$, which is roughly k_L^2 . Consequently the density range for TPD to occur

and the corresponding frequencies of the two plasmons are:

$$0.19 < n_e/n_c < \frac{1}{4} \left(1 - \frac{3}{2} k_L^2 \lambda_D^2 \right), \quad \omega_{B, R} \approx \frac{\omega_L}{2} \left(1 \pm \frac{3}{4} (k_B^2 + k_R^2) \lambda_D^2 \right),$$

where the “+” sign refers to the blue-shifted plasmon, travelling with a wave vector component in the direction of the pump laser wave, while the “−” sign refers to the red plasmon, for which $\vec{k}_L \cdot \vec{k}_R$ can be either positive or negative [19].

Finally, the inhomogeneous threshold intensity is given by [17]

$$(3.11) \quad I_{t, TPD} = 5 \times 10^{12} \frac{T_e}{L_{1/4} \lambda_L} \text{ W/cm}^2,$$

where $L_{1/4}(\mu\text{m})$ is the electron density scalelength at $n_e \equiv n_c/4$. A signature of the occurrence of two-plasmon decay in laser-plasma interaction experiments is the production of electromagnetic radiation at a frequency corresponding to half-integer harmonics of the incident laser light, and in particular at the three-half harmonic. This emission originates from the non-linear coupling of the incident e.m. wave with the plasma waves produced by the two-plasmon decay instability. The spectral distribution of the three-half harmonic is strictly related to the dynamics of the coupling as well as the TPD instability itself. In particular, such a distribution can provide evidence [19] of propagation of the TPD plasmons in the density gradients, prior to their coupling with the incident laser light. As in the case of SRS, the occurrence of TPD leads to intense emission of hard X-rays, which can be easily diagnosed by using simple techniques based upon detection of X-rays with appropriately filtered X-ray detectors [20].

3.2.4. Filamentation. The occurrence of filamentation and/or self-focusing of a laser beam in a plasma causes substantial modifications of the plasma conditions, producing local density depression and an increase in the electron temperature. These circumstances, and the consequent effects on emission, absorption and scattering of radiation [21, 22] can provide indirect evidence of the process itself. An increase in the local electron temperature affects the emission properties of the plasma. In particular, the spectral distribution and intensity of the X-ray radiation emitted from the plasma region involved in the filamentation processes will result modified. All the emission processes (see subsect. 4.1) arising from bound-bound, free-bound and free-free transitions, will reflect the modifications occurring in the plasma, with a time response typically of the order of a picosecond [23, 24].

Filamentation of laser light in a plasma can occur when a small perturbation in the transverse intensity profile of the incident laser beam induces a perturbation in the electron density. This perturbation can be generated either directly, via the ponderomotive force, or indirectly as a consequence of localised collisional heating and subsequent plasma expansion. Once the perturbation has been generated, refraction of the laser light in the electron density perturbation enhances the intensity perturbation providing the feedback for the instability.

The most important theoretical results concerning the filamentation instability have been derived by using a simple model in which a sinusoidal intensity perturbation is imposed on a plane light wave interacting with a plasma. Recently, the effect of non-local heat transport has also been included [25] to account for deviations from the classical Spitzer-Härm conductivity occurring when the electron temperature scale-

length is shorter than the electron mean free path. In these conditions thermal transport must be described solving the electron Fokker-Planck equation. This modification to the electron heat conductivity leads to the following expression for the spatial growth rate of the filamentation instability:

$$(3.12) \quad K = \frac{k_{\perp}}{2\sqrt{\varepsilon}} \left[2 \frac{n_e}{n_c} \left(\gamma_p + \gamma_T \frac{\kappa_{SH}}{\kappa_{FP}} \frac{k_L^2}{k_{\perp}^2} \right) - \frac{k_{\perp}^2}{k_L^2} \right]^{1/2},$$

where $\varepsilon = 1 - n_e/n_c$ is the plasma dielectric function, κ_{SH} and κ_{FP} are the Spitzer-Härm conductivity and the effective Fokker-Planck conductivity that accounts for non-local transport effects [26] and k_{\perp} is the wave-number of the sinusoidal spatial modulation. The above equation basically consists of three terms. In the first term $\gamma_p = (1/4)(Z/(Z+1))(v_q^2/v_{th}^2)$ accounts for ponderomotive effects, v_q and v_{th} being the quiver and thermal velocity of the electrons respectively, and Z the charge state of the plasma. In the second term $\gamma_T = c^2 S/\omega^2 \kappa_{SH} k_B T_e$ accounts for thermal effects, S being the background inverse bremsstrahlung heating rate and T_e the electron temperature. The third term is due to diffraction and gives negative feedback as it tends to defocus the beam. The important consequence of non-local electron transport in the theory of filamentation instability is that the threshold of the instability is substantially reduced since, generally speaking, the growth rate is increased. In addition, an optimum perturbation wavelength is found which maximises the growth rate, in contrast with the theory based on the classical electron transport, which predicts a constant growth rate over a wide range of perturbation wavelengths ([27] and references therein).

Since filamentation is seeded by perturbations of the intensity profile of the laser beam, several beam smoothing techniques have been adopted in order to control the growth of the instability. Even though some of these techniques are very effective in reducing small scale filaments, whole-beam self-focusing is found to be basically unaffected [24]. A special role is played by filamentation when other laser-induced instabilities are present. In fact, filamentation (and self-focusing) can deeply modify both the longitudinal and transverse distribution of the laser field amplitude in the plasma. As a consequence, some instabilities may be enhanced, some other suppressed. As an interesting example, sum of frequencies via stimulated Brillouin scattering was observed in a filamentary plasma [28]. As we will see in the following, filamentation may also influence the X-ray generation process.

3.2.5. Surface plasma waves (SPW). A sharp plasma boundary, as that created by ultrashort pulses, can support surface waves [29]. These fluctuations of the electron density are accompanied by a mixed transverse and longitudinal electromagnetic field. In the case of a SPW propagating on a plasma surface ($z = 0$) in the x -direction, the electric field is given by

$$\vec{E}_i = (E_{x,i}, 0, \pm E_{z,i}) \exp[i(k_{x,i}x \pm k_{z,i}z - \omega t)], \quad i = 1, 2,$$

where “+” and “−” correspond to $z > 0$ ($i = 2$) and $z < 0$ ($i = 1$), respectively. In the physical conditions in which the SPW can be supported, k_x is represented by a complex number, while k_z , which is imaginary, causes the exponential decay of the field, for increasing values of $|z|$.

Due to the dispersion relations of SPWs and electromagnetic waves, p-polarised laser radiation, impinging on the plasma at an angle θ , cannot excite SPW at the

vacuum-plasma boundary. This can only occur if a low-density plasma is present in front of a high-density plasma boundary. Alternatively, SPW can also be excited in the presence of an electron density modulation at the plasma surface whose wave number (Δk_x) allows to fulfil the matching conditions

$$k_x = \frac{\omega_L}{c} \sin \theta \pm \Delta k_x = k_{\text{SPW}}.$$

The damping of the SPW, excited by intense laser radiation, produces a quite efficient absorption of laser energy in the plasma. In fact, the component of the electric field perpendicular to the plasma surface causes a strong coupling with the resonance absorption.

3.2.6. Hot electrons. Measurements of the spectrum of the X-ray radiation emitted in laser-plasma interaction experiments often show evidence of the generation of suprathermal electrons. In fact, besides the thermal Maxwellian population of electrons characterised by a temperature T_e , there is a small population ($n_h/n_c \approx 0.01$) which can be modelled as being distributed as a Maxwellian at a much higher temperature T_h . These electrons give rise, via bremsstrahlung emission, to hard X-ray radiation, well above the typical thermal emission from LPP. Besides its importance for the understanding of the mechanisms from which such hot electrons originate, such an emission can be useful in applications requiring harder X-rays.

Hot electrons may be produced by several mechanisms. For example, they may be generated as a consequence of the inhibition of electron thermal conduction [30-32] that prevents the laser energy absorbed in the proximity of the critical density layer to propagate towards the high-density plasma regions. In these circumstances, a thin plasma layer just beyond the critical surface can reach very high temperature, and the production of hot electrons and ions becomes possible. Taking into account the inhibited electron thermal conduction, one gets, for the hot electron temperature, $T_h \propto (I\lambda^2)^{2/3}$.

Another source of hot electrons is the resonance absorption mechanism. As shown above (subsect. 3.1.3), this absorption process produces an intense electric field parallel to the plasma density gradients, strongly localised in the proximity of the critical surface [15]. Numerical simulations [33] show that slow electrons that travel only a small fraction of this high-field region during a laser period, experience an oscillating electric field, which does not produce a significant increase of their kinetic energy. On the other hand, very fast electrons that move across the high-field region in a very small fraction of period, experience a constant electric field. However, due to the short duration of the electric field action, the energy gain of these electrons is very small. On the contrary, electrons with an intermediate velocity, crossing the region in a fraction of period, $\Delta t \leq T/2$, can gain as much energy as their initial kinetic energy. In this case the hot electron temperature scales as $T_h \propto (I\lambda^2)^{1/3}$ [34].

Finally, electrons can be accelerated up to *supra*-thermal energies by the electric field of the intense laser radiation or by that of the plasma waves. In the case of the transverse electromagnetic wave, the maximum electron energy gain is

$$(3.13) \quad \Delta \epsilon_{\text{max}} = \frac{1}{2} m v_q^2 \frac{1}{(1 - v_x/v_\phi)^2},$$

where v_q is the quiver velocity, v_x is the component of the electron velocity along the propagation direction of the wave, whose phase velocity is v_ϕ . Since the phase velocity of an electromagnetic wave propagating in a plasma is larger than the speed of the light in the vacuum $v_\phi = c(1 - \omega_p^2/\omega_L^2)^{-1/2} > c$, the electron remains under the action of an electric field of the same sign only for a short time. Therefore, the simple interaction between electrons and an electromagnetic plane wave does not produce fast electrons, except for very high laser intensities. In the case of interest, *i.e.* for electrons with a low initial speed $v_x/v_\phi \ll 1$, for $\lambda = 1 \mu\text{m}$ and $I = 10^{15} \text{ W/cm}^2$, we find, $\Delta\varepsilon_{\max} \approx 200 \text{ eV}$. In contrast, for a relativistic intensity $I = 10^{19} \text{ W/cm}^2$, then $\Delta\varepsilon_{\max} \approx 0.6 \text{ MeV}$.

Longitudinal electron plasma waves are responsible for the generation, via collisionless damping processes, of suprathermal electrons with energies up to the MeV region [18]. The phase velocity is given by $v_\phi = v_{\text{th}}(3 + 1/(k\lambda_D)^2)^{1/2}$ and can be relatively low so that some electrons can spend a long time in a region of constant sign electric field and gain much energy from the wave. In the optimum condition the electron energy gain is

$$\Delta\varepsilon_{\max} = 4mv_\phi^2 \left(\frac{v_q}{v_\phi} \right)^{1/2},$$

where v_q is the electron quiver velocity, due to the electric field of the plasma wave. The amplitude of the electric field of the plasma wave can be obtained by the Poisson equation and is $E = 4\pi k^{-1} \delta n_e e$. If we introduce the ratio between the phase and the thermal velocity $\eta = v_\phi/v_{\text{th}}$, and approximate the ratio of the quiver velocity to the phase velocity as follows:

$$\frac{v_q}{v_\phi} = \frac{eEk}{mw^2} = \frac{\delta n_e}{n_e} \left(\frac{\omega_p}{\omega} \right)^2 \approx \frac{\delta n_e}{n_e},$$

we can rewrite the previous formula for the energy gain:

$$(3.14) \quad \Delta\varepsilon_{\max} = \frac{1}{2} mv_{\text{th}}^2 8\eta^2 \left(\frac{\delta n_e}{n_e} \right)^{1/2}.$$

For typical values of interaction experiments with long scalelength plasmas, *i.e.* for $\eta = 10$, $\delta n_e/n_e = 0.1$ and $T_e = 0.5 \text{ keV}$, we find $\Delta\varepsilon_{\max} = 125 \text{ keV}$. We observe that such high energies can be achieved at laser intensities much lower than the value considered above.

In the early experiments on laser-driven inertial fusion it was soon recognised that these hot electrons were highly detrimental to the achievement of ICF conditions [5]. In fact it was found that they produced a substantial pre-heating of the fusion pellet which prevented its efficient inertial compression. Therefore, a strong effort was spent in trying to design interaction configurations in which hot electron production could be inhibited. One of the results of this effort was the development of short wavelength high power laser technology. In fact, the use of shorter wavelengths leads to a substantial reduction of laser-induced instabilities and therefore to a less efficient generation of plasma waves and hot electrons. Another approach to a strong reduction of laser induced instabilities and hot electrons was the indirect drive approach in which pellet implosion is driven by X-rays instead of laser light directly.

It is interesting to note that recently, with the advent of ultra-short pulse laser

technology, a novel scheme has been proposed [35] as a short-cut towards the achievement of ignition in conditions that, in either direct and indirect drive schemes are otherwise prohibitive. Surprisingly, this scheme is indeed based upon a massive production of hot electrons by an ultra-short, powerful laser pulse. The resulting hot electron beam penetrates into the highly overdense region down to pellet core at the time of maximum compression. Here it releases most of its energy giving rise to a localised nuclear burn in the pellet core thus initiating the nuclear fusion process. The possibility of achieving this goal is entirely related to the understanding of hot electron production mechanisms and their control.

3.3. Femtosecond interactions. – The advent of chirped pulse amplification [36] has led to high power lasers capable of delivering several joules in tens of femtoseconds ($1 \text{ fs} = 10^{-15} \text{ s}$) [37, 38]. These lasers allow to study radiation-matter interaction at intensities exceeding 10^{20} W/cm^2 . At these intensities the electric field of the laser radiation exceeds by several orders of magnitude the atomic electric field. Matter is ionised in a fraction of the wave period, *i.e.* almost instantaneously. The basic interaction physics in this novel regime [39] is entirely new, and possible scenarios are described below.

3.3.1. Basic features of femtosecond interactions. As discussed in sect. 2, the characteristic time of hydrodynamic expansion of laser-produced plasmas, *i.e.* the time taken by the plasma to expand by a length comparable with the laser wavelength, is of the order of a few picoseconds. Therefore, the use of femtosecond laser pulses enables to study the interaction of intense optical radiation with plasmas characterised by solid density ($5 \times 10^{23} \text{ el/cm}^3$) and ultra-steep gradients. In fact, the scale length of the plasma density in the direction perpendicular to the target surface is roughly given by $L = c_s \Delta t$, where c_s is the sound speed given by eq. (2.3) and Δt is the laser pulse duration. For $\Delta t \approx 100 \text{ fs}$ and even for a relatively high expansion velocity $c_s = 10^7 \text{ cm/s}$, $L \approx 100 \text{ \AA}$, which is much shorter than the vacuum wavelength λ of the impinging laser radiation, that is $\lambda \gg L$. Moreover the ponderomotive force acting at the plasma-vacuum interface strongly contributes to the steepening of the density profile. In these interaction conditions, according to eqs. (3.9)-(3.11), parametric instabilities (Raman, Brillouin, etc.) and in general the coupling between plasma modes and laser field cannot develop due to the extremely short scalelength of the underdense region and the short duration of the laser pulse. In these experimental conditions laser radiation impinges at a given angle θ on a plasma surface characterised by a sharp density profile.

According to current ionisation models (see, for example, [40] and [41]) at the high intensities attainable by femtosecond lasers, the time required to ionise the target is extremely short, so that the plasma becomes opaque to the impinging radiation in a fraction of a period of the laser field oscillation. In the typical experiments reported so far, the laser pulse is focused on a thick target, or a film coated on a transparent massive substrate. In principle, the plasma produced in these conditions can be divided into three regions. The first region consists of the plasma expanding in the vacuum, whose typical extent is a few hundreds of angstroms. The second, characterised by an electron density of the order of that of the solid target times the average ionisation degree, extends over a length of the order of the skin depth, typically $\delta_S = c/\omega_P$, that is, of the order of a few hundreds of \AA . In these first two regions, laser energy deposition is accounted for by different mechanisms including collisional absorption,

resonance absorption, Brunel effect and anomalous skin effect. A strong electron heating is produced in a very short time, so that the electron velocity distribution is far from a Maxwellian and the plasma, despite the high density, is away from thermal equilibrium. The high density and the high electron kinetic energy make these plasmas bright sources of X-rays pulses, with photon energy extending up to the MeV region. The third region, not directly reached by the laser e.m. field, is heated by thermal diffusion and extends over several thousands of angstroms.

In reality, such a schematic view of the interaction can be strongly modified if target pre-heating occurs, due to the presence of spurious laser pre-pulses which give rise to a precursor plasma on the target surface. In fact, in the case of laser systems based on chirped pulse amplification technique, laser pre-pulse can arise from leakage through the compression stage of the laser [42] or from amplified spontaneous emission [43]. This pre-pulse can produce a tenuous plasma in front of the target, before the arrival of the main pulse, thus deeply changing the interaction conditions.

In order to minimise pre-pulse effects, targets consisting of very thin ($d < 1000 \text{ \AA}$) plastic (FORMVAR) foils have been used [44]. Such thin foils have unique properties that make their use as targets in fs laser interaction experiments particularly interesting. Primarily, due to the high optical transparency of these targets, the threshold intensity for damage, and consequent plasma formation, is high compared to the typical pre-pulse intensity level of good performance femtosecond lasers. Moreover, in the laser pulse regime considered here a higher-temperature plasma can be achieved during the interaction, as a consequence of minor energy losses due to heat conduction. In fact, the thermal conduction length is much larger than the target thickness.

An important peculiarity of the interaction of high-intensity femtosecond laser pulses with plasmas is represented by the occurrence of relativistic effects. In fact, the electron motion in the oscillating field of the laser wave is characterised by velocities that approach the speed of light in a vacuum. From the relativistic equation of motion one gets the electron velocity (normalised to the speed of light) and the related Lorentz factor

$$(3.15) \quad \beta = \frac{eE}{\gamma m\omega c}, \quad \gamma = (1 - \beta^2)^{-1/2}.$$

It is useful to introduce the dimensionless relativistic parameter

$$(3.16) \quad a_0 = \frac{eE}{m\omega c} = 8.5 \times 10^{-10} \lambda_L (\mu\text{m}) [I (\text{W/cm}^2)]^{1/2}$$

which leads to the following expression for the Lorentz factor, averaged over an oscillation period of the laser wave:

$$(3.17) \quad \gamma = \left(1 + \frac{\alpha a_0^2}{2} \right)^{1/2},$$

where $\alpha = 1$ for linearly polarised radiation and $\alpha = 2$ for circular polarised radiation. According to these equations, one can see that relativistic effects become relevant for $a_0 \approx 1$ that, for $\lambda_L = 1 \mu\text{m}$ gives a laser intensity of the order of 10^{18} W/cm^2 .

3.3.2. Propagation of laser light in overdense plasmas. In principle, femtosecond laser systems open the possibility of investigating phenomena produced by high-intensity radiation in experimentally unexplored conditions, including propagation in plasmas whose density is higher than the critical density. Recently, penetration of ultraintense, short laser pulses into overdense plasmas has been extensively investigated both theoretically and experimentally also in view of its relevance (see also subsect. 3.2.6) to the implementation of the fast ignitor concept [35]. Several effects that predict enhanced propagation in overdense plasmas have been considered including anomalous skin effect [45], self-induced transparency (see, for example, [46]) and ponderomotive force driven hole boring [47-49].

At non-relativistic intensity the propagation of an e.m. wave in an overdense plasma is expected to be limited to the plasma skin depth δ_S . A deeper penetration (anomalous skin effect) is possible in very hot plasmas, where the electron velocity becomes larger than $\omega_L \delta_S$ [50]. Recently the anomalous skin effect in solid-density plasmas has been considered both analytically [51] and numerically [52], with attention to the case of the interaction with thin foils.

In a recent experiment [53] the propagation of intense 30 fs laser pulses through thin plastic targets has been studied. The measured transmittivity for laser intensities greater than 10^{17} W/cm^2 was found to be orders of magnitude higher than the transmittivity predicted by current models. In particular, when the intensity was $3 \times 10^{18} \text{ W/cm}^2$, *i.e.* only weakly relativistic, almost complete transparency of solid density laminar plasmas without substantial modification of the spectrum was observed with the additional evidence of spatial filtering effects in the transmitted pulse. Incidentally, this latter effect provides a novel and simple way to perform a difficult task like the spatial filtering of high intensity, ultrashort, aberrated laser pulses. The observation of transparency of solid density plasmas to ultra-short pulses at intensities corresponding to relatively low values of the relativistic parameter introduced above ($a_0 \approx 1.2$) opens a completely new area of investigation, very promising for applications like the fast ignitor scheme, and challenging for theoretical plasma physics.

The same group [54] recently proposed an explanation of these new observed phenomena based on the effect of a super-intense magnetic field self-induced during the ultrafast volume ionisation of the target. The magnetic field, parallel to the laser oscillating magnetic field and therefore orthogonal to the wave vector, reduces the electron transverse quivering motion and consequently the laser pulse can propagate through a highly overdense plasma without significant attenuation and spectral modifications. The authors also show that in the cyclotron resonance condition electrons can be accelerated to energies of several MeVs.

4. – X-ray emission from laser plasmas

4.1. Fundamental emission processes. – Once the plasma has gained thermal energy, radiation is emitted via free-free, free-bound and bound-bound mechanisms. In the first mechanism, free electrons interacting with the Coulomb potential of the ions, radiate in a continuum electromagnetic spectrum, giving rise to the so-called *bremssstrahlung* emission. The second process, known as *recombination*, consists in the transition from initial free electron states to bound electron states and produces a continuum electromagnetic spectrum. The third emission mechanism produces a line

spectrum as a result of transitions between discrete (bound) levels of ionised atoms [55].

4.1.1. Bremsstrahlung. The power radiated by this process can be evaluated using a simple argument. Let us consider an electron, with an initial velocity v , interacting with an ion, with an impact parameter b . The characteristic interaction time is $\tau = 2b/v$. So, the dominant frequency in the radiated electromagnetic spectrum is $\nu \approx 1/2\pi\tau = v/4\pi b$. On the other hand, the energy ΔE , radiated during a single electron-ion impact can be evaluated on the basis of the maximum acceleration $a = Ze^2/b^2m$, suffered by the electron. Therefore we have

$$\Delta E = \frac{2e^2 a^2 \tau}{3c^3} \approx \frac{4}{3} \frac{Z^2 e^6}{m^2 c^3 b^3 v} .$$

The number of electron-ion collisions per unit time, with an impact parameter ranging from b to $b + db$, is $2\pi n_i v b db$. So, the power radiated per electron is

$$w = \int \Delta E \cdot 2\pi n_i v b \cdot db \approx \frac{4}{3} \frac{Z^2 e^6}{m^2 c^3} 2\pi n_i \int_{b_{\min}}^{b_{\max}} \frac{db}{b^2} ,$$

where the maximum impact parameter b_{\max} is given by the Debye length λ_D , while the minimum impact parameter, determined by the uncertainty principle, is the De Broglie wavelength, i.e. $b_{\min} = h/2\pi mv$. Since $b_{\min} \ll b_{\max}$, the integration gives

$$w \approx \frac{16\pi^2}{3} \frac{e^6}{mhc^3} Z^2 n_i v .$$

Considering a Maxwellian distribution of electron velocities:

$$(4.1) \quad f_e = n_e \left(\frac{m}{2\pi k_B T_e} \right)^{3/2} \exp \left[-\frac{mv^2}{2k_B T_e} \right] ,$$

we can obtain the bremsstrahlung power radiated per unit volume W_B by evaluating the integral

$$W_B = \int_0^\infty w f_e 4\pi v^2 dv .$$

Due to the approximations made above, this calculation slightly overestimates W_B . The exact numerical solution differs from the result given above by a factor of $1/3^{1/2}$ and gives

$$(4.2) \quad W_B = \frac{32\pi^2}{3^{3/2}} \frac{Z^2 e^6}{mc^2} \frac{n_e n_i}{h} \left(\frac{2k_B T_e}{\pi m} \right)^{1/2} = 1.6 \times 10^{-27} Z n_e^2 [T_e(k)]^{1/2} \text{ erg s}^{-1} \text{ cm}^{-3} .$$

The characteristic dependence of bremsstrahlung emission upon electron density and temperature is clearly shown by this expression. To evaluate the spectral distribution of bremsstrahlung emission, we start from the relation between the frequency and the impact parameter and then we integrate the above expression over

the frequency ν instead of b assuming $\nu_{\max} \gg \nu_{\min}$, where $\nu_{\min} \approx 0$:

$$w = \int 2\pi n_i \Delta E v b db \approx$$

$$\approx \frac{4}{3} \frac{Z^2 e^6}{m^2 c^3} 2\pi n_i \int_{b_{\min}}^{b_{\max}} \frac{db}{b^2} \approx - \frac{4}{3} \frac{Z^2 e^6}{m^2 c^3} \frac{8\pi^2 n_i}{v} \int_{\nu_{\min}}^{\nu_{\max}} d\nu = A \int_{\nu_{\min}}^{\nu_{\max}} d\nu \approx A \nu_{\max},$$

where $\nu_{\max} = mv^2/2h$, $\nu_{\min} = v/4\pi\lambda_D$. According to this result, the energy radiated by an electron of velocity v per unit frequency, in the frequency range $0 < \nu < \nu_{\max}$, is a constant and is equal to zero for $\nu > \nu_{\max}$. Therefore, the contribution to the frequency ν comes only from those electrons whose velocity is $v > (2hv/m)^{1/2}$. Performing the integration, taking into account the contribution of all the electrons of the Maxwellian distribution and correcting by the factor $1/3^{1/2}$, we finally obtain the spectral intensity

$$W_B^\nu = \frac{1}{3^{1/2}} \int_{(2hv/m)}^{\infty} Af_e 4\pi v^2 dv = \frac{32\pi}{3} \left(\frac{2\pi}{3k_B T_e m} \right)^{1/2} \frac{Ze^6 n_e^2}{mc^3} \exp \left[- \frac{h\nu}{k_B T_e} \right]$$

that, in a numerical form, becomes

$$(4.3) \quad W_B^\nu \approx 6.8 \cdot 10^{-38} Z n_e^2 [T_e(k)]^{-1/2} \exp \left[- \frac{h\nu}{k_B T_e} \right] \text{erg s}^{-1} \text{cm}^{-3} \text{Hz}^{-1}.$$

Taking into account the relation between the spectral intensity per unit of frequency and that per unit of wavelength, we also obtain the useful expression

$$(4.4) \quad W_B^\lambda = W_B^\nu \frac{c}{\lambda^2} \approx 2 \cdot 10^{-27} Z n_e^2 [T_e(k)]^{-1/2} \lambda^{-2} \exp \left[- \frac{hc}{\lambda k_B T_e} \right] \text{erg s}^{-1} \text{cm}^{-4}.$$

The maximum of the spectral emission occurs for $hc/\lambda k_B T_e \approx 2$, i.e. at a wavelength $\lambda_{\max}(\text{\AA}) = 6200/T_e(\text{eV})$. This bell-shaped distribution is similar to that of a blackbody

$$(4.5) \quad u_\lambda = \frac{8\pi hc}{\lambda^5} \left[\exp \left[- \frac{hc}{\lambda k_B T} \right] - 1 \right]^{-1} \text{erg cm}^{-4},$$

whose spectral energy density for the same temperature however, is peaked at a shorter wavelength. In fact, in the case of blackbody radiation, the above condition for maximum emission becomes $hc/\lambda k_B T_e \approx 5$, and the wavelength is therefore $\lambda_{\max}(\text{\AA}) = 2500/T_e(\text{eV})$. Moreover the total black-body emission scales as T^4 (Stefan's law), while that of the bremsstrahlung scales as $T^{1/2}$.

4.1.2. Recombination. When a free electron is captured by a $(Z+1)$ -fold ionised atom, leading to a transition to a bound state of a Z -fold ionised atom, a photon is emitted with an energy

$$h\nu = \frac{1}{2} mv_{\text{th}}^2 + E_Z^n,$$

where the first and the second terms in the right-hand side of the equation represent the initial kinetic energy of the electron and the energy of the final atomic state, Z is the ion charge and n the principal quantum number. Since the initial electron energies can take values over a continuum, the radiation is emitted in a continuum frequency spectrum. However, the contribution of each transition to the continuum satisfies the condition $h\nu \geq E_Z^n$ (recombination edge), so that the continuum recombination spectrum is characterised by “jumps”, corresponding to different recombination stages. The spectral intensity of the recombination continuum can be expressed in terms of that of the bremsstrahlung one as follows:

$$(4.6) \quad W_r^v = W_B^v \cdot 2.2 \cdot 10^{-32} \frac{Z^3 n_e^2}{T_e^{3/2}} \sum_{n=1}^{\infty} \frac{1}{n^3} \exp \left[-\frac{Z^2 E_H}{n^2 k_B T_e} \right] \text{erg s}^{-1} \text{cm}^{-3} \text{Hz}^{-1},$$

where $E_H = 13.6$ eV is the hydrogen ionisation energy. Note that, according to the above discussion, the argument of the exponential is always negative. Similarly for the ratio of the spectrally integrated recombination and bremsstrahlung intensities we find

$$(4.7) \quad \frac{W_r}{W_B} = \frac{\int_0^{\infty} W_r^v d\nu}{\int_0^{\infty} W_B^v d\nu} = \frac{2Z^2 E_H}{k_B T_e} \sum_{n=1}^{\infty} \frac{1}{n^3} \approx 2.4 \frac{Z^2 E_H}{k_B T_e}.$$

According to this result, for low- Z and/or high-temperature plasmas bremsstrahlung emission overcomes recombination emission.

4.1.3. Lines. Transitions of bound electrons from excited to lower states of the ions in a plasma can give important contribution to the emission of radiation. In particular, strong contribution comes from transitions to the ground state (resonance lines). On the other hand, transitions between excited states, even though typically weaker, are very useful for plasma diagnostic purposes because they escape from the plasma without substantial re-absorption.

The emission coefficient, that is, the specific power radiated per unit volume, solid angle and frequency interval, corresponding to the transition from the upper state u to the lower state l is

$$(4.8) \quad \epsilon_v = \left(\frac{h\nu}{4\pi} \right) A_{u,l} n_u L(\nu - \nu_{u,l}) \text{erg cm}^{-3} \text{s}^{-1} \text{Hz}^{-1} \text{sr}^{-1},$$

where n_u is the number density of ions in the upper state, $L(\nu - \nu_{u,l})$ is the line shape function, $\nu_{u,l}$ is the central frequency of the transition between the two states of energy E_u and E_l and

$$(4.9) \quad A_{u,l} = \frac{8\pi h\nu^3}{c^3} B_{u,l} = \frac{64\pi^4}{c^3 h} \nu^3 P_{u,l}^2 \text{s}^{-1}$$

is the spontaneous emission coefficient. $A_{u,l}$ and $B_{u,l}$ represent the probability per unit time of spontaneous and induced emission, respectively. $P_{u,l}^2$ is the modulus squared of the matrix element of the electric dipole moment evaluated between the two states. The

line shape function $L(\nu - \nu_{u,1})$, describing the emitted spectrum close to the central frequency $\nu_{u,1}$, is a normalised function

$$\int_0^\infty L(\nu - \nu_{u,1}) d\nu = 1 .$$

The energies of the levels and the $A_{u,l}$ -values are intrinsic properties of the radiating ions or atoms and tabulated values [56] have been obtained by quantum mechanics calculations and confirmed by indirect measurements. In contrast, level populations and line shapes depend upon the physical conditions of the plasma in which the radiating atoms or ions are embedded. In particular, populations are determined by the dynamical balance of several collisional and radiative processes inside the plasma.

Three main physical processes determine the line shape: a) the finite radiative lifetime of the bound states involved in the transition (natural broadening); b) the thermal motion of radiating atomic systems (Doppler broadening); c) the interaction of radiating systems with the rest of the plasma (pressure broadening). Natural line broadening is determined by the sum of transition probabilities for all spontaneous transitions originating from both upper and lower levels involved in the transition. In this case the line shape is a Lorentzian

$$(4.10) \quad L(\nu - \nu_{u,1}) = \frac{L_0}{1 + [(2(\nu - \nu_{u,1}))/\Delta\nu_N]^2} ,$$

where the characteristic width is determined by the mean lives of the two levels τ_l and τ_u according to the following expression:

$$(4.11) \quad \Delta\nu_N = \frac{1}{2\pi\tau_l} + \frac{1}{2\pi\tau_u} .$$

In the non-relativistic limit, the Doppler shift is simply given by

$$\Delta\nu = \frac{v_x \nu}{c} ,$$

where v_x is the component of the velocity along the line of sight. For a Maxwellian distribution of electron velocities the line shape is a Gaussian:

$$(4.12) \quad L(\nu - \nu_{u,1}) = L_0 \exp \left[- \left(\frac{2 \sqrt{\ln 2} (\nu - \nu_{u,1})}{\Delta\nu_D} \right)^2 \right] ,$$

where the FWHM depends upon the electron temperature T_e and the atomic mass number A

$$(4.13) \quad \Delta\nu_D = \frac{2\nu_{u,1}}{c} \sqrt{\frac{2 \ln 2 k_B T_e}{M}} \cong 6.65 \times 10^{-9} \sqrt{\frac{T_e(\text{eV})}{A}} ,$$

Pressure broadening is due to the interaction of the radiating systems with the other particles of the plasma. For an interaction with a cross-section σ , the line shape is

essentially a Lorentzian and the FWHM is given by

$$(4.14) \quad \Delta\nu_p \approx \frac{1}{2\pi\tau_p} \approx \frac{\sigma v_{\text{rel}} n_p}{2\pi},$$

where n_p is the number density of the perturbers and v_{rel} is the relative velocity of the interacting atomic systems. The so-called Stark broadening is the most important pressure broadening mechanisms in a plasma. It is due to the interaction of the radiating system with the microscopic electric fields produced by the surrounding particles.

In plasmas the natural line width is usually negligible compared with the widths due to Doppler and Stark effects. In particular, Stark broadening becomes dominant at high plasma densities and for highly ionised species like hydrogen-like ions. As discussed below, in the case of plasmas produced by high-contrast, high-intensity short laser pulses, Stark broadening becomes an important diagnostic for density measurements [57]. On the other hand, low-density plasmas can also be investigated by means of pressure broadening if high- n state lines are used [58, 59].

4.2. Radiation transport in plasmas.

4.2.1. Basic definitions. As a general rule, a medium can absorb the radiation that it generates. In conditions of thermal equilibrium this principle is expressed by the Kirchhoff's law that connects the emitting power of a body, *i.e.* the power radiated per unit surface, solid angle and frequency, to its spectral absorptivity, namely the ratio of the absorbed monochromatic power to the power impinging on the surface, via the emitting power of the blackbody, that is an universal function of temperature and frequency:

$$e(\nu, T) = \alpha(\nu, T) \cdot e^{\text{BB}}(\nu, T).$$

The hemispherical emitting power of a blackbody is related to its energy density $u^{\text{BB}}(\nu, T)$, by the simple relation:

$$e^{\text{BE}}(\nu, T) = \frac{c}{4} u^{\text{BB}}(\nu, T) = \frac{c}{4} \frac{8\pi h\nu^3}{c^3} \left[\exp\left(\frac{h\nu}{k_B T}\right) - 1 \right]^{-1}.$$

The intensity of the radiation emitted by a plasma element of thickness dx per unit solid angle is

$$dI = \xi \cdot dx - Ik \cdot dx,$$

where ξ is the emission coefficient (due to free-free, free-bound and bound-bound emission) and k is the effective absorption coefficient. The equation states that while radiation propagates in the plasma over a distance dx , its intensity increases by ξdx due to emission processes and decreases by $Ik dx$ due to reabsorption processes. The previous equation can be rewritten in the following form:

$$(4.15) \quad \frac{dI}{dt} = \frac{\xi}{k} - I = S - I,$$

where $d\tau = k dx$ and S is the source function. In the case of thermodynamic equilibrium

the source function is related to the Planck function according to the following relation:

$$S = \frac{\xi}{k} = \frac{c}{4\pi} u^{\text{BB}}(\nu, T).$$

The dimensionless quantity τ is the optical depth defined as

$$\tau = \int_0^x k \cdot dx,$$

which takes into account the opacity effects suffered by the radiation propagating in the plasma.

The integration of the radiative transport equation is not straightforward, because ε and k depend on time and space co-ordinates in the plasma. The solution can be easily found in the simple and instructive case of a stationary and uniform plasma. In fact, by integrating the equation, we obtain

$$I(\tau) = I(0) \exp[-\tau] + \frac{\xi}{k} [1 - \exp[-\tau]],$$

where $I(0)$ is the source term at $x = 0$, which is zero if we consider the case of pure plasma self-emission.

4.2.2. Limit approximations: thin and thick plasmas. Two important cases are the limits of negligible and very large optical depths. The first case, *i.e.* $\tau \ll 1$, corresponds to the so-called condition of optically thin plasma. In this case the intensity is simply given by

$$(4.16) \quad I(\tau) \cong \xi x.$$

In other words, the intensity of the radiation emitted by the plasma is proportional to the plasma thickness and to the emission coefficient related to the different emission mechanisms (ff, fb, bb) activate inside the plasma.

The second case, *i.e.* $\tau \gg 1$, corresponds to the condition of an optically thick plasma. In this case the radiated intensity does not depend upon the plasma thickness and the strong self-absorption deeply modifies the original spectrum of the energy radiated by the plasma interior. In the condition of thermal equilibrium, the spectral distribution of the radiated intensity approaches that of blackbody:

$$(4.17) \quad I(x) \cong \frac{\xi}{k} = \frac{c}{4\pi} u^{\text{BB}}(\nu, T).$$

From the previous considerations it follows that self-absorption in a plasma becomes important when τ approaches or is greater than unity. We note, however, that a plasma can be optically thick in some spectral regions while being thin in another regions. For the same reason self-absorption is more important for frequencies close to the maximum than for the frequencies in the tail of the line.

4.3. Equilibria in laser-produced plasmas. – In the typical conditions relevant to laser produced plasmas, the peak of the spectral self-emissivity of the plasma falls in

the X-ray region. Much information on the physical properties of the plasma emitting region can be gained from a spectroscopic analysis of this emission. However, due to the complexity of the physical system under investigation, the analysis of experimental results is usually performed via comparison with numerical simulations.

A simplified steady-state model of the plasma is often considered in the simulations and the spectral features of the radiation emitted are studied as a function of a set of input plasma parameters including atomic number, ion and electron temperature, electron density and plasma size. These parameters can be set according to the experimental results or following the results of hydrodynamic simulations (see sect. 2) and will, in turn, provide further information on the plasma.

The first issue to be addressed in the study of emission of radiation from a plasma is the kind of equilibrium to be considered. The degree of interaction among the three plasma subsystems, namely electrons, ions and radiation, must be specified in order to determine the population of all available energy levels. Consequently, one can determine the spectral distribution of radiation energy emitted via bound-bound, free-bound and free-free transitions. Once the particular equilibrium is specified, the result of the numerical analysis of atomic physics processes can be compared with the experimental results provided that radiation transport effects and, possibly, time-dependent effects are taken into account. In the following, a summary of the main results on plasma equilibria will be given with emphasis on the conditions to be fulfilled, in terms of density and temperature, for the various types of equilibria to hold. Some criteria which allow the validity of a steady-state approximation to be tested will be also given below.

4.3.1. Thermal equilibrium (TE). Although this kind of equilibrium does not apply to laboratory plasmas and is only approached in stellar interiors, it can be considered as a reference condition in the limit of high plasma density. A plasma is said to be in TE when electrons, ions and radiation are strongly coupled to each other and share the same temperature. The populations N_u and N_l of two ionic bound levels, u and l, with statistical weights g_u and g_l , respectively, are given by the Boltzmann equation

$$(4.18) \quad \frac{N_u}{N_l} = \frac{g_u}{g_l} \exp\left[-\frac{\Delta E_{u,l}}{k_B T}\right],$$

where $\Delta E_{u,l}$ is the energy difference between the two levels and T is the thermodynamic temperature of the plasma. The population of ionisation states is given by the Saha equation

$$(4.19) \quad \frac{N(Z+1) n_e}{N(Z)} = \frac{g_0(Z+1)}{g_1(Z)} \left[\frac{2\pi m k_B T}{h^2} \right]^{3/2} \exp\left[-\frac{\chi_0(Z)}{k_B T}\right],$$

which gives the ratio between the population densities of two contiguous ionisation states with charges Z and $Z+1$, and statistical weights $g_0(Z)$ and $g_0(Z+1)$, respectively. The subscript "0" refers to the ground state of the ion and, in TE, it is, by far, the most populated one; $\chi_0(Z)$ is the ionisation potential of the ion with charge Z , n_e is the electron density, m is the electron mass and h is the Planck constant. Free electrons are distributed among the available energy levels and their velocities follow the Maxwell distribution function f_e given by eq. (4.1). The number of electrons with

velocities between v and $v + dv$ is therefore given by the relation $dN_{v, v+dv} = 4\pi f_e v^2 dv$. Finally the spectral energy density of the radiation emitted by a plasma in TE is that of a black body and is given by Planck's formula given by eq. (4.5). This formula, along with the equations given above completely define the spectral properties of a plasma in thermal equilibrium. When TE is not satisfied, a new set of equations will have to be derived.

4.3.2. Local thermal equilibrium (LTE). The most important case of deviation from TE in a plasma consists in a relatively weak coupling of radiation with atoms and ions. If we assume that the populations of the available energy levels are entirely determined by particle collisions, radiation processes being ineffective, then we obtain another type of equilibrium called local thermal equilibrium (LTE). Also this equilibrium, in general, is still too restrictive for laser-produced plasmas to hold but, in some cases, can provide a simple estimate of the spectral emissivity, particularly in short-pulse laser-produced plasmas where electron densities can be very high.

In an optically thin LTE condition, radiation can escape from the plasma and particle collisions by themselves account for the population of the ion energy levels. The main difference between LTE and TE is that radiation and particles do not share the same temperature. However, the equations given in subsect. 4.3.1 are still valid, provided that the thermodynamic temperature, T is replaced with the electron temperature, T_e .

In contrast, the spectral properties of the radiation emitted by a plasma in LTE are now determined by bound-bound transitions which give rise to line radiation, and by free-bound and free-free transitions both yielding continuum radiation as discussed in subsect. 4.1.

As can be derived from the initial assumptions, LTE will be satisfied as long as collisional processes are dominant over radiative ones, that is, the probability that an excited ion decays due to spontaneous emission must be much smaller than the probability of collisional decay. According to this condition, an operational criterion has been derived [60] based on the following inequality between collisional de-excitation and spontaneous emission:

$$(4.20) \quad n_e n_u X(T_e, u, l) \geq 10 n_u A_{u,1},$$

where $X(T_e, u, l) = \langle \sigma_{u,1} v_e \rangle$ is the electron de-excitation coefficient for a transition from an upper level, u , to a lower level, l , that depends upon the cross-section $\sigma_{u,1}$ and is averaged over all possible electron velocities, v_e . Using a Maxwellian distribution, one finds the condition on the electron density for an optically thin plasma in order for LTE to hold

$$(4.21) \quad n_e \geq 1.7 \times 10^{14} T_e^{1/2} \Delta E_{u,1}^3 \text{ cm}^{-3},$$

where the transition energy, $\Delta E_{u,1}$ and the electron temperature, T_e are expressed in eV. According to this condition, in a plasma with given electron density and temperature, there is a maximum energy gap below which LTE holds for a given transition. For example, in a plasma with an electron density of 10^{21} cm^{-3} and an electron temperature of 500 eV, the maximum b-b transition energy for which LTE is satisfied is approximately 65 eV. In contrast, a b-b transition of 2 keV, typical of K -shell emission from H-like Al ions, can be considered in LTE if $n_e > 3 \times 10^{25} \text{ cm}^{-3}$, i.e. at densities well above the Al solid density.

If the plasma is optically thick, *i.e.* if radiation is coupled to ions and electrons, this criterion may be relaxed to lower densities. In fact, opacity effects give rise to radiative excitation which tends to balance radiative decay, making collisional processes effectively responsible for de-excitation. However, the condition given above should still be regarded as a necessary, but not sufficient condition for a plasma to be in LTE.

4.3.3. Non-LTE plasmas. In a plasma where the condition given above for LTE is not fulfilled, radiative processes are expected to play an important role in determining the population of the available energy states. In the general case all the possible electron processes will have to be taken into account and the populations of the levels will now depend upon atomic cross-sections. However, as these processes depend differently upon the electron density, one can expect that, in particular conditions, some of them will be more efficient than others, leading to a substantial simplification of the problem. If we assume that the plasma is optically thin, ion excitation and ionisation will be supported by collisional processes. A question arises on how these processes are balanced, *i.e.* which of the possible de-excitation and recombination processes will have to be considered. In general, when the density is not high enough to ensure LTE, all inverse processes will contribute to de-excitation and recombination. On the other hand, if the density is sufficiently low, all collisional processes will become inefficient and only radiative de-excitation and recombination processes will have to be considered. In this last case the problem can be simplified leading to the so-called coronal model.

4.3.4. Coronal equilibrium (CE). In this case collisional excitation and ionisation are balanced respectively by radiative de-excitation and recombination. By comparing the ionisation and recombination rates one obtains the basic equation which governs ionisation processes in the coronal equilibrium

$$(4.22) \quad n_e N(Z) S(T_e, Z, 0) = n_e N(Z + 1) \alpha_{fb}(T_e, Z + 1, 0),$$

where $S(T_e, Z, 0)$ is the collisional ionisation coefficient and $\alpha_{fb}(T_e, Z + 1, 0)$ is the radiative recombination coefficient. The above equation leads to the important result that, in a coronal plasma, the population of the ionisation states does not depend upon the electron density and is given by

$$(4.23) \quad \frac{N(Z + 1)}{N(Z)} = \frac{S(T_e, Z, 0)}{\alpha_{fb}(T_e, Z + 1, 0)}.$$

Once again it is assumed that most of the ions are in their ground state, 0, and therefore both the ion populations and the coefficients are relative to the ground level. Also, it is assumed that electrons have a Maxwellian velocity distribution with a characteristic temperature, T_e .

The condition on the electron density, for coronal equilibrium to hold, can be derived from the basic assumption that collisional de-excitation and recombination processes must be inefficient when compared with the radiative processes. Nevertheless it can be shown that, for a given density, there is always a quantum number, above which, this condition is not fulfilled. Therefore one must define a further condition, from an operative point of view, according to experimental criteria. For the purpose of diagnosing He-like and H-like plasmas, one is usually concerned with the

evaluation of spectral line intensities relative to transitions on the ground state from excited levels typically up to $n_u = 6$, corresponding to the so-called $\alpha, \beta, \gamma, \delta$ and ε lines (see par. 5'1.1). Assuming this level as the upper limit for which the coronal equilibrium condition is to be fulfilled, a quantitative evaluation of the criterion for hydrogen-like ions to be in coronal equilibrium is [60].

$$(4.24) \quad n_e \leq 6 \times 10^{10} (Z + 1)^6 T_e^{1/2} \exp \left[\frac{(Z + 1)}{10 T_e} \right] \text{cm}^{-3},$$

where Z is the ion charge and T_e is the electron temperature in eV. In this case, the sum over the spontaneous emission coefficients was performed using tabulated values for hydrogen. Figure 4 shows the dependence of the maximum electron density for which the above condition is satisfied, for hydrogen-like ions from He to Cu. The curve for the hydrogen-like He indicates that, for this plasma species, the electron density must be less than 10^{14} cm^{-3} for coronal equilibrium to hold. In contrast, due to the strong dependence of the density limit upon the Z number of the species involved, hydrogen-like Al plasmas at electron densities up to approximately $5 \times 10^{18} \text{ cm}^{-3}$ can be considered in coronal equilibrium. This is a special case of particular interest in the study of laser-produced plasmas as those described in the following sections. For example, plasmas produced by laser irradiation of a thin Al target, after a few hundreds of picoseconds, reach the conditions of density and temperature given by fig. 4 and can, therefore, be described by using the coronal approximation. In fact, it has been shown [61] that an Al plasma in coronal equilibrium becomes hydrogenic at approximately $T_e \approx 1 \text{ keV}$.

The curve relative to hydrogenic Cu should only be considered as indicative for the very high temperature limit. In fact, the electron temperature required for hydrogen-like Cu to be the dominant ion species is [61] approximately $T_e \approx 13 \text{ keV}$, whereas the dominant species at 1 keV is the Cu XXVI, that is Be-like Cu.

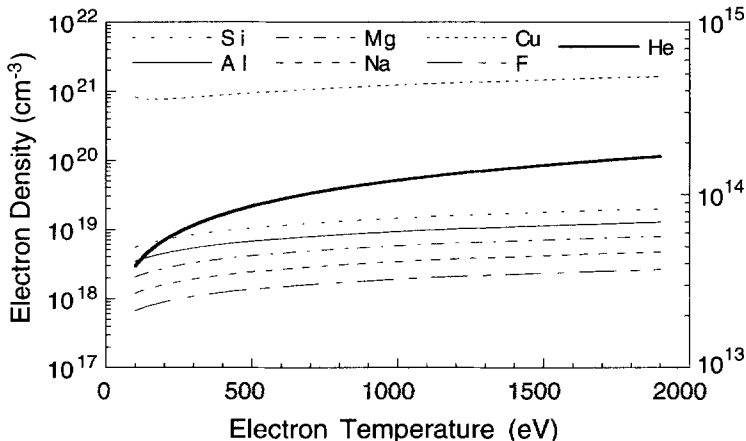


Fig. 4. – Dependence of the maximum electron density for which the condition for coronal equilibrium is satisfied. The density has been evaluated for hydrogen-like ions from fluorine to silicon and for copper. The thicker solid curve has been calculated for hydrogen-like He and the corresponding density axis is given on the vertical axis on the RHS.

4.3.5. Collisional-radiative equilibrium (CRE). If the electron density is neither low enough to satisfy the coronal equilibrium condition, nor high enough for LTE, then we are in the case where both radiative and collisional decay must be taken into account [62]. This so-called collisional-radiative equilibrium can be studied by numerical simulation and is briefly discussed in the next section.

4.4. Atomic physics: temporal scale and related calculations. – On the hypothesis of optically thin plasmas, among all the possible transition processes only radiative excitation and ionisation can be neglected. The electrons still have a Maxwellian distribution. In the general case, a rate equation must be written for each bound level, taking into account all possible transitions, from and to this level. An infinite set of equations is obtained that would be impossible to solve unless some approximations could be made. The typical approach is to set, from case to case, an upper limit to the number of levels to be considered as the population of higher levels becomes very small and eventually can be neglected, without any substantial error being generated.

In addition, as already observed, above some high quantum number level, collisional processes dominate over radiative ones, leading to LTE conditions. Once the truncation is operated, a finite set of equations is obtained which can be solved numerically using the available database on transition rate coefficients.

This approach has been implemented in atomic physics codes like RATION [63] and examples of calculated spectra and line intensity ratios will be given in the following section and compared to experimental spectra obtained in different interaction conditions.

4.4.1. Limits of the steady-state approximation. To calculate the plasma emission spectrum at a given time during the interaction process using a steady-state atomic-physics simulation code, plasma parameters including electron density and temperature at the time of interest are used as input parameters. Therefore, the temporal evolution of the X-ray emission is simply obtained by the evolution of hydrodynamic parameters. In the general situation, however, plasma hydrodynamic conditions may change on a time scale fast compared to the typical time scale of atomic processes. In this case, the populations of excited and ionised states are not in equilibrium, therefore the steady-state approximation is no longer valid, and time-dependent rate equations will have to be solved.

We observe that, although both ionisation and excitation and their inverse processes play a role in determining the response time of the atomic processes, a quantitative analysis of the transition rates shows that excitation and de-excitation processes are in general faster than ionisation and recombination processes. Therefore, excited states of a given ion can be considered, in most cases, in equilibrium with the corresponding ground state.

An estimate of the relaxation time of ionisation processes can be obtained assuming a two level system in which transitions take place from one level to the other. The solution of the rate equation is characterised by an initial transient phase, during which the populations of the two levels relax to the equilibrium condition, with a time constant approximately given by

$$(4.25) \quad \tau = \frac{1}{n_e(S + \alpha_{3b} + \alpha_{fb})} .$$

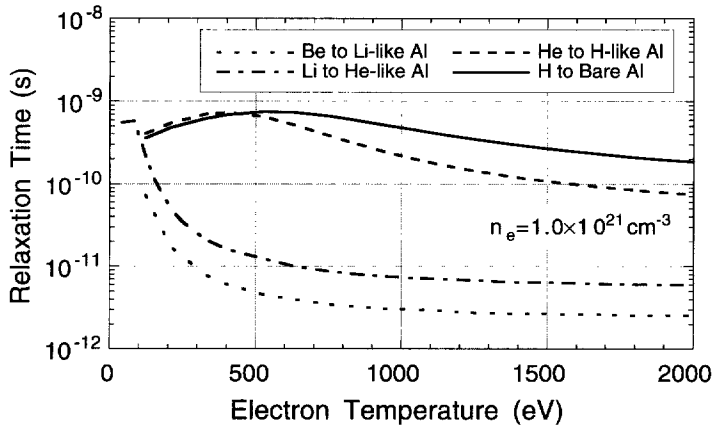


Fig. 5. – Relaxation times of ionisation for aluminium ions from Be-like to H-like as a function of the electron temperature for a density of $1 \times 10^{21} \text{ cm}^{-3}$.

where S and α_{3b} are the collisional ionisation rate and the rate of the inverse process (three-body recombination), while α_{fb} is the radiative recombination rate. The relaxation time given by eq.(4.25) has been evaluated using semi-analytical expressions [64] of the transition rates for the typical case of plasmas produced by laser irradiation of targets consisting of medium-low atomic number elements including aluminium, oxygen and carbon at various ionisation stages from Be-like to H-like ions.

4.4.2. Transient ionisation in Al plasmas. Figure 5 shows the relaxation time for aluminium ions as a function of the electron temperature and for a density of 10^{21} cm^{-3} which is the critical density for $1 \mu\text{m}$ laser light, typical of solid-state, high-power lasers. The density of interest here is the critical density since most of the X-ray

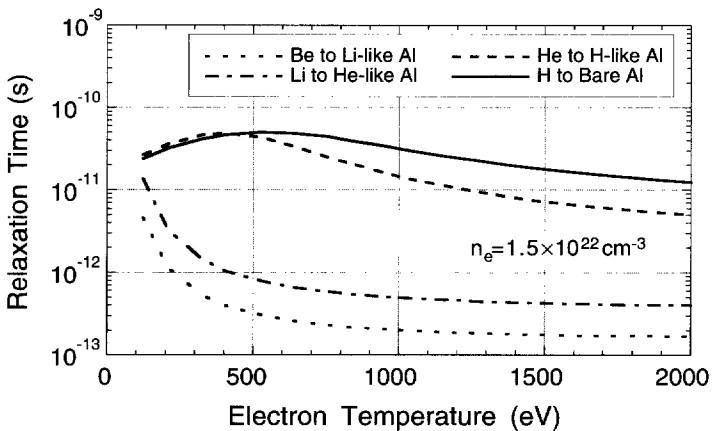


Fig. 6. – Relaxation times of ionisation for aluminium ions from Be-like to H-like as a function of the electron temperature for a density of $1.5 \times 10^{22} \text{ cm}^{-3}$.

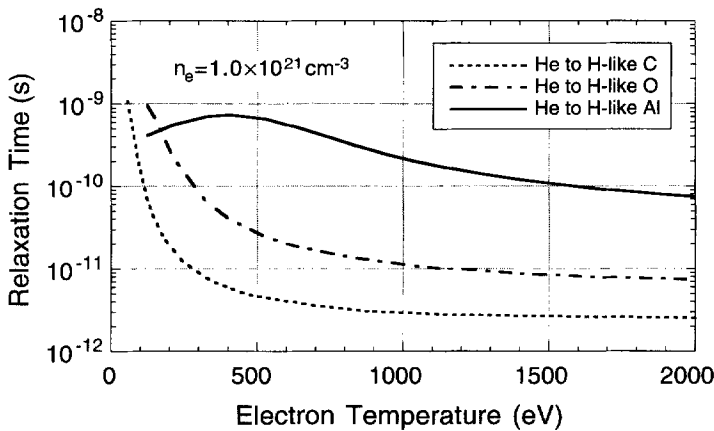


Fig. 7. – Relaxation times of ionisation for carbon, oxygen and aluminium ions from He-like to H-like as a function of the electron temperature for a density of $1.0 \times 10^{21} \text{ cm}^{-3}$.

radiation emitted by the plasma originates from a region close to the critical layer. The plots of fig. 5 show a dramatic increase in the relaxation time from He-like to H-like Al, compared to ionisation from Be-like to Li-like and from Li-like to He-like. This is mainly due to the large increase of the ionisation energy of He-like ions involving the tightly bound *K*-shell electrons.

According to this plot, the time taken by a plasma with an electron density of 10^{21} cm^{-3} , to achieve equilibrium between Li-like ion and He-like ions is of the order of several hundred picoseconds. Figure 6 shows a plot analogous to that of fig. 5, but obtained at a density of $1.5 \times 10^{22} \text{ cm}^{-3}$, which is the critical density at the fourth harmonic ($\lambda = 0.25 \mu\text{m}$) of the neodymium laser.

Relaxation to He-like Al ions is now reduced to a few tens of picoseconds or less,

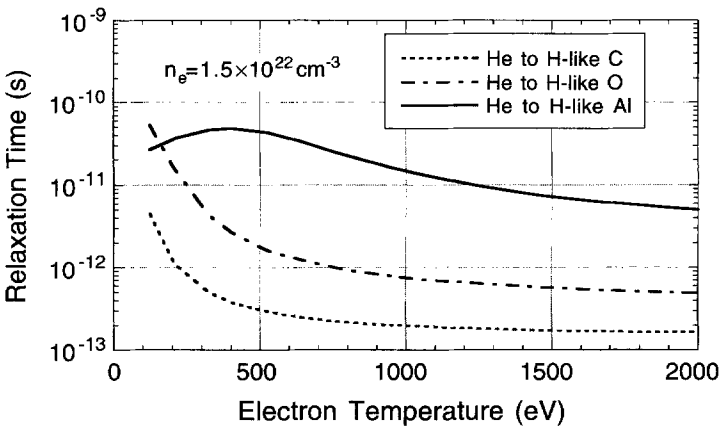


Fig. 8. – Relaxation times of ionisation for carbon, oxygen and aluminium ions from He-like to H-like as a function of the electron temperature for a density of $1.5 \times 10^{22} \text{ cm}^{-3}$.

mainly as a consequence of the scaling of the time constant with the electron density given by eq. (4.25). A steady-state modelling is therefore expected to provide an accurate description of X-ray radiation emitted during plasma formation by nanosecond laser pulses at a wavelength of $0.25\text{ }\mu\text{m}$. In contrast, in the lower density case of fig. 5, that is, in the case of $1\text{ }\mu\text{m}$ laser light, more restrictive conditions are established. According to fig. 5, He-like and H-like X-ray emission during nanosecond plasma formation should be considered in a transient regime. On the other hand, it should be noted that this analysis includes collisional ionisation, three-body and radiative recombination only. Although these are the most important processes, other processes including, for example, charge exchange recombination, can contribute to a faster relaxation.

4.4.3. Transient ionisation in low- Z plasmas. In the case of oxygen and carbon plasmas, equilibrium is established on a picosecond time-scale or, as in the higher density case, on a subpicosecond time scale. Figures 7 and 8 show the relaxation time from He-like to H-like ions for these two atomic species, as calculated according to eq. (4.25), for the two values of the electron density considered above. The corresponding curve relative to the Al plasma is also shown for comparison.

Although a detailed analysis is required, for the particular experimental conditions under investigation from case to case, a general conclusion on the validity of a steady-state model can be formulated on the basis of the results obtained so far and for the particular plasma species considered. The use of medium- Z elements, like aluminium, sets a lower limit on the electron density at which processes involving He-like and H-like ionisation states can be regarded as stationary on a given time scale. In the conditions of laser-produced plasmas using nanosecond pulses, this relaxation time can be as high as several hundred picoseconds. In the case of low- Z elements, ($Z < 10$), plasmas with an electron density above 10^{21} cm^{-3} can be considered stationary on a picosecond time-scale. These circumstances will play a crucial role in the temporal evolution of the X-ray emission.

4.5. Characteristics of laser-plasma X-ray sources. – A laser-plasma X-ray source is generated by focusing a high-power laser pulse onto the surface of a target placed in a vacuum. A schematic view of the interaction is given in fig. 9 for typical laser and plasma parameters. Laser pulse durations can range between a few tens of femtoseconds and tens of nanoseconds with energies ranging from a few mJ to tens of kJ with focused pulse intensities up to 10^{20} W/cm^2 . However, useful X-ray sources for applications can be driven at laser intensities on target as low as 10^{12} W/cm^2 easily achievable by laser systems running in a Q-switch configuration and amplification of the pulse at the 100 mJ level.

For each incident laser pulse an X-ray pulse is emitted, into the 4π solid angle with the angular distribution weakly peaked on the target normal axis. When solid massive targets are used, the X-ray radiation emitted forward is absorbed by the target. Therefore, the angular distribution of the outgoing radiation is physically limited to the solid angle not obstructed by the target. The duration of the X-ray pulse is roughly the same as that of the impinging laser pulse. Quasi-CW X-ray sources can be obtained by focusing high repetition rate pulsed lasers onto suitably designed targets as described in subsect. 6.1.3.

In the case of interaction of nanosecond laser pulses focused on target at moderate intensities, say below 10^{15} W/cm^2 , the leading edge of the focused laser pulse vaporises

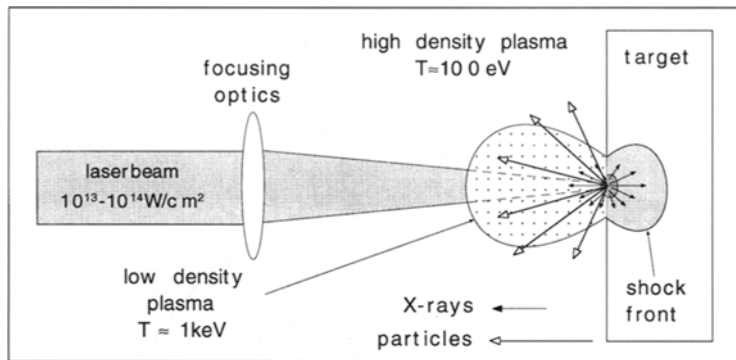


Fig. 9. – Schematic representation of a laser-produced plasma X-ray source. The laser beam is focused on a massive target and produces a high-density plasma from which X-ray and particles are emitted. The low-density, hot-plasma blow-off is also shown which expands in the vacuum towards the laser beam (not to scale).

and ionises the matter at the target surface layer. An expanding plasma is created, which strongly absorbs the remainder of the laser pulse, so that the plasma temperature rises to ≈ 0.1 – 1 keV . The heat, transported through the plasma, vaporises and ablates more target material. This new produced plasma ensures a steady flow from the ablation front that compensates the loss of matter due to hydrodynamic expansion. A highly inhomogeneous plasma is produced whose density increases approaching the target with a scalelength of the order of several hundred micrometers. On a time scale of $\approx 100 \text{ ps}$ a steady-state plasma flow is established, which lasts for the entire duration of the laser pulse. The peak of X-ray emissivity is located in the plasma region which combines both high temperature and high electron density, typically just beyond the critical density surface where electron conduction ensures efficient energy transport.

4.5.1. Spectral distribution. Laser produced plasmas can be regarded as potential sources of black-body radiation [65]. In fact, for typical temperatures of hundreds of electronvolts, a very wide spectrum is emitted, ranging from the infrared to the X-ray region. However, a detailed analysis of the properties shows several important differences. First of all a black body is a physical system at thermal equilibrium, radiating in a pure continuum spectrum while, as discussed in subsect. 4.3, laser produced plasmas are typically far from thermodynamic equilibrium, radiating in a continuum as well as a discrete spectrum. Figure 10 shows a typical radiation spectrum from a laser-produced plasma compared to that of a blackbody at the same temperature [66]. It can be seen that for longer wavelengths the plasma emission approaches that of a black body, as a consequence of increasing reabsorption (inverse bremsstrahlung) that scale as λ^2 . Further, a comparison of the emission from a laser plasma source and a black body shows that plasma emission peaks at wavelengths typically longer than in the case of black-body radiation. In fact, plasma bremsstrahlung continuum emission peaks at a wavelengths ≈ 2.5 times longer than for the black-body spectral distribution (see subsect. 4.1.1).

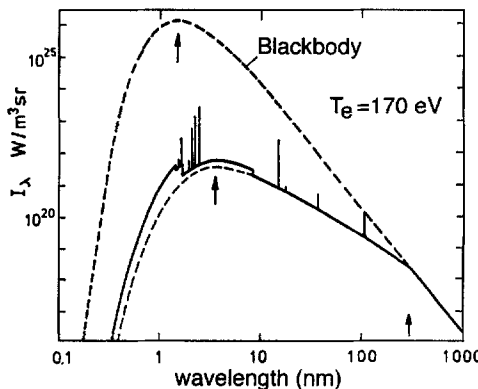


Fig. 10. – Schematic radiation spectrum from a laser-produced plasma compared to that of a black body at the same temperature [66].

As discussed in detail in subsect. 4.1.2, an additional contribution to plasma emission is given by electron-ion recombination processes. The recombination process gives rise to a continuum emission at photon energies greater than the ionisation energy of the recombining ion. Consequently, in a plasma where two or more ionisation stages exist simultaneously, the spectral emissivity is characterised by characteristic “jumps” corresponding to the different ionisation energies, the so-called “recombination edges”.

The discrete components in the plasma electromagnetic emission are due to electron transitions between bound states (see subsect. 4.1.3). Transitions of excited ions to the ground state produce the so-called resonance lines that are of particular interest in plasma characterisation due to the sensitivity of their relative intensity to the electron temperature. Line emission may also originate from doubly excited states of ions. These lines are less intense than the resonance lines and occur at slightly longer wavelength. Their sensitivity to the plasma electron density makes them a primary source of information when the plasma density has to be inferred from X-ray spectroscopic measurements.

When target material of medium-high atomic number (Z) is used, recombination continuum and line emission carry most of the outgoing radiation energy. As an example, in the case of an Al target irradiated by 3 ns pulses at $0.35 \mu\text{m}$ wavelength (third harmonics of Nd:Glass laser) at an intensity of 10^{14} W/cm^2 , 30% of the radiated energy is emitted as lines, 60% as recombination continuum and 10% as bremsstrahlung [67]. The X-ray spectrum calculated in these conditions in the range from 10 eV to 10 keV is shown in fig. 11.

By changing the atomic number (Z), it is possible to control the spectral properties of laser-plasma X-ray sources. Figure 12 shows X-ray spectra of the radiation emitted by plasmas produced by different Z targets over a wide spectral range. The contribution of the different bands is clearly visible. The detailed structure of K -shell line emission as that shown in fig. 11 is not resolved due to the resolution of the wide spectral range of the spectrometer [68].

By using very low- Z targets (plastics) a plasma is produced in which bare (fully stripped) ions are the dominant. The radiation emitted by such a kind of plasmas is

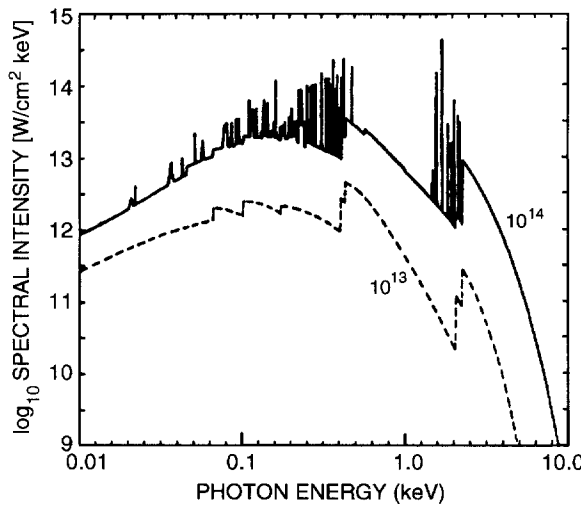


Fig. 11. – Calculated X-ray spectrum from a laser-heated Al target irradiated at intensities of 10^{13} and 10^{14} W/cm² [67].

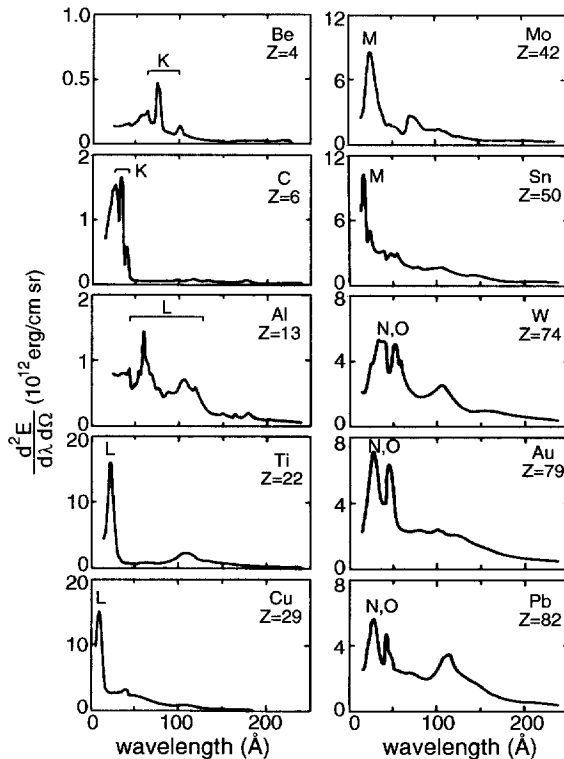


Fig. 12. – Wide range (low resolution) X-ray spectra from plasmas produced by laser irradiation of various Z targets. The intensity of the $0.53 \mu\text{m}$ laser beam was 3×10^{13} W/cm² and the pulse duration was 3 ns [68]. The spectroscopic structure, K , L , M , N , and O refer to the shells from which the emission arises.

almost free from line emission, and the continuum is mainly due to bremsstrahlung emission. For medium values of Z ($Z \leq 20$), the plasma produced is predominantly populated by hydrogen-like through Be-like ions. In these conditions a single line can carry a significant fraction (a few %) of the total X-ray emission energy between 0.5 to 10 keV. Due to the sharpness of emission lines ($\Delta\nu/\nu \approx 100$), their intensity can overcome continuum emission (for the values of Z considered above the recombination overcomes the bremsstrahlung) by several orders of magnitude. Medium- Z X-ray sources are fruitfully used in spectroscopic applications where bright line-emitters are required.

When high- Z targets ($Z \geq 20$) are used, the plasma is populated by ions with several bound electrons. The resulting X-ray spectrum is dominated by a complex many-electron line emission. The density of emission lines in the spectrum is so large that they merge giving an effective band of a quasi-continuum emission which can be hardly resolved even if high-resolution spectrographs are used.

We can see that targets with very low- Z values, as well as with high- Z values basically produce continuum X-ray emission. However, the conversion efficiency of laser energy into X-ray radiation energy increases with Z . So, high- Z targets are preferred as band emitters, when back-lighting sources are required as in the case of absorption spectroscopy.

4.5.2. X-ray pulse duration. Typically, the X-ray pulse duration is comparable with that of the laser pulse producing the plasma. In particular, the rise time of the X-ray emission is mainly determined by the characteristic time needed to heat the plasma while the time scale of plasma cooling sets the fall time of the emission. The main sources of plasma cooling are plasma expansion and radiation emission. With an appropriate choice of target geometry and material, and interaction conditions, the X-ray pulse duration can be substantially reduced. In particular, the use of mass limited targets like thin foils, can ensure that a more efficient cooling occurs due to a more rapid plasma expansion [69, 70].

In the case of plasmas produced by very short laser pulses the duration of X-ray emission may be substantially longer than that of the laser pulse. When a plasma is generated by using a laser pulse of 1 ps duration, X-ray pulses of up to 20 ps duration at photon energy $h\nu \approx 100$ eV can be generated [71]. Ultrashort X-ray pulses have been achieved by using fs laser pulses focused onto solid targets. Figure 13 shows the result [72] of streak-camera (see par. 5.1.2) measurements carried out on the X-ray emission from plasmas produced by laser irradiation of silicon targets with 160 fs laser pulses focused at an intensity of 10^{16} W/cm². The X-ray pulse duration was found to be approximately 2 ps and was obtained from the deconvolution of the streak-camera signal by using the camera response function generated by a 500 fs UV pulse.

On the other hand, the duration of the X-ray emission varies with the considered spectral range. Keeping constant all the physical conditions, the higher the energy of the photons considered the shorter is the duration of the X-ray emission. In fact, higher energy X-rays photons are typically produced by higher plasma temperature regions, which, of course, have a shorter life. As an example we consider two experiments in which 25 ns KrF laser pulses were used. In the first experiment [73] the detection spectral range was at 15 eV $\leq h\nu \leq$ 73 eV and the laser pulse was focused on an Au target at an intensity of 10^{12} W/cm². In this case the half-width of the X-ray pulse

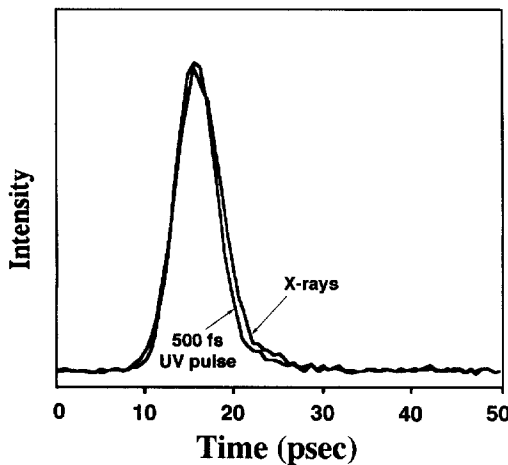


Fig. 13. – Streak-camera measurements of the soft-X-ray emission from plasmas produced by laser irradiation of a massive silicon target with 160 fs laser pulses at an intensity of 10^{16} W/cm^2 . The actual duration of the X-ray pulse (after deconvolution based upon the streak-camera response to the 500 fs UV calibration pulse) was estimated to be approximately 2 ps [72].

was ≈ 40 ns, which is nearly a factor two longer than the laser pulse. In the second experiment [74] the detection spectral range was at $h\nu \approx 1$ keV and the laser pulses were focused on a Cu target at an intensity of 10^{14} W/cm^2 . In this case the half-width of the X-ray pulse is only ≈ 5 ns, which is much shorter than the laser pulse duration. Similar behaviour is expected in the case of ultra-short laser pulses. Figure 14 shows the calculated temporal evolution of the total X-ray emission compared to the emission for photon energies > 1 keV in the case of interaction of a 100 fs laser pulse with a silicon target [75].

Another important factor that can affect the duration of X-ray emission at a high photon energies is the occurrence of laser plasma coupling mechanisms like resonance absorption or two-plasmon decay (see subsects. 3.1-2), that give rise to transfer of energy from the laser e.m. wave in the form of longitudinal electron plasma waves. These waves, due to collisionless damping mechanisms, can produce significant changes in the electron energy distribution function producing a population of "hot electrons" (see subsect. 3.2.6), *i.e.* electrons with high kinetic energy, which is much larger than the corresponding Maxwellian population. Due to bremsstrahlung emission process, these electrons may generate intense fluxes of high energy photons, large compared to the flux produced by the same process in a Maxwellian plasma with the same background electron temperature. In this case, the dynamics of the emission process is related to the history of the laser pulse that acts as an external driving force. Therefore, in contrast with thermal X-rays whose history is dominated by the evolution of the plasma, the duration of X-ray emission at higher photon energies is expected to be comparable with or shorter than the laser pulse duration.

4.5.3. Source size and angular distribution. The plasma plume that develops after laser irradiation of a planar target with a circular focal spot exhibits a cylindrical

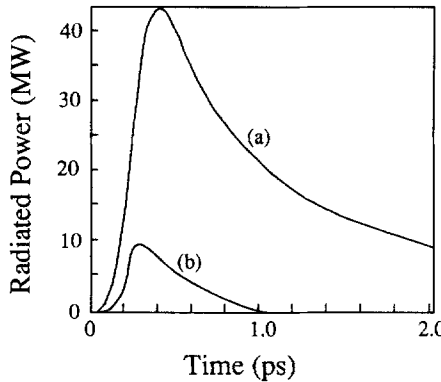


Fig. 14. – Calculated temporal evolution of (a) the total X-ray emission and (b) the emission for photon energies > 1 keV, from plasma produced by the interaction of a 100 fs laser pulse with a silicon target [75].

symmetry about an axis perpendicular to the target surface and centred in the spot. The preferential expansion direction does not depend upon the angle of incidence, which is usually set to be different from normal incidence to avoid detrimental back-reflections into the laser system. In addition, for laser pulse durations shorter than the characteristic times of the plasma hydrodynamic expansion, the X-ray source size is determined by the size of the laser focal spot. In these conditions the plasma emitting volume can be very small: almost a point source, a few micrometers wide.

For laser pulse durations shorter than the typical hydrodynamic expansion times, the X-ray source shows a cylindrical shape, whose diameter is of the order of the focal spot size, while the length is roughly given by the product $c_s \tau$, where c_s is the sound speed (see eq. (2.3)) in the plasma and τ is the laser pulse duration. For even longer laser pulse durations, the X-ray source shows the typical “cigar shaped”, whose longitudinal and transversal dimensions depend on heat transport and matter ablation mechanisms.

The measured X-ray source size strongly depends upon the spectral window of the imaging system, which typically consists of a pin-hole camera (see subsect. 5·4). One finds that the source size decreases when harder X-rays are selected since the plasma region where hotter plasma is generated is smaller. The effect of different filtering conditions on the X-ray image of a laser-plasma is described by fig. 15 which shows X-ray images of a plasma taken by using a 4-channel pin-hole camera as described in subsects. 5·4·1-2.

A detailed discussion of spectral selection effects is given in subsect. 5·4·2. Here we only observe the dramatic reduction of the X-ray source size from the $\approx 90 \mu\text{m}$ of the Be filtered image to the $\approx 30 \mu\text{m}$ of the image additionally filtered with Al and Cu (see also fig. 43).

The angular distribution of X-ray emission from laser-produced plasmas shows a cylindrical symmetry, whose axis is orthogonal to the target surface, regardless of the angle of incidence of the laser beam. Experimentally the angular distribution of X-ray

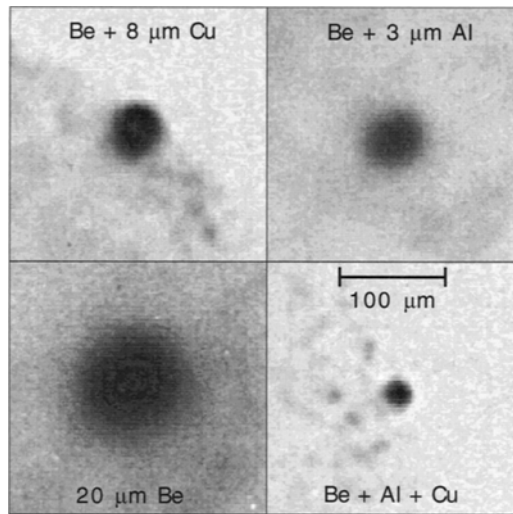


Fig. 15. – X-ray images of a plasma produced by irradiating a solid target with a 10 ps laser pulse focused in a $\approx 25 \mu\text{m}$ diameter spot at an intensity of $3.6 \times 10^{16} \text{ W/cm}^2$. The images have been obtained simultaneously from a single interaction event using a pin-hole camera fitted with a 4-pin-hole array as described in sect. 5.4.1.2. Different spectral windows were selected for each channel by using different filters as indicated [76].

emission is found (see [77] and references therein) to fit the function

$$(4.26) \quad I_\lambda(\theta) = I_\lambda[\cos(\theta)]^n,$$

where θ is the angle with respect to the surface normal, λ is the X-ray wavelength and n is a parameter that ranges, according to the particular experimental conditions, from ≈ 0.3 to ≈ 3 .

4.5.4. X-ray conversion efficiency. The X-ray conversion efficiency, *i.e.* the efficiency of conversion of laser energy into X-ray energy, depends strongly upon the target atomic number (Z) and the laser parameters. Experiments performed using targets of different atomic numbers have shown that the X-ray conversion efficiency varies strongly as a consequence of the atomic shell structure. The plot of fig. 4.13 shows the yield of X-rays between 0.7 and 20 keV emitted by laser-irradiated targets as a function of the atomic number Z [78].

The plasma was generated by 8 ns Nd:Glass laser pulses focused in a $100 \mu\text{m}$ diameter focal spot at an intensity of $4 \times 10^{13} \text{ W/cm}^2$. Figure 16 shows that the emission exhibits four maxima as the atomic number of the target is progressively increased from $Z = 4$ (beryllium) through to $Z = 92$ (uranium). The physical reason of this characteristic behaviour is that, as the Z of the target increases for fixed interaction conditions, the atomic configuration is optimum for the generation of resonance line emission from the K -, L -, M - and N -shells. In general, the behaviour of the X-ray yield as a function of the atomic number depends upon the considered spectral range because the contribution of resonance emission from different shells lies in different regions of the spectrum for different atomic numbers. This is evident from the plots of fig. 12 and is more clearly described by the plot of fig. 17.

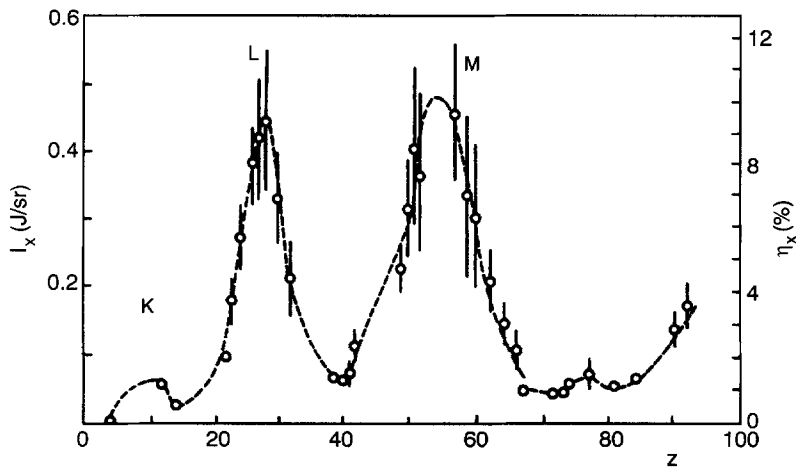


Fig. 16. – Yield of X-ray emission between 0.7 keV and 20 keV as a function of the atomic number of the irradiated target. Maxima of emission are measured when the atomic configuration is optimum for the excitation of resonance lines from K -, L - and M -shells [78].

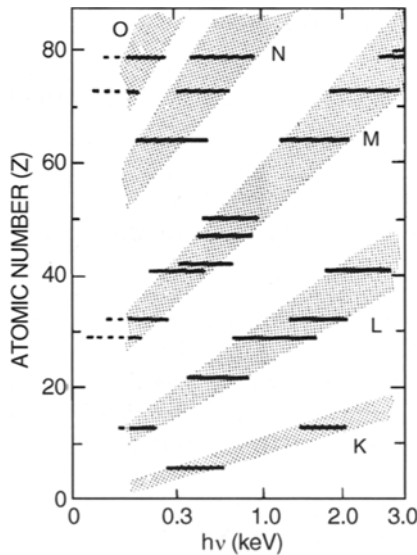


Fig. 17. – Spectral position of plasma emission from different shells as a function of the atomic number. Experimental results (horizontal bars) are compared with calculations (shaded regions) [79].

According to this figure, the atomic number at which maximum emission occurs is a function of the observed spectral range [79]. In fact, the spectral range characteristic of some shell emission (for example L -shell emission), depends on the atomic number of the target. Therefore it is possible to “tune” the X-ray emission from laser-produced plasmas by choosing the atomic number of the target. Clearly, the laser intensity must

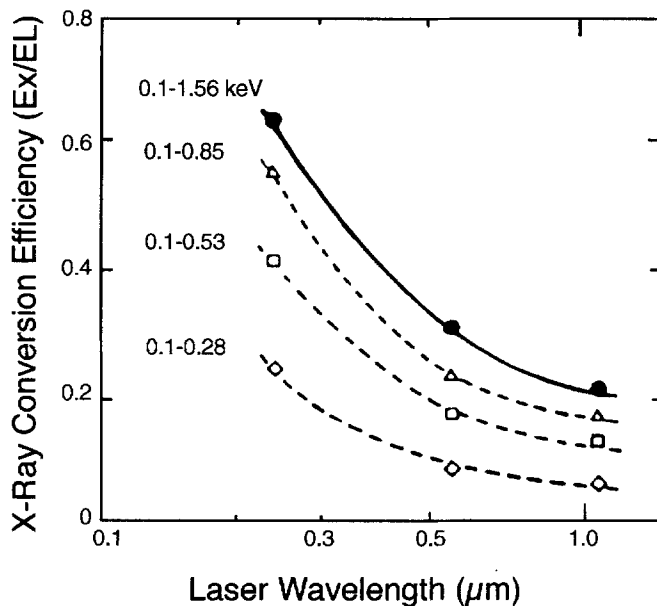


Fig. 18. – Dependence of X-ray conversion efficiency on the laser wavelength for different photon spectral ranges. The plasma was produced by irradiating Au targets with the fundamental ($1.05\text{ }\mu\text{m}$), the frequency doubled ($0.53\text{ }\mu\text{m}$) and the frequency quadrupled ($0.26\text{ }\mu\text{m}$) of Nd laser at an intensity of $7 \times 10^{13}\text{ W/cm}^2$ [80].

be high enough to reach a plasma temperature suitable to excite the considered shell emission.

Several experiments have been performed to investigate the dependence of X-ray conversion efficiency upon laser wavelength. Shorter wavelengths were found [80] to couple more favourably with the target, due to the higher absorption and the smaller fraction of the absorbed energy lost to excite fast electrons as shown in fig. 18.

In fact shorter wavelength laser light can penetrate in denser plasma regions (see subsect. 3'1), where collisional absorption is more efficient and where collisional excitation of ions gives higher X-ray yield. The first clear demonstration of the advantages of using short wavelengths to generate X-ray radiation from laser-produced plasma was given in an important experiment [81]. In that experiment the X-ray conversion efficiency of the fundamental ($\lambda = 1.06\text{ }\mu\text{m}$) and 3rd harmonic ($\lambda = 0.35\text{ }\mu\text{m}$) of a Nd laser were compared. The conversion efficiency of UV laser radiation was found to be ten times higher than that of IR laser light.

Another important experimental parameter that can influence X-ray conversion efficiency is the laser intensity. In fact, the laser intensity on target determines the plasma temperature ($T \propto I^{0.5}$), which in turn determines the degree of ionisation and the efficiency of excitation of the different ion species. Figure 19 shows the conversion efficiency vs. laser intensity on target for Cu and Au targets in two different detection spectral ranges (0.1–0.75 keV and 0.75–2 keV) for a $0.26\text{ }\mu\text{m}$ laser wavelength and 0.5 ns pulse duration [82].

In the case of the low-energy spectral window, the efficiency remains almost

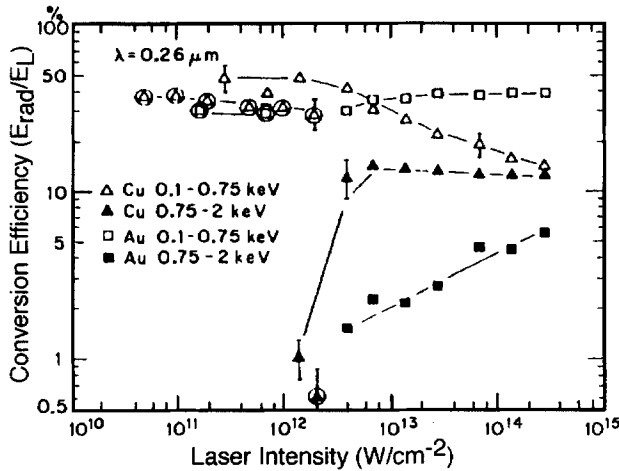


Fig. 19. – Conversion efficiency as a function of laser irradiance on target for Cu and Au targets in two different detection spectral ranges (0.1–0.75 keV and 0.75–2 keV). The laser pulse duration was 0.5 ns and the laser wavelength was 0.26 μm [82].

constant around $\approx 30\%$ for Au and $\approx 50\%$ for Cu up to an intensity of 10^{12} W/cm^2 . The high-energy spectral window shows a different behaviour. In particular, in the case of the Cu target, the conversion efficiency increases above 10^{12} W/cm^2 , due to the excitation of the Cu L -shell emission [82, 83]. For further increase of the laser intensity (above 10^{16} W/cm^2) the conversion efficiency tends to reduce due to a less efficient absorption of laser light (see subsect. 3'1).

From the point of view of laser pulse length it has been shown that [84] the conversion efficiency decreases considerably when going from the nanosecond regime to the picosecond regime as shown in fig. 20. This is due to reduction of the absorbed laser energy with a consequent less efficient conversion of the absorbed energy into X-rays.

In fact, in the nanosecond regime the laser energy is almost completely absorbed by the long scalelength plasma produced in this regime [85, 86] due to efficient collisional absorption, provided that the laser intensity is not too high (see subsect. 3'1.1). In contrast, in the case of picosecond pulses the plasma density scalelength reduces dramatically [87] and therefore collisional absorption becomes ineffective. On the other hand, the efficiency of resonance absorption (par. 3'1.3), which becomes the dominant absorption mechanism, is limited to approximately 50% in conditions of optimum matching of polarisation and angle of incidence.

Finally we observe that laser focusing conditions on target have to be controlled accurately in order to maximise the X-ray conversion efficiency. It is well known that the intensity of the X-ray emission from laser-produced plasmas depends strongly upon the laser focusing configuration on target. The X-ray flux can be maximised by scanning the target position along the beam axis, in the proximity of the nominal focal position. Figure 21 shows the results of an experiment carried out by focusing a 3 ns, Nd laser with an $f/8$ optics [88, 89]. The plot on the left shows the dependence of the X-ray emission as a function of the position of the target surface with respect to the

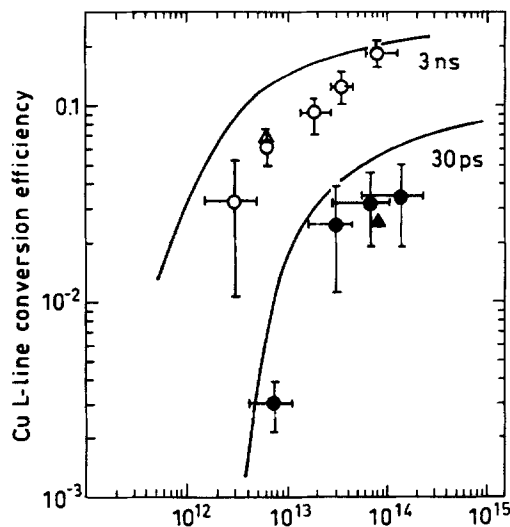


Fig. 20. – Conversion efficiency of line emission from Cu *L*-shell vs. incident laser intensity for two different laser pulse durations. The solid lines are calculations from numerical simulations [84].

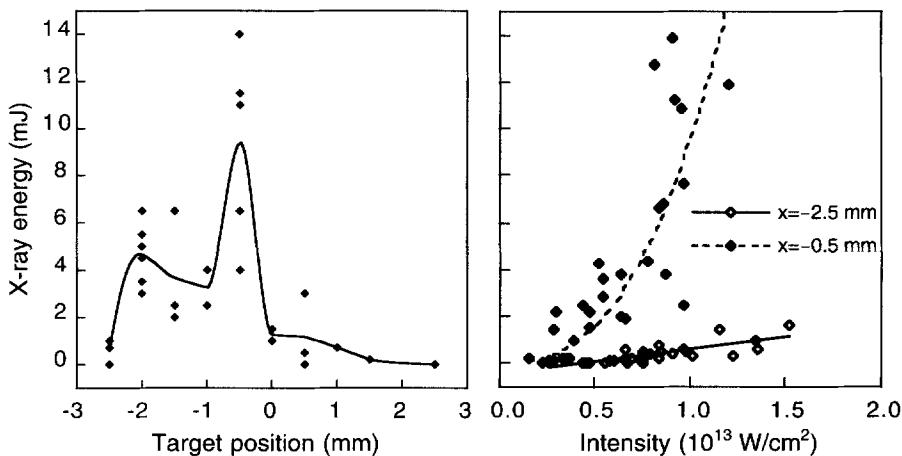


Fig. 21. – X-ray emission intensity as a function of the position of the target with respect to the focal plane (left) and as a function of the laser intensity on target with the target in the position of maximum X-ray emission ($x = -0.5 \text{ mm}$) and in a marginal position (-2.5 mm) [88].

laser beam focal plane. The maximum of the X-ray conversion efficiency is found with the target displaced by 0.5 mm with respect to the position of the beam waist, in the direction of the propagation of the laser light. Such a position of maximum X-ray yield is characterised by a more than quadratic dependence of the X-ray yield upon laser intensity and by a large shot-by-shot variability as shown in the plot on the right.

This behaviour has been explained [20] by taking into account the effect of

filamentation (see subsect. 3.2.4) on local plasma conditions. In fact, when the target is in the optimum position, the laser beam waist lies in the plasma blow-off. In this particular configuration, the plasma can contribute to further focus the laser light due to the filamentation instability, thus enhancing X-ray emission. The variability of the X-ray yield would be, in this case, a consequence of the non-linear character of the filamentation instability. On the other hand, when the target is located in a position where filamentation is not favoured by geometrical effects, the X-ray yield, though lower, becomes much more reproducible from shot to shot and increases linearly with the intensity [88]. It is interesting to observe that measurements of second-harmonic emission intensity *vs.* target position and laser intensity, performed in similar experimental conditions [27] showed a similar behaviour. Very recent measurements [90] based upon second harmonic and X-ray imaging of laser produced plasmas have shown that these emissions are strongly correlated. In this experiment, the X-ray conversion efficiency was found to be maximum in conditions of strong filamentation. Despite the occurrence of filamentation, the X-ray source remains uniform, due to thermal smoothing acting in the plasma region between the laser energy deposition and the X-ray emitting layers.

4.6. X-ray emission in ultrashort pulse interactions.

4.6.1. Femtosecond X-ray sources. The duration of X-ray pulses is a key parameter in their application to the analysis of rapidly evolving phenomena. Typical examples are the investigation on rapidly expanding plasmas, the propagation of shock waves in solids, the study of microscopic living cells and so on. Alternative techniques are being investigated worldwide to achieve ultrashort X-ray pulses by combining fs laser technology and synchrotron radiation sources [91].

As soon as ultrashort laser pulses became available, it was clear that subpicosecond pulses of X-ray radiation could be generated [92] during the interaction of short, intense laser pulses with matter. Later, [93, 94], hard X-ray radiation was also found to be generated. Recently, several experiments [95, 96] have been devoted to the study of ultrafast X-ray emission from laser plasmas. The interaction of high-power femtosecond laser pulses with matter is now established as a powerful technique of generating short intense X-ray pulses with photon energies extending from a few hundreds of electronvolts to the MeV region [53]. Very recently, generation of coherent X-ray radiation in the water window has been reported [97] in the interaction of 5 fs laser pulses with a helium gas jet.

As discussed in sect. 3, collisional absorption mechanisms are inefficient at the intensities considered here. In fact, analytical studies and numerical simulations show that in this regime collisionless processes including resonance absorption [98], vacuum heating [16] and anomalous skin-layer heating [99] play a key role in the absorption of laser energy by the target. It has been shown that these absorption processes lead to non-thermal electron distribution functions. In particular, high-intensity, ultrashort laser heating gives rise to the production of a substantial fraction of highly energetic electrons and a relatively cold background plasma. Energetic electrons give rise, via collisions with ions (bremsstrahlung), to emission of high energy (up to the MeV region) photons in a continuum spectrum while the background plasma accounts for keV or sub-keV line or continuum emission.

As discussed in detail in subsects. 4.1.1-3, X-ray photons are emitted either by radiative de-excitation and recombination processes or by electron-ion collisions

(bremsstrahlung). In particular, the duration of the X-ray pulses depends upon the transient properties of these radiative relaxation processes and upon the lifetime of energetic electrons produced during the laser-matter interaction process. On the other hand, the properties of the radiation also depend upon the type of target used. Mass-limited targets consisting of very thin foils, in contrast with thick (massive) targets, give significant advantages in the production of short X-ray pulses. Advanced numerical simulations and analytical scaling laws developed for femtosecond laser interaction with either massive or thin foils targets [69] consistently predict significantly shorter X-ray pulses. In particular, X-ray pulse lengths comparable to the laser pulse length are predicted when thin targets are used in combination with high-Z material. In this case the target is considered thin when it is completely heated by the thermal wave during the laser pulse.

According to simple considerations on the propagation of thermal heat waves, it can be calculated that the heat penetration depth of absorbed laser energy in 100 fs is of the order of 500 Å [69]. The condition for a rapid fall of the X-ray emission is that the radiation mean free path be much greater than the plasma scalelength. In the case of thin targets, once laser energy is absorbed, the foil explodes immediately, its density rapidly drops and the radiation mean free path soon becomes much greater than the plasma size. Consequently, radiation can escape freely, without undergoing absorption and re-emission and the emission process is rapidly terminated.

As pointed out above, the properties of X-ray emission strongly depend upon the dominant absorption mechanism of laser energy. In some cases, absorption processes have well-known properties that enable to identify their contribution. In a recent experiment [44], the role of resonance absorption in the interaction of high intensity femtosecond laser pulses with thin plastic foils was investigated by exploiting the dependence of this absorption mechanism on the polarisation of the incident laser light. The intensities of hard X-ray emission and specularly reflected second harmonic (SH) of the laser frequency were measured as a function of the polarisation angle of the laser light. While the observed features of the SH emission showed a clear signature of the occurrence of resonance absorption, the intensity of the X-ray radiation was found to be very sensitive to the polarisation, as expected by the resonant enhancement of the *p*-polarised electric field at the critical density typical of resonance absorption. We observe that these results provide a direct way of controlling the intensity of the X-ray radiation in view of applications of similar experimental configurations as sources of hard X-rays.

4'6.2. High harmonics generation. Over the past few years, considerable progress has been made in the generation of coherent X-UV radiation. Besides X-ray lasers, whose working principles are described in subsect. 4'7, important achievements have been made recently in the generation of high-order odd harmonics from the interaction of intense subpicosecond lasers with noble gases and odd and even harmonics from ultra-intense subpicosecond laser interaction with high-density plasmas with ponderomotively-steepened density gradients.

In fact, coherent X-UV radiation can be obtained by focusing short intense laser pulses into gaseous targets thus inducing highly non-harmonic oscillations of the electrons in the Coulomb field of the nuclei. The non-harmonicity of the motion of the electron is responsible for the emission of harmonics of the fundamental laser frequency. However, due to the symmetry of the Coulomb potential, only odd harmonics can be generated. Such harmonics are typically generated by focusing

subpicosecond lasers pulses at intensities ranging from 10^{14} to 10^{16} W/cm^2 into a relatively low density (10^{18} – 10^{19} cm^{-3}) gas target. This ensures that there is insufficient time for electron-ion collision to occur. Therefore, the only mechanism available for ionisation is direct field ionisation due to the laser field itself also known as optical ionisation. However, for sufficiently short laser pulses, electrons in neutral atoms and weakly ionised ions can experience very high laser fields before significant optical ionisation to the next ion stage occurs. The nonlinear character of the mechanism invoked for the production of high-order harmonics is clear if we observe that at an intensity of 10^{16} W/cm^2 the laser electric field is of the same order of magnitude of the Coulomb field experienced by the electron in the first Bohr orbit of the hydrogen atom.

In general, harmonic spectra are characterised by a rapid fall off of the first few (5 th-7 th) harmonics, followed by a plateau, with a relatively sharp cut-off at shorter wavelengths (see for example [100]). The cut-off occurs at a photon energy corresponding approximately to $h\nu = I_P + 3.17U_P$, where I_P is the ionisation potential of the atom and $U_P = (e^2 E_0^2 / 4m\omega_L^2)$ is the ponderomotive energy of the electron quivering in the laser field E_0 oscillating at an angular frequency ω_L . If the laser intensity exceeds the value at which saturation of the harmonic generation process occurs, the previous expression for the ponderomotive energy must be replaced with $U_P(\text{eV}) \approx 9 \times 10^{-14} I_S (\text{W/cm}^2) [\lambda(\mu\text{m})]^2$, where I_S is the saturation intensity [101]. Therefore, the cut-off energy increases with the laser intensity as well as with the ionisation potential. For this reason, due to their highest neutral atom ionisation potential, noble gas are usually employed as gas targets. On the other hand, the laser intensity cannot exceed the value at which excessive optical ionisation occurs. Once the neutral atom has been optically ionised, harmonics are produced from the action of the laser field on the electrons of the ion. Due to the higher ionisation potential, harmonics from ions show a cut-off at higher energy. However, once plasma formation has occurred, the harmonic generation process becomes inefficient due to a loss of matching conditions.

Harmonics up to the 109th of the Ti-Sapphire laser (800 nm) at 74 Å [2] and the 141st of Nd:glass laser (1053 nm) at 75 Å [38] are now routinely generated. Figure 22 shows a spectrum of harmonic emission in the cut-off region generated by the interaction of a 25 fs laser pulse focused at an intensity of $6 \times 10^{15} \text{ W/cm}^2$ on a neon target [101]. Recently detection of harmonics up to the 299th (27.3 Å) of the Ti-Sapphire laser (800 nm) has been reported [102].

An alternative approach to harmonics generation consists in the interaction of high-power lasers with solid targets [103-105]. In this case the laser radiation can interact with the steep plasma density profile essentially in two ways. When high-contrast femtosecond laser pulses are employed, there is no significant plasma expansion during the laser pulse and the laser effectively interacts with the sharp target-vacuum interface. With picosecond (or longer) laser pulses, plasma expansion takes place, nevertheless, if the ponderomotive force is sufficiently large, steepening of the plasma density profile during the laser pulse may occur.

In both situations the harmonics (odd and even) are produced by the relativistic motion of the electrons dragged back and forth across the asymmetric density step. In a recent experiment [104] higher harmonics up to the 15th order have been observed from 130 fs laser-solid interaction using a Ti:Sapphire laser at 815 nm with intensities up to 10^{17} W/cm^2 . In this experiment, it was assumed that the contrast of the laser pulse, i.e. the pulse to prepulse intensity ratio, typically 10^6 , was sufficiently large that

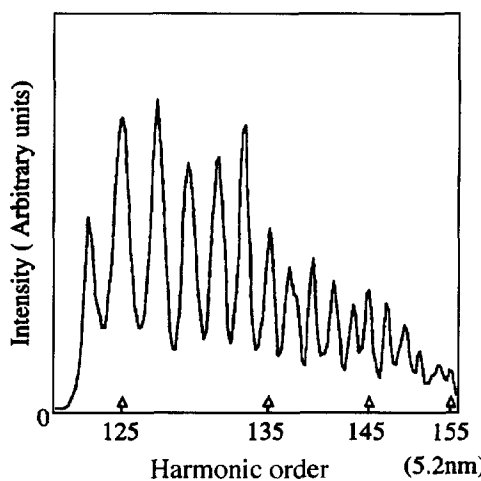


Fig. 22. – Harmonic emission in the cut-off region from the interaction of a 25 fs laser pulse focused at an intensity of 6×10^{15} W/cm² on a neon gas targed at a pressure of 8 Torr [101].

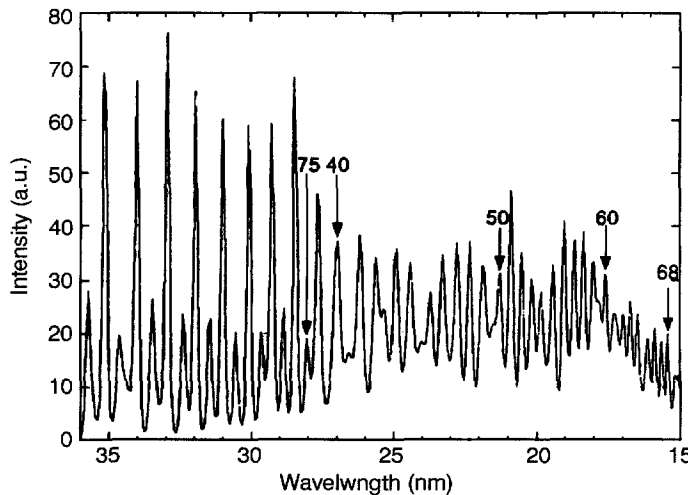


Fig. 23. – Spectrum of harmonic emission in the range 36–15 nm generated by the interaction of a 1.053 μm, 2.5 ps laser pulse focused onto a solid target at an inensity of 10^{19} W/cm² [106].

a vacuum-solid density step could be generated. A narrow beam of harmonics was detected in the specular direction. The reported conversion efficiency was of the order 10^{-8} to 10^{-9} . In another experiment [106] up to the 68th harmonic of 1.05 mm light was observed as shown in fig. 23. The laser intensity on solid target was as high as 10^{19} W/cm², while the conversion efficiency was estimated to range from 10^{-4} to 10^{-6} . The harmonics were found to be emitted into a wide cone, and their generation efficiency was found to be independent of additional prepulse and insensitive to the polarisation of the incident beam.

Harmonics from ponderomotively-steepened plasmas are more competitive than harmonics from gas jet targets as far as spectral brightness is concerned. On the other hand, harmonics generation from gas jet targets requires less powerful laser systems and therefore, in principle, is more attractive in view of a development, in the near future, of a coherent X-UV source. A great effort is being devoted in the development of new techniques to enhance the brightness of harmonics generated from gas jets to the level required by applications like microscopy and microlithography. Recently it has been suggested [102] that phase matching induced by propagation in hollow-core fibres [107] and/or the use of high-pressure gas may greatly enhance the emission intensity.

4.7. X-ray lasers.

4.7.1. Motivation. Since the discovery of the principle of stimulated emission, great effort has been devoted to achieving physical conditions for laser emission at progressively shorter wavelength. In the middle of the 1950's the first maser was built, generating microwaves with a wavelength of a few centimetres. In the 1960's the first optical lasers became to be employed in laboratories, their operating wavelength being a factor 10^{-5} shorter than that of masers. Later, lasers operating in ultraviolet region have been developed, until, in the 1980's, the first demonstration [4] of X-ray lasing was given, at wavelengths 10^{-2} times shorter than that of optical lasers. Due to the intense research devoted worldwide to the development of this kind of sources, X-ray lasing has been achieved in the wavelength range between 400 Å and 35 Å.

Short wavelengths lasers may offer significant advantages in applications like holograms of microscopic biological structures, too small to be investigated with visible light, as well as in many fields of research where coherent, short-wavelength radiation is required, like, for example, holography and interferometry on a submicrometer scale. Nevertheless, severe scientific and technological problems will have to be overcome before lasing at shorter wavelengths can be achieved and before such devices can be routinely available for experiments and applications.

4.7.2. Basic principles. The working principles of an optical and an X-ray laser are basically the same. An intense energy source (flashes, electrical discharge or other) produces a population inversion on electronic levels in the active material. The induced decay mechanism *activates* the material and, in appropriate physical conditions, very intense, highly monochromatic, directional and coherent radiation is emitted.

However, simple considerations show that the power needed to pump an X-ray laser largely exceeds that required by an optical laser. In the simplest atomic model, the energy levels, the transition energy between such levels, and the ionisation energies scale as Z^2 , Z being the effective nuclear charge seen by an outer bound electrons. Therefore, the active material for an X-ray laser operating at wavelength 10^{-2} shorter than that of an optical laser must consist of relatively heavy atoms, whose Z is of the order of 10. The required pump energy for X-ray laser is therefore 10^3 times that of optical lasers, a factor of 10 due to the required ionisation and a factor of 10^2 due to the increased laser levels separation. In addition, due to the scaling of the rate spontaneous decay (as Z^4), this pumping energy has to be released in a time at least 10^4 times shorter than in the case of optical lasers. In fact, the energy transitions involved in X-ray laser schemes are of the order of the keV and the corresponding

lifetimes are of the order of the picosecond while optical transitions are of the order of the eV and with typical lifetimes of the order of microseconds.

According to the scaling laws given above, simple calculations show that the power required to pump the active medium of an X-ray laser is of the order of 100 TW. The only available pumping devices capable of such high power are indeed powerful solid-state laser operating in the sub-nanosecond or picosecond regime or, in principle, CPA Ti:Sapphire lasers operating in a femtosecond regime [36]. For this reason, the research activity on X-ray lasers has been mainly carried out in large laser facilities worldwide.

The matter irradiated at such high-power densities rapidly evolves to a plasma state and X-ray lasers operate on valence electron transitions in highly stripped ions. The active medium of an X-ray laser consists of a large aspect ratio cylindrical target, whose lasant material is a high-density plasma which is pumped by a short- and high-power laser pulse. Since X-ray resonator cavities are not feasible, the laser operates in a high-gain mode in which spontaneous emission is amplified in a single pass of the lasant medium. This represents a serious limitation in the coherence properties of X-ray lasers.

4.7.3. Pumping schemes. In the first demonstration of X-ray lasing action, collisional excitation was achieved by focusing the beam of a high power laser on to a thin, high aspect ratio selenium strip target [4, 108]. In these conditions, target irradiation produces a high temperature (1 keV) selenium ($Z = 34$) plasma whose atoms are rapidly ionised and the outer 24 electrons are set free, leaving neon-like selenium as the dominant species. Electron-ion collisions induce transition from the ground state $1s^2 2s^2 2p^6$ ($2p$ for short) to the higher energy levels like $1s^2 2s^2 2p^5 3s$ ($3s$ for short) and $1s^2 2s^2 2p^5 3p$ ($3p$ for short). Since the transition from the $3p$ to the $2p$ ground state is quantum-mechanically forbidden, while electrons decay very rapidly back to the ground state, a population inversion between the $3p$ and the $3s$ levels is produced. In fact, in this condition 96% of the ions have electrons in the $2p$ state, 3% in the $3p$ state and 1% in the $3s$ state. When transitions from $3p$ to $3s$ are spontaneously produced, 200 Å soft X-ray photons are emitted, that initiate the lasing action by stimulating other similarly excited ions to emit photons of the same wavelength.

The evidence of lasing action is the exponential dependence of the intensity of laser radiation on the length of the lasing medium. Figure 24 shows the spectra obtained for two different plasma lengths [109]. The effect of the exponential amplification of gain line emission is clearly shown.

Typical values of the X-ray laser power are 10–100 MW, in a pulse lasting ≈ 100 ps. Further amplification of this radiation is related to the possibility of producing good multilayer mirrors for soft-X-ray radiation. So the majority of X-ray laser schemes till now have operated in single-pass conditions, *i.e.* in such a way that photons pass through the active medium only once. However, alternative techniques have been proposed and tested in order to increase the length of the active media and to overcome detrimental refraction effects of the X-ray beam in the active medium (see for example [110] and references therein).

Numerous alternative X-ray laser pumping schemes have been tested [111], with the goal of reaching shorter operating wavelengths and higher efficiency. Among them the most promising is the recombination scheme, in which population inversion occurs after recombination of free electrons. However, the output power of the X-ray lasers

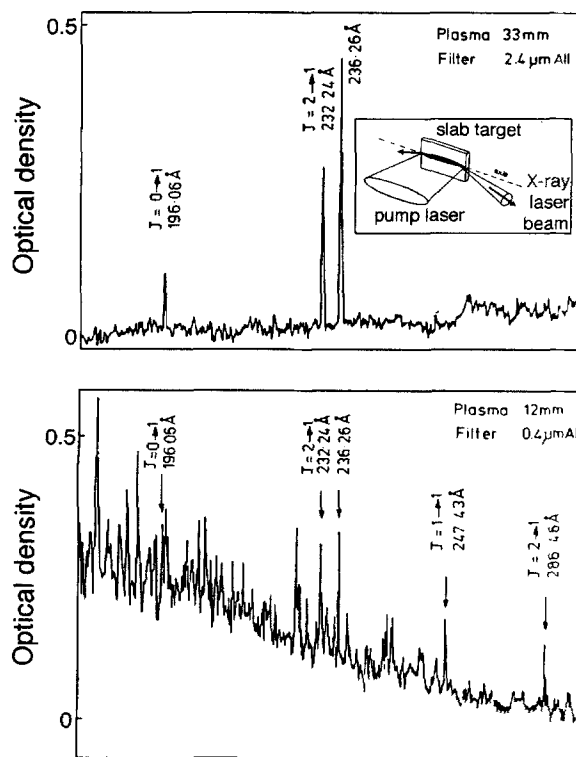


Fig. 24. – Axial spectra for two lengths of irradiated plasma column. The five gain lines are identified in the lower plot. The upper plot shows how the intensity of gain lines increases much more than the other spectral components as the length of the plasma is increased from 12 mm to 33 mm. Note that filtering was increased from $0.4 \mu\text{m}$ for the lower trace to $2.4 \mu\text{m}$ thick Al filter for the upper one [109].

operating in collisional excitation regime has not been reproduced until now by lasers operating with other pumping schemes.

5. – X-rays as plasma diagnostics

Since the early studies on laser interaction with matter, plasma self-emission in the X-ray region has been regarded as a fundamental tool for the investigation of laser-plasma coupling mechanisms. Indeed, in the case of experiments designed to investigate laser-plasma coupling processes or hydrodynamic instabilities, a detailed analysis of spectral and spatial features of the X-ray emission allows a direct monitoring of the modifications induced by the interaction processes on plasma conditions.

As discussed previously, atomic physics processes are strictly related to the thermodynamic properties of the plasma. X-ray line emission from H-like and He-like ions can be investigated in order to study the temporal evolution of plasma properties such as electron temperature and electron density. Experimental line intensity ratios

between resonance emission lines from different ionisation stages present in the plasma can be compared with the analogous ratios calculated in the appropriate plasma equilibrium model. On the other hand, X-ray imaging with high temporal resolution is also considered the key diagnostic technique to study basic interaction processes including, for example, absorption processes, laser induced instabilities and thermal transport (see for example [24]), or to monitor the dynamics in the implosion of inertial confinement fusion capsules [112].

5.1. X-ray spectroscopy.

5.1.1. Spectroscopic techniques. The temporal evolution of plasma physical parameters like electron temperature and density can be inferred by comparison of experimentally measured line intensity ratios with the predictions of atomic physics simulation codes based upon collisional-radiative equilibrium as discussed in sect. 4. The basic idea behind the technique is that, in a given plasma regime, one can identify appropriate spectral components that are highly sensitive to changes of one of the parameters while being weakly dependent on other parameters. In this case, numerical codes can help in identifying the relationship between experimentally measured quantities and unknown plasma parameter(s). A typical example is the measurement of electron temperature from the intensity ratio between emission lines from different ionisation stages. As an illustrative example of experimental temperature measurements from laser-produced plasmas we consider the case of a plasma generated by exploding aluminium targets. In these plasmas strong line emission from highly stripped Al ions, namely, He-like and H-like aluminium ions, occurs. The wavelength and the corresponding photon energy of the most intense resonance lines from these ionic species and the corresponding notation used in the remainder of this paper are reported in table I.

Since the X-ray source size is very small, typically much less than 1 mm, and extremely bright, a simple X-ray spectrometer consisting of a flat crystal set in a first-order Bragg configuration can be employed to perform spectral analysis in the wavelength range from 10 Å down to ≈ 1 Å. Figure 25 shows a schematic arrangement of a TiAP (Thallium hydrogen Phthalate, $\text{TiHC}_8\text{H}_4\text{O}_4$) crystal ($2d = 25.9$ Å) for X-ray spectroscopy of Al laser plasmas in the 5–8 Å spectral range, where K-shell emission from He-like and H-like Al ions occurs.

In this case the crystal simply acts as a multi-layer structure with period d which produces N interfering beams. Therefore, the spectrum of the radiation incident on the plane with an angle of glancing incidence (the complement of the conventional optical angle of incidence) θ is dispersed according to the Bragg equation $n\lambda = 2d \sin \vartheta$, where

Table I. – Wavelength and photon energy of resonance lines from He-like and H-like aluminium. The resonance series of H-like Al ions is labelled according to the analogous Lyman series of the hydrogen atom.

He-like	$\lambda(\text{\AA})$	$h\nu(\text{eV})$	transition	He-like	$\lambda(\text{\AA})$	$h\nu(\text{eV})$	transition
He α	7.75	1600	$1s^2-1s2p$	Lya	7.17	1729	$1s-2p$
He β	6.64	1867	$1s^2-1s3p$	Ly β	6.05	2050	$1s-3p$
He γ	6.31	1965	$1s^2-1s4p$	Ly γ	5.74	2160	$1s-4p$
He δ	6.17	2010	$1s^2-1s5p$	Ly δ	5.60	2214	$1s-5p$
He ϵ	6.10	2032	$1s^2-1s6p$	Ly ϵ	5.53	2242	$1s-6p$

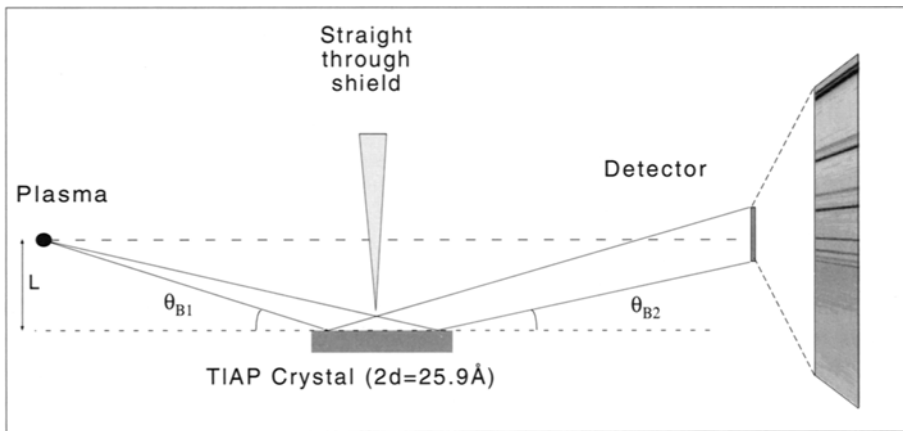


Fig. 25. – Schematic of flat TiAP crystal configuration in the X-ray spectrometer for spectroscopy of highly ionised Al plasmas.

n is an integer that represents the reflection order and λ is the wavelength of the incident radiation. Following simple geometrical considerations [113], the resolving power of this configuration is approximately $\lambda/\Delta\lambda = \sqrt{\tan^2 \vartheta / (\Delta\vartheta_c^2 + (S/L)^2)}$, where $\Delta\vartheta_c$ is the crystal rocking angle, S is the source transverse size and L is the distance between the source and the crystal plane. It is easy to verify that in the typical configuration in laser-produced plasma studies the rocking angle is much smaller than the angular source size and therefore the spectral resolution is limited by the source size. Figure 26 shows an X-ray spectrum from a $6 \mu\text{m}$ thick Al foil irradiated by a 3 ns laser pulse at an intensity of $2 \times 10^{13} \text{ W/cm}^2$. Emission lines from hydrogen-like ($1s-np$) and He-like ($1s^2-1snp$) Al ions can be easily identified once wavelength calibration is carried out.

Once the spectral range of interest is identified, a crystal with the appropriate crystal plane spacing d must be chosen for a given working glancing angle according to the Bragg relation given above. In particular, as the wavelength increases, larger spacings are needed. Since both natural and synthetic crystals have spacings typically less than a few tens of \AA , other dispersing devices must be adopted for longer wavelength X-rays (X-UV).

Grazing incidence gratings can be efficiently used for wavelengths ranging from a few tens of \AA up to hundreds of \AA or more. In fact, grazing incidence ensures a very high reflectivity of gratings coated with medium/heavy metals at relatively high photon energy. Also, variable groove spacing [114] allows the dispersed radiation to be focused onto a plane rather than onto curved surface as in standard gratings. Such a feature makes this grating suitable for use with flat detectors such as film plates or streak-camera photocathodes. Figure 27 shows a schematic set up for a grazing incidence grating equipped with a hard X-ray filter that enables to cut off high energy photons ($> 1 \text{ keV}$) for measurements in the range above $\approx 15 \text{ \AA}$.

The high-energy cut-off filter also uses the properties of X-ray reflection at grazing incidence angles. In this case the process is used to select the required spectral range while rejecting unwanted high energy photons which, if allowed on the grating, can contribute to the first-order spectrum with higher diffraction orders. Figure 28 shows

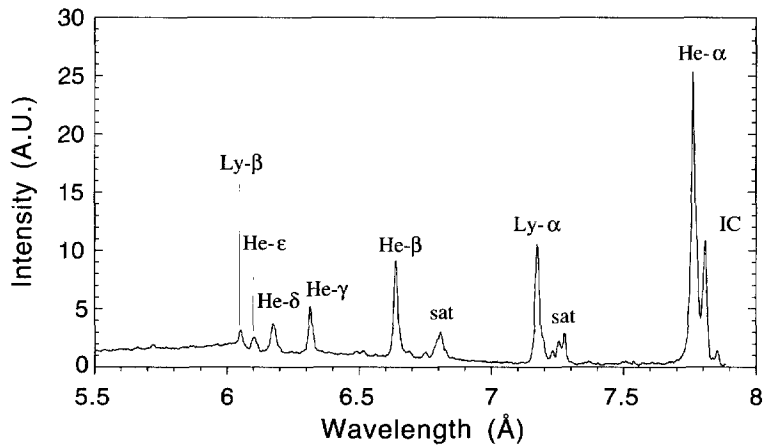


Fig. 26. – Lineout of an X-ray spectrum from a hot aluminium plasma, obtained from a crystal spectrometer on an X-ray film as shown schematically in fig. 25. The main line emission components from hydrogen-like and helium-like aluminium ions are identified.

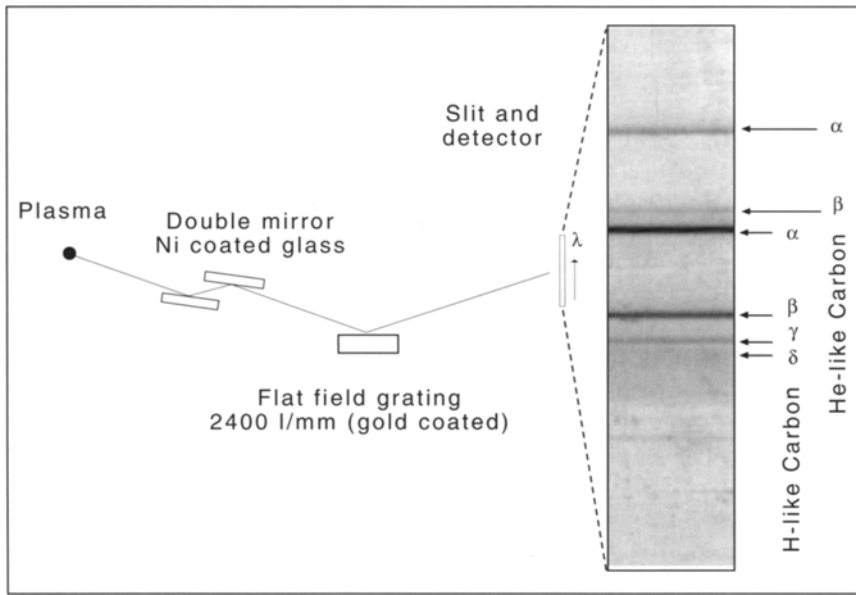


Fig. 27. – Schematic diagram of the experimental arrangement of the flat-field X-UV grating showing the double-reflection filter used to cut off high-energy (> 1 keV) photons. Also shown is a spectrum from a hot carbon plasma produced by laser irradiation of a plastic target (see fig. 28) showing the main line emission components from highly ionised (hydrogen- and He-like) carbon atoms.

a spectrum from a highly ionised carbon plasma generated by the interaction of a 12 ps laser pulse with a plastic target at an intensity of $\approx 2 \times 10^{14} \text{ W/cm}^2$ [76]. In this case the double reflection mirror was implemented using two highly parallel, highly

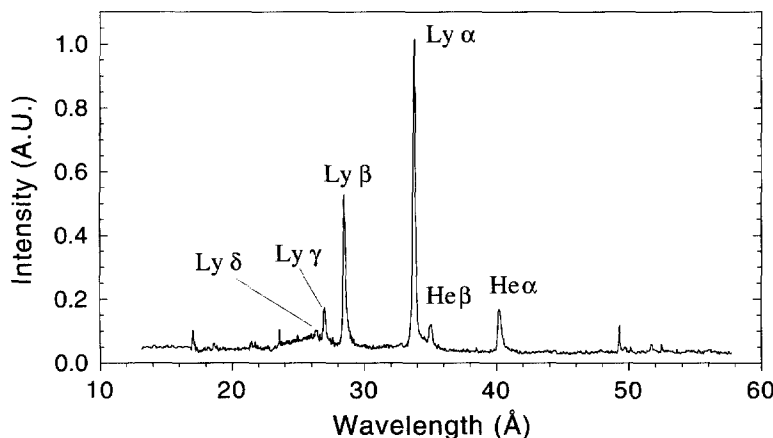


Fig. 28. – Time integrated spectrum of the X-ray radiation from the plasma produced by irradiation of a solid plastic (Mylar) target with a 12 ps, 268 nm laser pulse at an intensity $\approx 2 \times 10^{14}$ W/cm² in a 200 μm diameter focal spot. The spectrum was obtained by using the grazing incidence grating spectrometer shown schematically in fig. 27.

polished, Ni-coated silica substrates placed on the path of the radiation before the grating as shown in fig. 27. The high-energy cut-off edge of the filter is defined by the L -shell absorption edge of Ni atoms located at approximately 860 eV. Below this value the reflectivity of the Ni-coated surface is very close to unity ($\approx 95\%$) provided the incidence angle is ≤ 50 mrad.

A comparison of experimental line ratios measured from spectra like that of fig. 28 with synthetic spectra calculated by atomic physics codes [63] yields an estimate of the time-averaged electron temperature. If the history of the electron temperature is required, spectra must be resolved in time.

5.1.2. Time-resolved analysis. The analysis of the temporal evolution of the emission requires the use of fast detectors with sub-nanosecond temporal resolution. X-ray photodiodes are typically employed for broad-band spectroscopic analysis in combination with X-ray filters [20]. When one-dimensional or two-dimensional analysis is required, special devices are employed in which secondary electron emission is used to convert radiation into electrons while preserving its temporal evolution [115] and spatial distribution. Typical examples of such devices will be described in the following section and examples of applications will also be given. The X-ray streak-camera is a fast, one-dimensional detector that can be used to perform time-resolved analysis of X-ray spectra. Figure 29 shows schematically the working principle of such a device. Photons, incident on the photocathode induce emission of secondary electrons which are accelerated and driven onto the output phosphor screen, through two parallel plates. When a high-voltage ramp is applied to the plates, the time-varying electric field “streaks” the electron beam across the phosphor plate, thus displaying the temporal evolution of the incident radiation in the form of a space-dependent intensity pattern. The direction perpendicular to the streaking direction is relayed directly onto the output screen.

Such a device enables time-resolved analysis of a one-dimensional radiation pattern.

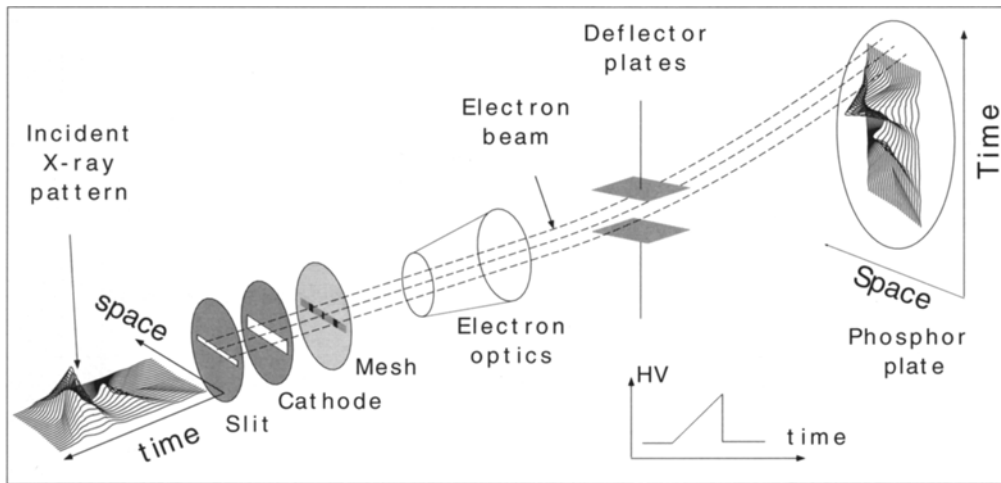


Fig. 29. – Schematic diagram of a streak-camera. The radiation, incident on the photocathode, produces secondary electrons that are accelerated and focused on a phosphor plate. A high voltage ramp, applied in a direction perpendicular to the propagation direction displays the temporal evolution on the output screen.

The temporal resolution of such a device, *i.e.* the shortest temporal interval that can be resolved or the measured duration of a delta-like temporal emission, is determined by the width of the pattern along the temporal axis. This width is typically controlled by placing a narrow slit in front of the streak-camera photocathode. Slits as narrow as a few tens of millimetres can be used with presently available streak-cameras leading to a temporal resolution as high as a few picoseconds. The limit resolution is determined by the physical properties of the photocathode, *i.e.* by the properties of secondary electron emission for the particular photosensitive material chosen. CsI is a typical choice due to the high efficiency. However, when a temporal resolution better than 10 ps is required, KBr is a better choice. In fact, although less sensitive than CsI [116], KBr photocathodes allow a better temporal resolution due to the narrower energy distribution of secondary electrons [117].

5.1.3. Temperature measurements from X-ray spectra. When an X-ray spectrum like that of fig. 27 is generated on the slit of an X-ray streak-camera, it can be resolved in time with a temporal resolution as high as a few picoseconds. Figure 30 shows a typical time-resolved spectrum of the X-ray radiation emitted by a plasma produced by laser irradiation of a thin Al disk target at a total intensity of $6.5 \times 10^{13} \text{ W/cm}^2$ and a pulse duration of 600 ps. Figure 31 shows a 1D trace taken 500 ps after the peak of X-ray emission and integrated over the instrumental temporal resolution of 50 ps. Emission lines from He β to Ly δ are clearly visible with the Ly γ and Ly δ emerging from the He-like continuum. The He ϵ line is just visible as a shoulder-like feature on the long-wavelength side of the Ly β line.

Line intensity profiles can be well fitted using Gaussian profiles with $\Delta\lambda_{\text{FWHM}} = 40 \text{ m}\text{\AA} \pm 10\%$. Except He ϵ and Ly β lines, all the remaining lines are well resolved and it is therefore relatively simple to determine the line intensity. With the available

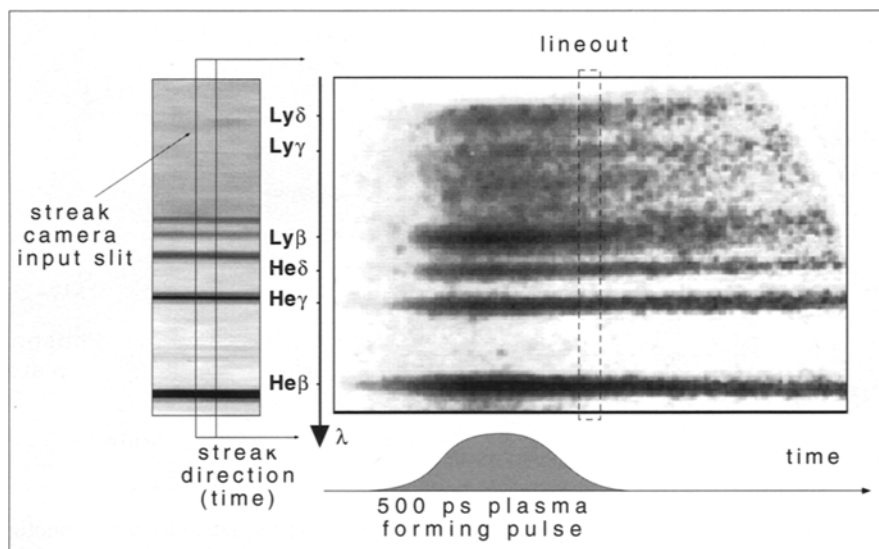


Fig. 30. – Time-resolved X-ray spectrum of K -shell aluminium emission from plasma formed by laser explosion of a thin Al foil heated at an irradiance of $6 \times 10^{13} \text{ W/cm}^2$ by four 600 ps FWHM, $1 \mu\text{m}$ laser pulses. The timing of the heating laser pulse is schematically shown by the bell-shaped curve. The *lineout* box refers to the plot of fig. 31 [10].

spectral resolution, the $\text{Ly}\beta$ line is only partially resolved, being merged to the $\text{He}\gamma$ and higher quantum number He-like lines and to the He-like continuum edge.

Intensity ratios involving the $\text{Ly}\beta$ transition will consequently be affected by a larger error. Brighter emission from hydrogen like transitions occurs at higher heating laser intensities as hotter plasmas are generated. This effect is clearly shown

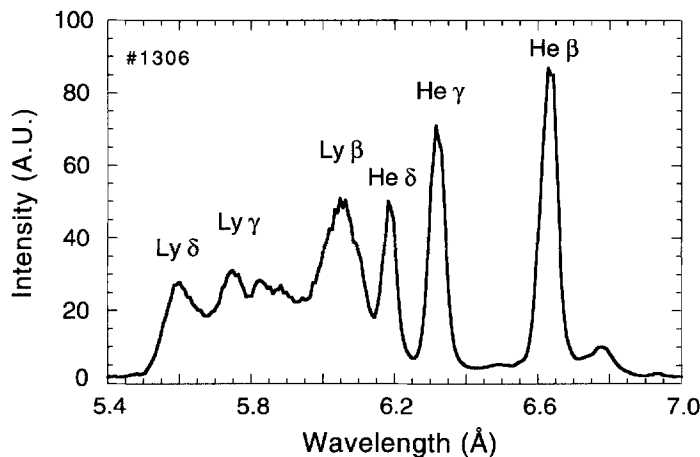


Fig. 31. – Lineout of the spectrum of fig. 30 taken 500 ps after the peak of X-ray emission intensity and integrated over 50 ps, *i.e.* over the temporal resolution of the spectrum (see fig. 30).

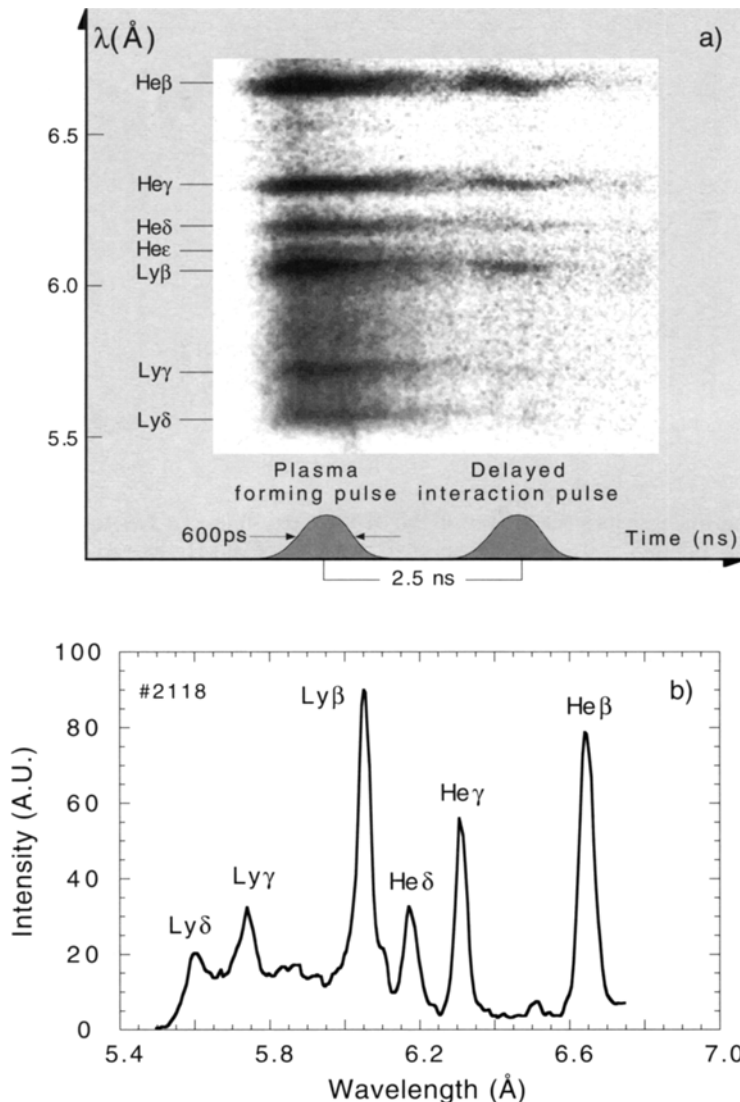


Fig. 32 – a) Time-resolved X-ray spectrum of K -shell Al emission from a laser plasma heated at an irradiance of $1.2 \times 10^{14} \text{ W/cm}^2$ by four 600 ps FWHM, $1 \mu\text{m}$ laser pulses. The effect of a second “interaction” pulse delayed by 2.5 ns with respect the peak of the plasma-forming pulse is also visible. b) Lineout of the spectrum of a) at the peak X-ray emission intensity showing brighter emission from hydrogen-like ions in comparison with the analogous plot of fig. 31.

by fig. 32a) and the corresponding 1D profile of fig. 32b) which shows a time-resolved spectrum obtained in similar conditions as fig. 30 but with a heating laser intensity of $1.2 \times 10^{14} \text{ W/cm}^2$. Also visible in this spectrum is the X-ray emission arising from a delayed interaction laser pulse set to reach the plasma 2.5 ns after the peak of primary heating pulses. The effect of the delayed interaction on the conditions of the preformed plasma will be discussed in detail later in this section. However, it is important to notice

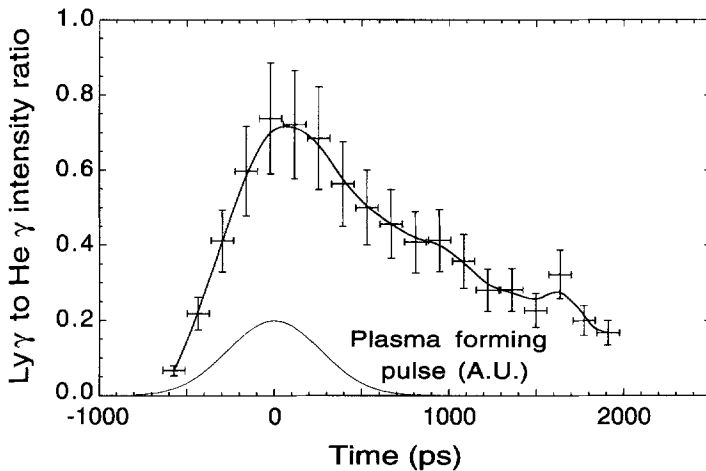


Fig. 33. – Experimental intensity ratio of the H-like Al γ -line ($1s-4p$) to the He-like Al γ -line ($1s^2-1s4p$) as a function of time with respect to the peak of the He-like Al β -line, measured from the spectrum of fig. 32.

that the spectral resolution for this part of the spectrum is clearly improved due to the smaller spatial extent of the X-ray source. In fact, in this case the X-ray emission comes from the region of plasma heated by the interaction beam, whereas the initial part of the spectrum comes from the whole heated plasma.

The higher heating intensity produces a higher electron temperature and therefore higher hydrogenic population that gives rise to stronger Ly γ and Ly δ which now clearly emerge from the He-like continuum in the spectrum of fig. 32. The Ly γ to He γ intensity ratio measured from the spectrum of fig. 32, limited to the heating phase only, is shown in fig. 33. Plots like this, compared with numerical simulations of atomic physics and hydrodynamics yields the history of plasma electron temperature.

It is clear that, since no spatial resolution is included in the spectra, plasma parameters determined in this way should, in principle, be regarded as averaged over plasma electron temperature and density distribution in space. In particular circumstances, like in the case of very hot plasmas (characterised by high thermal conductivity) or highly localised heating, a nearly complete knowledge of the electron temperature in the region of interest can be obtained.

5.2. Plasma opacity.

5.2.1. Opacity effects in temperature measurements. In order to minimise the contribution of opacity effects, it is always preferable to restrict the analysis of line intensity ratios to high quantum number members of a resonance series which are less sensitive to reabsorption effects. On the other hand, line intensity decreases dramatically going towards high quantum number members resulting in low signal-to-noise ratios. Therefore, the final choice will be to find a middle course between these two limits.

Recalling the previous example of temperature measurements, the intensity ratio between Ly γ and He γ was calculated for a uniform plasma as a function of the electron

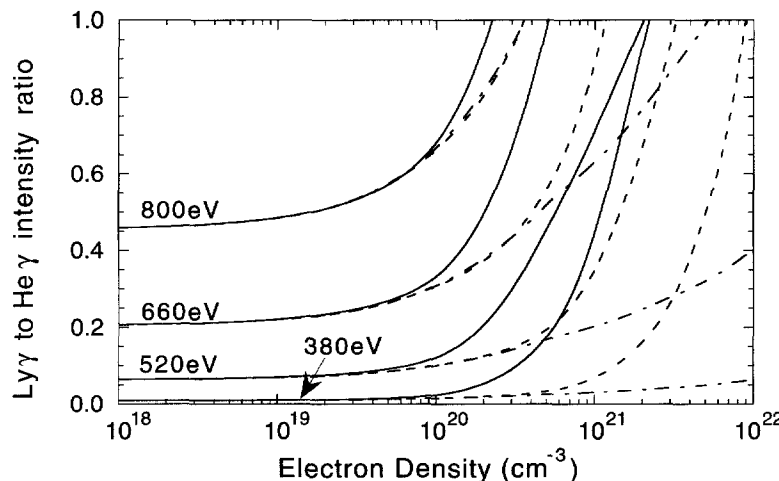


Fig. 34. – Ly γ -to-He γ intensity ratios as a function of electron density for different electron temperatures. Solid line curves have been obtained with no opacity included in the calculation while dashed and dashed-dotted lines correspond to calculation with opacity effects for a 10 μm and a 100 μm thick plasma, respectively.

density and temperature for optically thin and optically thick plasma of 10 μm and 100 μm lengths. The results of such a calculation are summarised in fig. 34 for an electron density ranging between 10^{18} and 10^{22} cm $^{-3}$ and for temperatures between 380 and 800 eV. We notice that, for densities below a few times 10^{19} cm $^{-3}$ the intensity ratio is almost independent of both density and opacity effects. However, in the range of densities between a few times 10^{19} cm $^{-3}$ and a few times 10^{21} cm $^{-3}$, there is a strong dependence of line ratios upon density. Also opacity effects strongly affect line ratios only for densities above 10^{20} cm $^{-3}$.

Once the density of the plasma is known, a plot like that of fig. 34 can be used to convert line ratios into electron temperatures. Figure 35 shows the temporal dependence of the electron temperature obtained by comparing the experimental intensity ratios of fig. 33 with the plot of fig. 34. Each curve of the graph was obtained comparing the experimental ratio with the calculated one and assuming an opacity effect with a given length of homogeneous plasma for the three plasma lengths taken into account in fig. 34.

Due to the lower background electron density after the full explosion of the target, *i.e.* later than about 1 ns after the peak of heating pulses, density and opacity-dependent effects become less important and, in principle, more accurate temperature measurements are possible. In fact, the plot of fig. 35 shows that opacity effects give a major contribution during the laser pulse while later in time the three curves approach each other and give a better defined electron temperature within less than 100 eV. In particular, at 2 ns, when the electron density is of the order of a tenth of the critical density the average electron temperature is found to be 550 eV with an uncertainty due to opacity smaller than 8%.

5.2.2. Laser reheating of preformed plasmas. Well-defined plasma heating conditions can be achieved when a high-intensity laser pulse is focused onto a

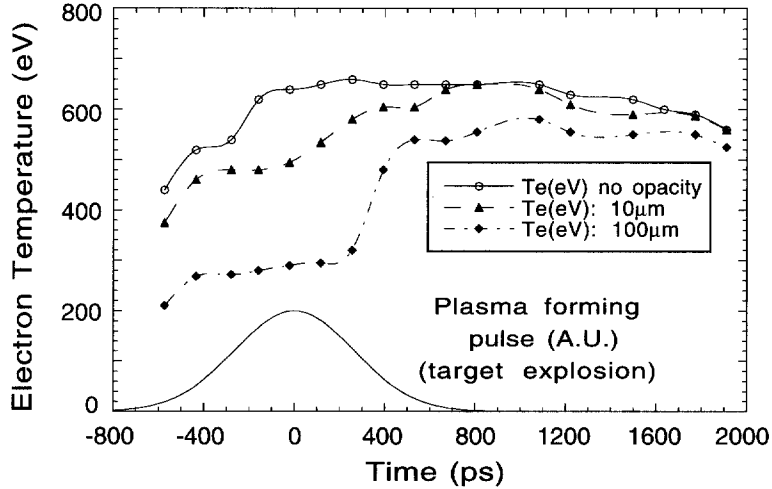


Fig. 35. – Temporal evolution of the electron temperature of a laser-produced Al plasma obtained by comparison of the experimental intensity ratio of $\text{Ly}\gamma$ to $\text{He}\gamma$ with the prediction of the steady-state collisional radiative numerical code RATION [63].

preformed plasma. A great deal of information can be gained from a spectroscopic analysis of the X-ray radiation emitted during the heating process as well as from X-ray imaging studies (see subsect. 5.4). When a laser pulse strikes a long-scalelength preformed plasma, energy is absorbed locally and gives rise to a rapid reheating of the interacting plasma region, with intense re-emission of X-ray radiation. This localised heating will be discussed in detail in subsect. 5.4 (see for example fig. 47). Here we examine the interaction from a spectroscopic viewpoint using the same diagnostic and analysis tools described above. A typical example of plasma re-heating has already been shown in fig. 32 and can be more clearly observed in the spectrum of fig. 36 where the first X-ray emission peak generated during plasma production by laser explosion of a small Al disk, as in the case of fig. 30, is followed by a second emission peak, due to the interaction of a second laser pulse focused on the plasma produced by the first.

The electron temperature of the X-ray emitting region can be determined following the procedure described above. Figure 37 shows the temporal evolution of the electron temperature obtained from the spectrum of fig. 36. Due to the high intensity of the interaction laser pulse, strong line emission up to $\text{Ly}\delta$ and $\text{He}\delta$ was detected and, therefore, the electron temperature could be measured taking into account both the $\text{Ly}\gamma$ to $\text{He}\gamma$ and the $\text{Ly}\delta$ to $\text{He}\delta$ intensity ratios. The plot shows that, in the conditions considered here, a delayed laser pulse interacting with an underdense plasma can give rise to an increase of the electron temperature in the interaction region of up to 200 eV. The difference in the values of the electron temperature obtained from the two line ratios considered here is accounted for by the error bars included in the plot of fig. 37.

Consistently with the analysis of fig. 35 given above, the uncertainty induced by opacity effects on the plot of fig. 37 minimises around 2 ns. Nevertheless, when the interaction pulse strikes the plasma, the error bar increases again suggesting a new

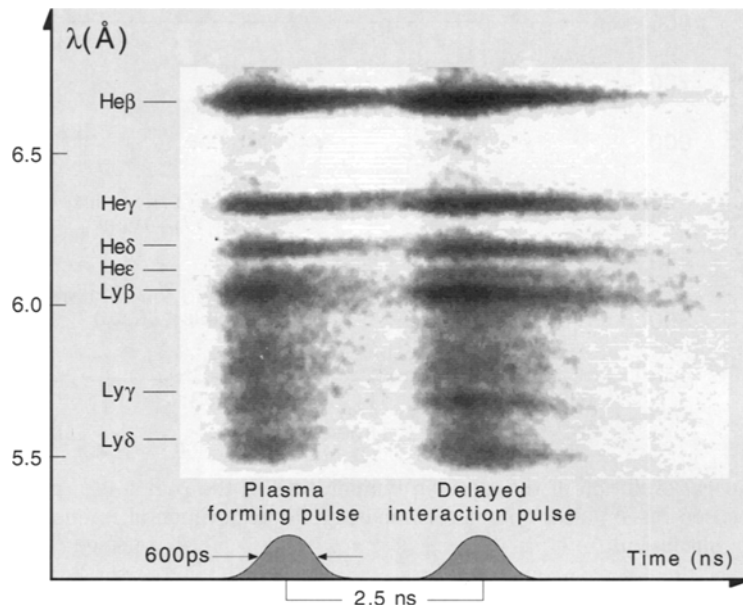


Fig. 36. – Time-resolved X-ray spectrum of K -shell aluminium emission from a laser-plasma heated at an irradiance of $1.2 \times 10^{13} \text{ W/cm}^2$ by four 600 ps FWHM, $1 \mu\text{m}$ laser pulses. The interaction beam is focused on the plasma in a $800 \mu\text{m}$ by $100 \mu\text{m}$ line focus at an intensity of $3.0 \times 10^{14} \text{ W/cm}^2$ and was delayed by 2.5 ns with respect to the peak of the heating pulse.

source of uncertainty. In fact, since the interaction pulse gives rise to localised heating of the underdense plasma, the effect of spatial integration over the entire plasma may come into play. Space-resolving techniques can be adopted to further reduce measurement uncertainty in these circumstances.

5.3. Plasma density. – As discussed above, a correct characterisation of the X-ray emission properties of laser plasmas requires a detailed knowledge of the electron density distribution. Interferometric techniques can be used to measure the electron density distribution of a plasma as well as its temporal evolution. A fringe pattern is generated by the interferometer which gives information on the refractive index of the plasma integrated along the line of sight. Under special experimental conditions and with appropriate assumptions on the symmetry of the plasma, the Abel inversion technique allows the density distribution to be obtained at a given time during plasma formation or expansion with a temporal resolution given by the length of the laser pulse used as a probe beam. An example of an interferometric study of a plasma produced by laser explosion of an Al disk target is shown below along with a brief description of the Fourier transform technique [118] used [10] to analyse the interferograms.

5.3.1. Interferometer set up for phase shift measurements. In the experiment described below, a 100 ps, $1 \mu\text{m}$ wavelength laser pulse was frequency-doubled, delayed, and used as a probe beam parallel to the plane of a 500 nm thick and $400 \mu\text{m}$ diameter disk target. A modified [119] Nomarski interferometer [120] was

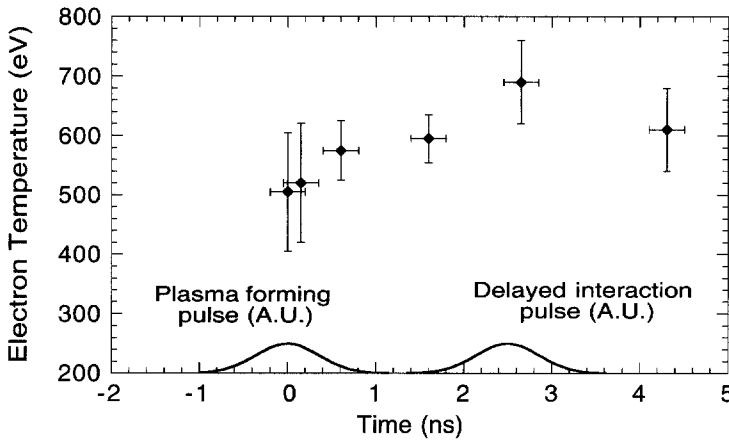


Fig. 37. – Temporal evolution of the electron temperature of the region of a pre-formed plasma heated by a focused laser pulse, obtained comparing the experimental intensity ratio of fig. 36 with numerical calculations.

employed in order to measure the phase shift induced by the plasma on the probe beam.

The technique [121] is based upon a polarised light interferometer which produces, by means of a Wollaston prism, two separate orthogonally polarised images of the plasma surrounded by an unperturbed background. Interference between each of the two images and the unperturbed background of the other images is achieved by placing a polariser before the detector plane, oriented at 45 degrees with respect to the two axes of polarisation of both images produced by the prism. The fringe pattern is then recorded onto a 2D detector (film/CCD).

5.3.2. Experimental results. Figure 38 shows an interferogram taken 4.3 ns after the peak of the plasma forming pulse incident each side of the Al disk target at an irradiance of $4.2 \times 10^{13} \text{ W/cm}^2$. The geometry of the experiment is schematically shown in the inset of fig. 38.

Only one of the two fringe systems produced by the interferometer is entirely shown in this figure. Fringes on the extreme right-hand side of the image are perturbed due to the overlapping with the other fringe system. The original position of the target is marked by two arrows and the edge of the target holder is just outside the image. The interferogram shows that, away from the target plane, the plasma extends up to distances from the longitudinal axis greater than the target radius and, in the limit of sensitivity of the interferometer, it is free from strong density perturbations.

5.3.3. Basic principles of time-resolved interferometry. The fringe pattern produced by the interferometer is the result of interference between a beam which has propagated through the plasma and an unperturbed reference beam, both beams originating from the same laser source. For a probe beam propagating along the y -axis,

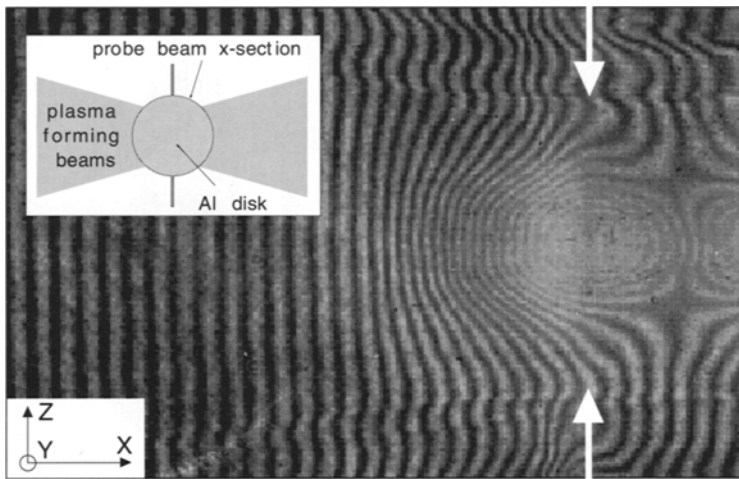


Fig. 38. – Interferogram of the preformed plasma taken 4.3 ns after the peak of the plasma-forming laser pulses. The laser irradiance on each side of the dot Al target was $4.2 \times 10^{13} \text{ W/cm}^2$.

the phase difference between these two beams at a given position (x, z) is given by

$$(5.1) \quad \Delta\phi(x, z) = \frac{2\pi}{\lambda_p} \left(\int_{-L/2}^{L/2} (n(x, y, z) - 1) dy \right),$$

where λ_p is the probe beam wavelength, n is the plasma refractive index, *i.e.* a function of the plasma electron density, and L is the total path-length greater than the plasma extent along y . For a plasma with cylindrical symmetry around the x -axis, once the phase shift is recorded from interferograms like that of fig. 38, the electron density can be calculated by using Abel inversion techniques. Therefore we have

$$(5.2) \quad n_e(r, x = x_0) = - \frac{mc^2}{\pi e^2 \lambda_p r} \int_r^{r_0} \left(\frac{d}{dz} \Delta\varphi_{x_0}(z) \right) \frac{dz}{\sqrt{z^2 - r^2}},$$

where e and m are the electron charge and mass, respectively, and c is the speed of light and r_0 is the radial plasma size. On the other hand, the interferogram intensity pattern can be written in the following form:

$$(5.3) \quad I(x, z) = a(x, z) + [c(x, z) \exp[2\pi i f_u x] + \text{c.c.}],$$

where $c(x, z) = (1/2) b(x, z) \exp[i \Delta\varphi(x, z)]$ and its complex conjugate $c^*(x, z)$ carry the information concerning $\Delta\varphi(x, z)$; $a(x, z)$ and $b(x, z)$ account for non-uniformities of the background intensity and the fringe visibility; f_u is the spatial frequency of the unperturbed fringe pattern. It can be shown that, with appropriate assumptions on the distribution in the frequency domain, the phase shift can be directly extracted from the Fourier transform of the interferogram intensity pattern. The surface plot of fig. 39 shows the phase shift obtained using this analysis from the interferogram of fig. 38.

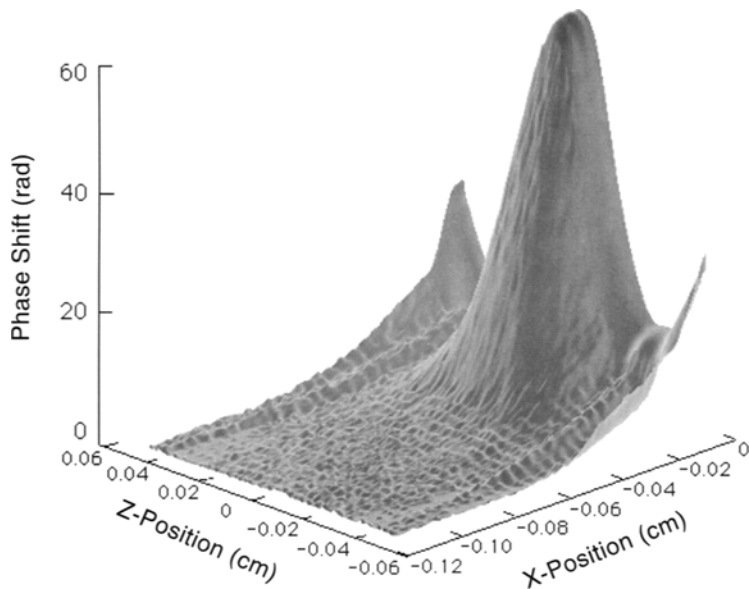


Fig. 39. – Three-dimensional shaded surface of the phase shift distribution induced by the preformed plasma, 4.3 ns after the peak of the heating laser pulses. The phase shift was obtained [10] from the interferogram of fig. 38 using a fast-Fourier-transform-based analysis technique [118].

5.3.4. Electron density profiles. Finally, the phase shift distribution shown above is fed into eq. (5.2) to obtain the electron density. A contour plot of the resulting plasma density profile is shown in fig. 40.

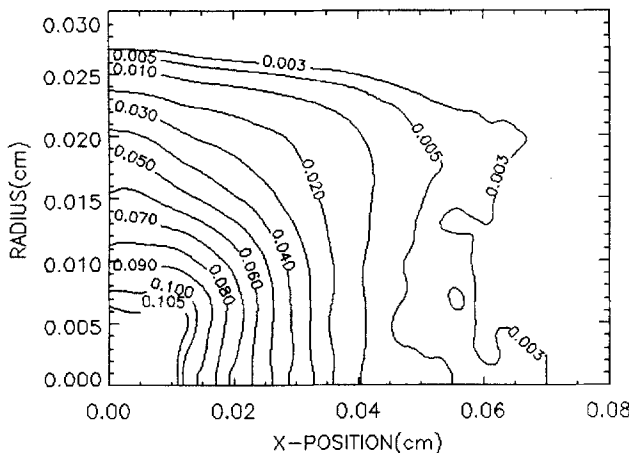


Fig. 40. – Contour plot of the electron density profile of the plasma, 4.3 ns after the peak of the plasma-forming pulses as obtained from Abel inversion of the phase shift distribution of fig. 39. Contour levels are labelled in units of the critical density at $1.053 \mu\text{m}$.

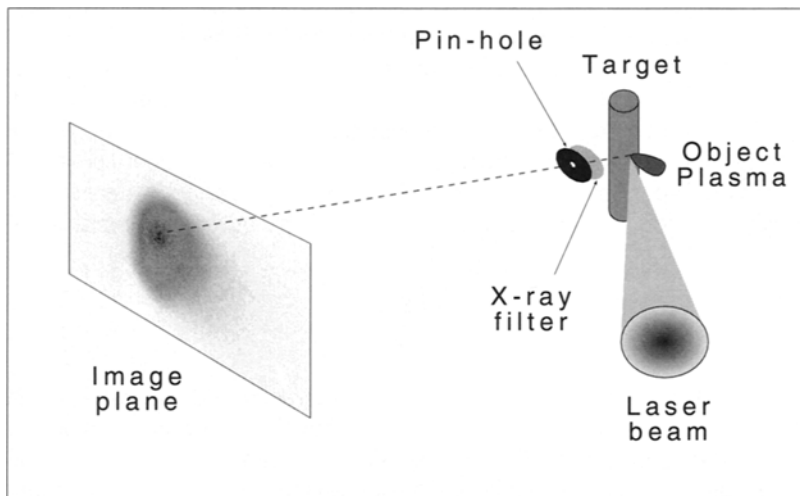


Fig. 41. – Geometry of a pin-hole camera for X-ray imaging of plasmas. The pin-hole diameter determines the spatial resolution of the image. In the limit of high magnification the spatial resolution of the image in the object plane is simply given by the pin-hole diameter.

The contour levels in fig. 40 are labelled in units of the critical density at $1 \mu\text{m}$ and, consistently with the assumption of cylindrical symmetry, the z -coordinate has been replaced by the radial coordinate. Plots like that of fig. 40 taken at different times during plasma expansion make it possible to determine the temporal evolution of the plasma density. This information is of fundamental importance to evaluate re-absorption effects of X-ray emission when determining the electron temperature of the plasma.

5.4. X-ray imaging of plasmas. – X-ray imaging of laser plasmas is a fundamental diagnostic tool that enables a direct monitoring of important characteristic parameters. In this section we describe the basic techniques of X-ray imaging of laser plasmas along with typical applications to the study of micron-sized sources. A method for obtaining time-resolving imaging with high spatial resolution is also discussed and an example of application of such method to Inertial Confinement Fusion related studies is also given.

5.4.1. Basic X-ray imaging techniques. Due to the strong X-ray emissivity of laser produced plasmas, a simple imaging device consisting of a pin-hole camera (PHC) can be employed to obtain X-ray images. Such images can be recorded directly by using X-ray-sensitive detectors (X-ray films, CCD cameras) or by employing phosphor screens coupled to optical image intensifiers. Presently available intensifiers based on micro-channel-plate technology (MCP) [122] can easily provide a thousand-fold overall gain in intensity [123]. Ordinary CCD cameras or commercial photographic B&W film can then be used to record intensified images.

Both magnification and resolution of a PHC can be easily calculated from simple geometrical consideration. According to the geometry of fig. 41 the magnification of a pin-hole camera is given by $A = q/p$, q and p being the pin-hole to image-plane distance

and pin-hole to object plane, respectively. The spatial resolution of the image is generally given by the combination of geometrical and diffraction effects.

It is easy to verify that the size of the image of a point source in the geometrical limit is given by $\Delta x_g \cong d_{ph}(1 + M)$, d_{ph} being the pin-hole diameter. According to the Fraunhofer diffraction theory [124], the typical transverse size, *i.e.* the diameter of the circle containing 85% of the total energy, of the Airy pattern produced by a uniformly illuminated circular aperture of diameter d_{ph} at a distance q , is $\Delta x_d \cong 2.44 q\lambda/d_{ph}$, λ being the X-ray wavelength. The best pin-hole size is given by the condition $\Delta x_g \approx \Delta x_d$, that is, by

$$(5.4) \quad d_{ph} = \sqrt{\frac{2.44 \lambda q}{1 + M}}.$$

For a typical set of parameters of laser-plasma experiments, $\lambda \approx 5 \text{ \AA}$, and $q \approx 50 \text{ cm}$, the best pin-hole diameter is approximately $7 \mu\text{m}$ for $M \approx 10$ and $5 \mu\text{m}$ for $M \approx 30$. On the other hand, a lower limit to the pin-hole size that can be employed in laser-plasma experiments is also set by the available X-ray flux as well as by the manufacturing feasibility of small diameter pin-holes. Typical commercially available pin-holes have diameters as small as $5 \mu\text{m}$. Therefore, for a magnification $M < 30$ the image resolution is determined by the geometrical limit. The size of the smallest feature which can be resolved in the object plane, *i.e.* in the plasma, is then

$$(5.5) \quad \Delta x_{\text{plasma}} \cong d_{ph} \left(1 + \frac{1}{M}\right).$$

In other words, in the limit of high magnification, the spatial resolution of a pin-hole camera image in the object plane is given by the pin-hole diameter. The pin-hole diameter also determines the X-ray flux collected by the camera.

According to the above geometry, the number of 1keV photons reaching the recording device per unit area of the magnified image can be written as follows:

$$(5.6) \quad \Phi_{1\text{ keV}} = 6.25 \times 10^{15} \frac{\eta_X E_L d_{ph}^2}{16 \pi q^2 M^2 A^2} \text{ photons/cm}^2,$$

where E_L is the laser energy absorbed by the plasma in joules, η_X is the X-ray conversion efficiency in the 1 keV region, d_{ph} and A are in μm and q is in cm. In the typical experimental conditions with nanosecond pulses the absorbed laser energy E_L ranges from several joules to hundred joules and the X-ray conversion efficiency in the 1 keV region is of the order of $\eta_X \approx 0.1$. With a plasma transverse size $A \approx 100 \mu\text{m}$ and assuming an image magnification $M = 10$, with a $10 \mu\text{m}$ pin-hole diameter and a pin-hole to image distance, $q \approx 50 \text{ cm}$, we obtain an X-ray flux ranging from 10^5 to $10^8 \text{ photons/cm}^2$, according to the variation of the absorbed laser energy.

This value should be compared with the flux required to obtain an optical density above fog $D = 1$ on a typical X-ray film [125], that is, approximately $\Phi_{1\text{ keV}} = 10^8 \text{ photons/cm}^2$. Therefore the use of an active (intensified) pin-hole camera becomes necessary in these experiments in order to cover the whole range of experimental conditions. The situation is different if specifically designed CCD arrays are used as direct X-ray detectors due to the higher efficiency resulting from the greater absorbing power as discussed in details in subsect. 5.5.2. Currently available CCD arrays equipped with cooling systems for the reduction of thermal noise are capable of

detecting the single X-ray photon. When these detectors are used, the spatial resolution can be pushed to the diffractive limit by using very small diameter (a few microns) pin-holes.

5.4.2. Spectral selection in X-ray imaging. Time integrated imaging is usually employed as a basic monitor of the laser-matter interaction process. However, when appropriate spectral selection is performed, valuable physical information can also be gained. To illustrate the role played by spectral selection in laser-plasma imaging we recall the results shown in fig. 15 concerning the size of LPP X-ray sources (see subsect. 4.5.3). In that experiment [76] the plasma was produced by the interaction of a 10 ps laser pulse with a layered target consisting of a solid plastic (Mylar) substrate coated with a $0.1 \mu\text{m}$ thick Al layer and over-coated with a $0.1 \mu\text{m}$ thick plastic (CH) layer. The laser beam focal spot, measured by direct obscuration, was $\approx 25 \mu\text{m}$ in diameter and the intensity was $3.6 \times 10^{16} \text{ W/cm}^2$. The X-ray images of the plasma shown in fig. 15 were obtained by using a pin-hole camera to study the interaction of a tightly focused, high-intensity picosecond laser pulses with solid targets. The PHC was fitted with a four-pin-hole array to allow a simultaneous 4-channel imaging as shown schematically in fig. 42a). Each channel was filtered to be sensitive to a different spectral region. One channel was filtered with a $20 \mu\text{m}$ thick Be filter, while the other three channels were additionally filtered with $3 \mu\text{m}$ Al, $8 \mu\text{m}$ Cu, and $3 \mu\text{m}$ Al + $8 \mu\text{m}$ Cu, respectively.

The transmittivity of the $25 \mu\text{m}$ Be, $3 \mu\text{m}$ Al and $8 \mu\text{m}$ Cu foil is plotted in fig. 42b) as a function of the X-ray photon energy in the range from 100 eV to 100 keV, calculated using available [126] mass absorption coefficients. Therefore, according to fig. 42b), the imaging channel filtered with the Be foil is mainly sensitive to photon energies above $\approx 1.5 \text{ keV}$. The addition of the Al filter in the second channel further shifts this lower bound to approximately 2.5 keV .

Figure 43 shows 1D lineouts of the X-ray images of fig. 15 for different filtering conditions. The profile obtained from the Be filtered channel is approximately $\approx 90 \mu\text{m}$ (FWHM), while the Be + Al and the Be + Cu both give a FWHM of $60 \mu\text{m}$ and the Be + Al + Cu channel gives a FWHM of $30 \mu\text{m}$. According to these results the extent of the X-ray-emitting region, in the case of the Be + Al + Cu channel, is slightly larger than the $25 \mu\text{m}$ diameter focal spot of the laser.

Since the main target component is Al, a strong contribution to the X-ray emission will come from Al resonance lines from He-like and H-like ions. The Al filter cuts off most of this emission, thus strongly reducing the X-ray source size as shown in fig. 43. The transmittivity of the second (Be + Cu) and the third (Be + Al + Cu) imaging channels are mainly determined by the transmittivity of the Cu foil. In this case the presence of the *L*-shell absorption at 933 eV selects photon energies between $\approx 6 \text{ keV}$ and 9 keV and greater than $\approx 15 \text{ keV}$. Therefore, with the Cu filter, only very energetic X-rays contribute to the image and the size of the X-ray source is found to be limited to the hot region of the plasma directly irradiated by the $25 \mu\text{m}$ diameter laser focal spot.

5.4.3. Time-resolving techniques. Temporal resolution can be achieved by forming the X-ray image generated by a PHC on a position-sensitive, time-resolving device. By using an X-ray streak camera, temporal resolution up to the picosecond range can be obtained. However, the spatial information is restricted to the direction perpendicular to the streak direction (1-D time-resolved imaging). This technique has

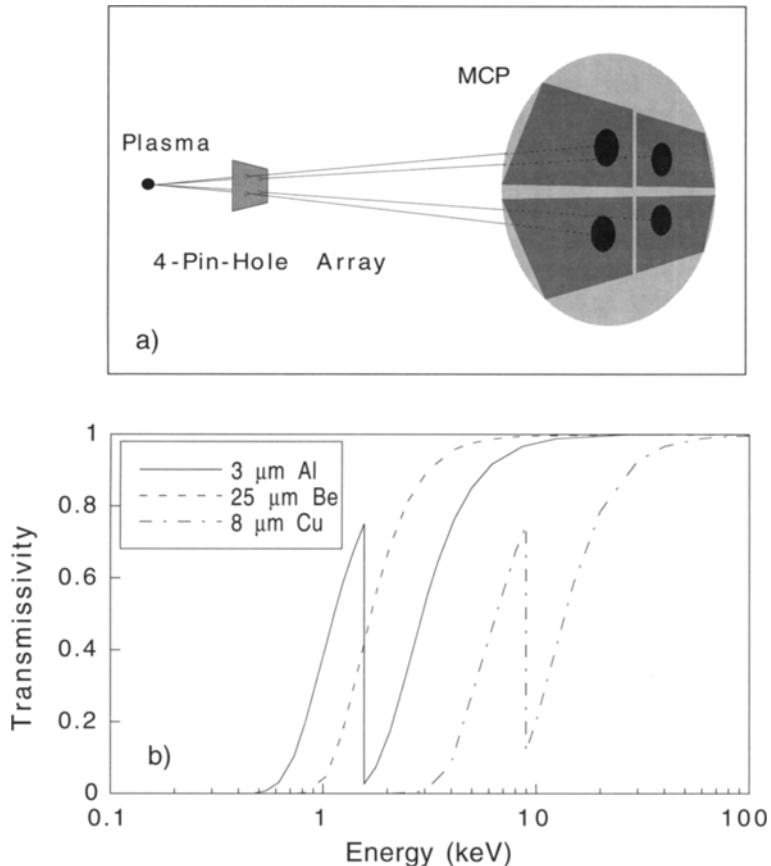


Fig. 42 – a) Schematic arrangement of a pin-hole camera fitted with a 4-pin-hole array to perform simultaneous 4-channel imaging of laser-produced plasmas; b) X-ray transmittivity of a $3\text{ }\mu\text{m}$ thick Al foil, a $25\text{ }\mu\text{m}$ thick Be foil and a $8\text{ }\mu\text{m}$ thick Cu foil calculated using tabulated mass absorption coefficients.

been employed for several years [121]. However, thanks to *micro-channel-plates* (MCP), two-dimensional position-sensitive devices with a temporal resolution of a few tens of picosecond are now available [123]. MCPs are characterised by a very low capacitance that enables fast switching of the externally applied electric fields. These devices can therefore be used as gated intensifiers as well as a DC intensifiers and usually do not require additional intensifiers due to their intrinsic high gain.

In all of the applications considered above, in order to avoid motional blurring of the images, framing times as short as few tens of picoseconds are often necessary. Recently, X-ray framing-times as short as 30–40 ps have been reported [127]. On the other hand, the scalelength of the features of interest may require high spatial resolution. Another important feature of such imaging systems is the number of frames that can be recorded on a single interaction event, so that the temporal evolution can be mapped with sufficient accuracy. The final configuration is therefore a trade-off between scientific requirements, spatial, temporal and spectral accuracy, on the one

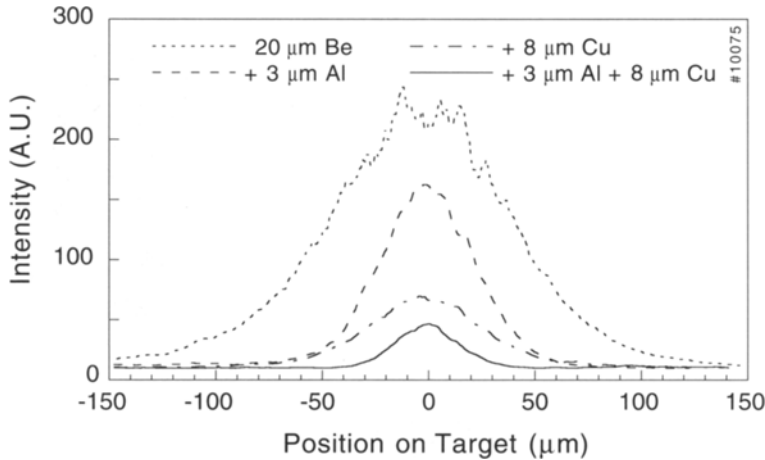


Fig. 43. – Lineout of X-ray images of fig. 15 obtained using a pin-hole camera fitted with a 4-pin-hole array. The plasma was produced by irradiating a solid plastic (Mylar) target coated with $0.1 \mu\text{m}$ thick Al layer, over-coated with a $0.1 \mu\text{m}$ thick palastic (CH) layer. The laser intensity was $3.6 \times 10^{16} \text{ W/cm}^2$ in a $\approx 25 \mu\text{m}$ diameter focal spot [76].

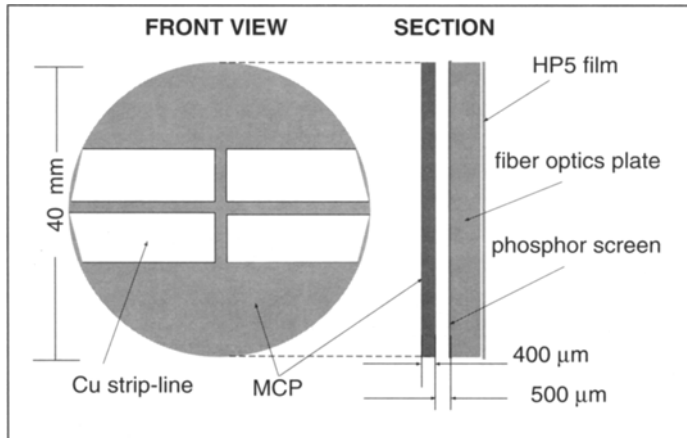


Fig. 44. – Schematic arrangement of the X-ray imager detection system with the MCP input surface showing the four 500 nm thick Cu-coated regions [128].

side, and flexibility, reliability, and ease of use, on the other side. In the following we briefly describe a technique employed [86] for fast, multiframe X-ray imaging of the interaction of a high-intensity laser pulse with preformed plasmas.

In this experiment, the X-ray detection unit, based on a MCP, enabled four independent X-ray imaging frames with 140 ps gate-time and adjustable interframe time. A diagram of the sensitive unit is shown in fig. 44. The input surface of the micro-channel-plate detector is coated with a 500 nm copper layer in four separated

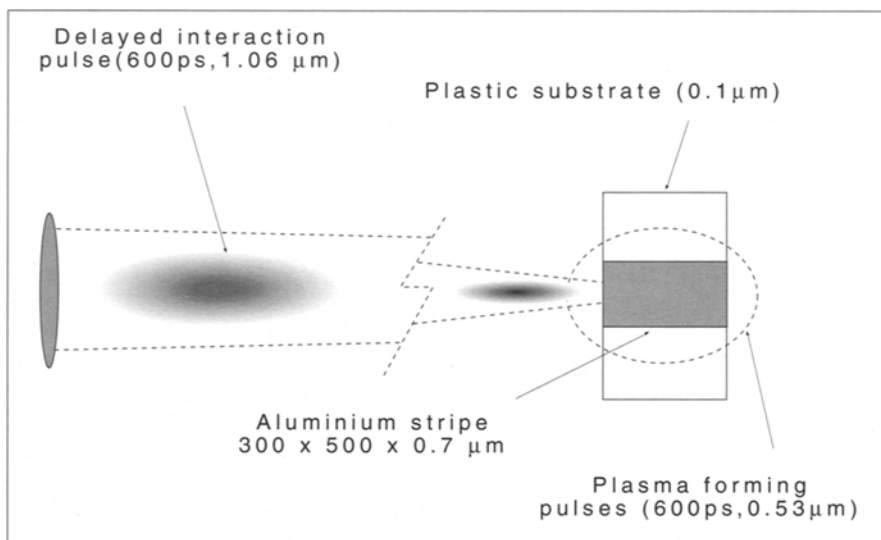


Fig. 45. – Target configuration and laser beams arrangement for the production of laser plasmas. The Al coating was 700 nm thick. The Al target was 300 μm wide and 500 μm long (along the interaction beam axis). The plasma, created by laser explosion of the foil, expands mainly in the direction perpendicular to the foil plane (not to scale).

rectangular regions (strip-lines) that acts as a photocathodes, while the output surface is uniformly coated with a thin copper layer.

Photons incident on one of the activated strip-lines generate photoelectrons that, accelerated by the external electric field, hit the walls of the micro-channel producing secondary electron emission. The electrons thus produced are then accelerated, multiplied and finally driven onto a phosphor screen by another electric field. A standard film records the light emitted by the phosphor screen and collected by a fibre optics bundle plate.

The unit is then coupled to a PHC equipped with a 4-pin-hole array capable of producing identical images of the plasma onto the four sensitive frames of the MCP. The X-ray radiation collected by the PHC is filtered in order to block visible radiation and to enhance the sensitivity of the detector to the spectral range of interest. In the case of the experiment described below, a thin ($\approx 1 \mu\text{m}$) Al filter was used to absorb most of the resonance line emission from He-like and H-like Al ions in favour of continuum emission, more closely related to the plasma conditions induced by local laser energy deposition.

5'4.4. An illustrative example of fast X-ray imaging. In this section we describe measurements carried out with the multi-frame X-ray imaging device described above to study the interaction of an intense laser pulse with a plasma pre-formed by a laser explosion of a thin Al stripe as shown schematically in fig. 45. The dashed ellipse around the Al coating shows schematically the size of the focal spot of the plasma-forming beams. A fifth laser interaction beam is then focused on the target along the longitudinal axis, as shown in fig. 45 and reaches the target typically 2.2 ns after the peak of the plasma-forming pulses, when a long plasma has developed.

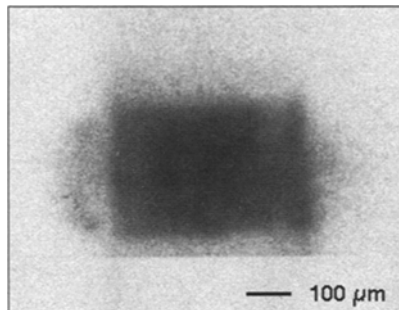


Fig. 46. – Time-integrated X-ray image of an Al stripe target heated on each side by a 600 ps, $0.53 \mu\text{m}$ laser pulses at an intensity of $\approx 2 \times 10^{13} \text{ W/cm}^2$. The 600 ps interaction pulse, delayed by 2.2 ns, was focused on the left edge of the target (as shown schematically in fig. 45) at an intensity of 10^{13} W/cm^2 . The image was obtained with the X-ray imager working as a DC X-ray intensifier [86].

Figure 46 shows a time-integrated X-ray image of the target heated on each side by the laser pulses at an intensity of $\approx 2 \times 10^{13} \text{ W/cm}^2$. In this case the imaging device was working as a DC X-ray intensifier. The delayed interaction pulse is focused on the (left) edge of the foil target at an intensity of 10^{13} W/cm^2 , in a $140 \mu\text{m}$ (FWHM) focal spot.

The shape of the bright X-ray emitting region, even though integrated in time, clearly resembles the shape of the Al heated target as shown in fig. 45 suggesting that most of the X-ray emission in the observed spectral range occurs during the plasma start-up phase, before hydrodynamic expansion takes place.

Consequently, in time-integrated images, the effects of the interaction occurring in the region of space occupied by the target prior to its explosion are masked by the intense X-ray emission occurring in the early stage of plasma formation. Therefore temporal resolution is needed to study the effects of the interaction pulse on the expanded plasma. Images like the one shown in fig. 46 are produced on each of the four frames of the imaging device and then, by driving the frames at different times, a temporal sequence of four X-ray images of the interaction region is recorded. A sequence of time resolved X-ray images is shown in fig. 47. In this case the target was heated at an incident laser intensity of $\approx 4 \times 10^{13} \text{ W/cm}^2$ on each side, while the intensity of the 600 ps delayed interaction pulse was $5.8 \times 10^{13} \text{ W/cm}^2$.

The first frame, synchronised with the peak of the plasma-forming laser pulses, shows X-ray emission from the plasma heating phase, while the remaining three frames show the X-ray emission due to the interaction of the delayed laser pulse with the preformed plasma. X-ray emission relative to the heating phase involves the whole Al target foil and, though very intense in the first frame, after $\approx 2 \text{ ns}$ drops below the detection level in the following frames. This is consistent with the history of X-ray spectra given in fig. 30 and fig. 32.

X-ray emission takes place again when the interaction pulse strikes the preformed plasma, making the interaction region “visible” in the X-rays. These results [86] indicate that a strong absorption of laser energy by the plasma takes place in this small region. Therefore, absorption processes like inverse bremsstrahlung and electron heat

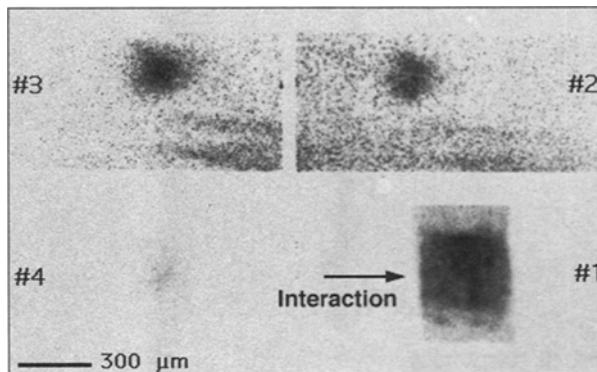


Fig. 47. – Sequence of time-resolved X-ray images of laser interaction with a preformed plasma produced by laser explosion of an Al stripe target. The delayed interaction beam was focused on the left edge of the plasma, as shown schematically by the arrow (see fig. 45), in a $140 \mu\text{m}$ (FWHM) focal spot at an intensity of $5.8 \times 10^{13} \text{ W/cm}^2$. The first frame, synchronised with the peak of the plasma-forming laser pulses, shows X-ray emission from the plasma heating phase, while the remaining three frames show the X-ray emission due to the interaction of the delayed laser pulse with the preformed plasma [86].

transport that account for absorption and propagation of the laser energy in the plasma can be investigated by studying the features of X-ray emission for different plasma and laser conditions.

5.5. Particles and high energy photons. – Beside X-ray emission originating from well-known emission mechanisms, laser-plasma interactions also give rise to the production of very energetic radiation, up to the gamma-ray region, as well as fast particles (electrons, ions). In ICF experiments, fast neutrons are also produced by nuclear reactions taking place in the compressed pellet. Depending upon the particular interaction regime, different particle acceleration mechanisms can take place as described below.

5.5.1. Ions, electrons and alpha-particles. Fast ions can escape from the plasma with high energy due to plasma hydrodynamic expansion and to ambipolar electric fields. The energy spectrum of ions consists of two components. The most intense component corresponds to thermal ions, whose velocity is of the order of the hydrodynamic expansion velocity (10^7 – 10^8 cm/s), while the weak component corresponds to the ions accelerated in the ambipolar field to velocities greater than 10^8 cm/s .

To measure the final velocity reached by the ions when they leave the plasma, time-of-flight techniques are usually employed. The method consists in recording as a function of time the ion current generated when the ions reach the collector surface of the detector. In order for this measurement to be accurate, the time of flight must be much greater than the characteristic ion emission time and the target-detector distance must be much greater than the ion source size. Laser-produced plasmas can be considered as a point source emitting an instantaneous burst of ions. In this case, considering a detector temporal resolution of 10 ns and a target-detector distance of 100 cm, the ion velocity is $\approx 10^8 \text{ cm/s}$ and can be measured with a relative error 1%.

The use of this technique requires several precautions. First of all, since the particle density scales as the inverse square of the target-detector distance the maximum distance is limited by the detector sensitivity. Secondly, since laser-plasmas are also sources of electrons, such measurements require the electron and ions components to be separated. This can be accomplished by using a metallic grid with a cell size smaller than the Debye length relative to the electron density at the detector position. Finally, if quantitative information on the parameters of the expanding plasma has to be obtained from time-of-flight detectors, the ion charge states has to be measured simultaneously. For this reason the time-of-flight detector is usually coupled with a mass spectrometer that enables the measurement of the average charge and relative atomic mass as a function of the velocity of the ions. Finally it should be emphasised that charge collector signals may be strongly influenced by the recombination in the expanding plasma [129]. This effect can be strongly reduced if a high vacuum is ensured in the flight region.

The particles emitted by laser irradiated targets can also be used to produce images of the source. Simple devices like pin-hole cameras (see subsect. 5'4) allow to obtain good spatial resolution. For instance, α -particle images of thermonuclear burn region of laser imploded D-T filled microspheres have been made [130]. Also, the angular distribution of fast ions emitted by the corona of spherical shell targets has been studied [131].

A powerful imaging technique for laser fusion experiments is the so-called zone plate coded imaging (ZPCI) [132]. The principle of this technique is the following. The source emits radiation which is registered by an appropriate position-sensitive detector. The information on the detector is coded by a plate with transparent and opaque areas chosen according to predetermined algorithms. The image is then unfolded using the known algorithm. Usually a Fresnel zone plate is used, so that the reconstruction process can be carried out rather simply with a laser beam. The most attractive features of this technique are its high radiation collection efficiency, the applicability to a broad class of incoherent radiation including γ -rays and the capability of producing three-dimensional images of the source.

Laser-produced plasmas are also important sources of free electrons. Electron emission can have thermal or non-thermal origin (see subsect. 3'2.6), depending on the physical mechanisms responsible for energy absorption during the laser-plasma interaction [133].

5'5.2. Hard X-rays and γ -rays from super-hot electrons. The energetic particles produced during laser-plasma interactions generate, via electromagnetic interaction with plasma particles, energetic electromagnetic radiation typically in the hard X-ray and γ -ray region. The most important mechanism responsible for the conversion of the particle kinetic energy in electromagnetic radiation is the bremsstrahlung (see subsect. 4'1.1). In addition, in the case of thermonuclear plasmas, *i.e.* in plasmas where nuclear reactions take place, γ -rays are directly produced by nuclear transitions.

The production of intense hard X-ray and γ -ray radiation is of particular interest in the interaction of intense, short and ultrashort laser pulses with plasmas. In fact, it has been shown that plasmas produced by ultrashort laser pulse interaction with solids [93] and gas jets [134] emit hard X-rays with photon energies extending beyond 1 MeV.

A recent experiment [44] has clarified the role of absorption mechanisms in the fs interaction regime showing that X-ray emission strongly depends on the polarisation of

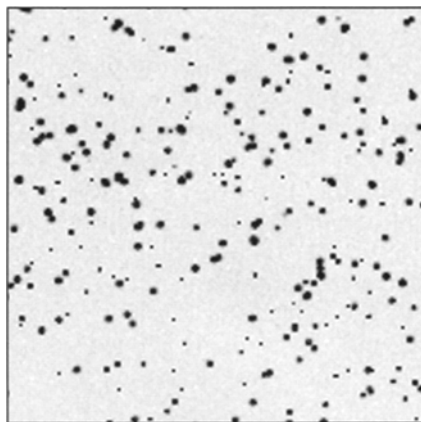


Fig. 48. – Output pattern produced by hard X-ray radiation on a single-photon detector based upon a low-noise, high-dynamic-range CCD array. The X-rays were generated by the interaction of a 150 fs laser pulse with a very thin ($0.1 \mu\text{m}$) plastic target at an intensity of $5 \times 10^{17} \text{ W/cm}^2$.

the incident laser light. In this experiment, hard X-ray spectroscopic measurements were carried out on a single laser interaction event by using a low noise, high dynamic range CCD detector working in a single photon measurement. The image of fig. 48 shows the pattern generated on the CCD by the radiation produced during the interaction of a 150 fs laser pulse with a very thin ($0.08 \mu\text{m}$) plastic target at an intensity of $5 \times 10^{17} \text{ W/cm}^2$. Each spot on the image corresponds to the capture of a photon with consequent production of charge.

Once the effect of low energy and light cut-off filters and the physics of interaction of X-ray photons with the detector have been taken into account, the charge distribution can be deconvoluted to obtain the photon spectral distribution. The histogram of fig. 49 shows the result of the analysis of the pattern of fig. 48 in terms of the number of photons detected in a given energy range as a function of the photon energy. Two distinct photon energy components are revealed by the measurement, a *thermal* one around the 1 keV region and a *hot*, intense component, peaked around 50 keV and extending up to the 100 keV region.

As already mentioned above, this study also provides a direct way of controlling the X-ray flux generated by an interaction event, based upon the control of a simple optical parameter, *i.e.* the polarisation of the incident laser pulse. In fact, as shown by the plot of fig. 50, the X-ray intensity in condition of *p*-polarisation was found to be approximately two orders of magnitude greater than in the case of *s*-polarisation. These results, together with the measurements on second harmonic emission [44] give a detailed understanding of the role played by absorption mechanisms and in particular by resonance absorption in the transfer of energy from the laser pulse to the target.

More recent experiments have shown that by using even shorter pulses, photons with MeV energies can be easily generated at high laser intensities. In fact, recent models predict a hot electron temperature, *i.e.* the characteristic temperature of the high-energy component of the electron distribution velocity, given by $T_h = mc^2(\gamma_{osc} - 1) \approx 0.511[(1 + I_{18}/1.37)^{1/2} - 1]$ MeV, where m and c are the electron mass and the velocity

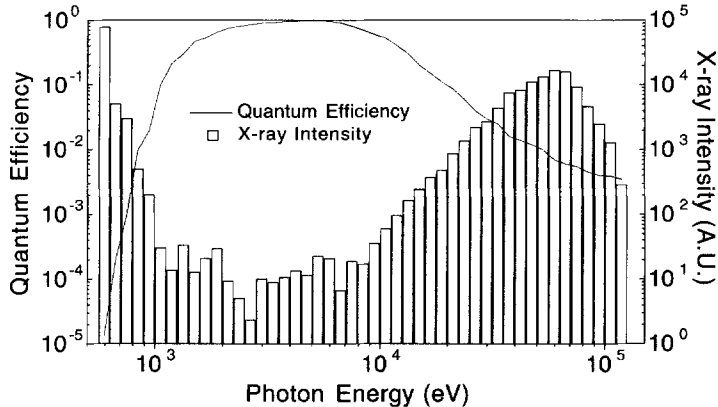


Fig. 49. – Histogram of the number of X-ray photons as a function of the photon energy obtained by the analysis of a single exposure of a CCD detector working in single-photon detection regime (see fig. 48). The quantum efficiency of the detector shown in the plot has been taken into account in the evaluation of the incident X-ray spectrum [44].

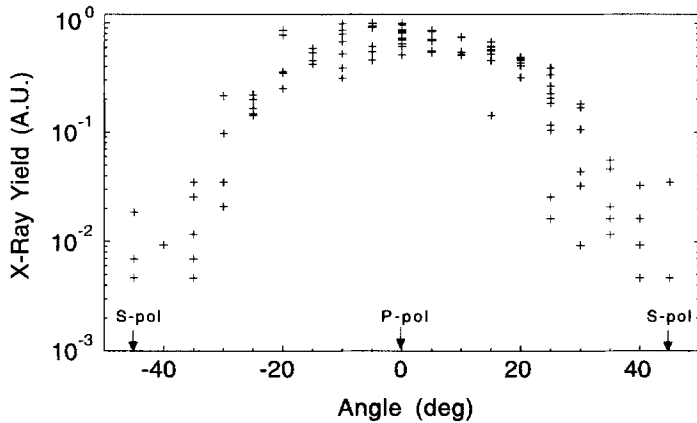


Fig. 50. – X-ray yield as a function of the polarisation of the 150 fs laser pulse incident on a 800 Å thick plastic target. The laser intensity on target was $5 \times 10^{17} \text{ W/cm}^2$. The polarisation of the laser light was varied gradually from *s* to *p* by rotating a half wave-plate placed on the incident beam, before the focusing optics [44].

of light, respectively, and γ_{osc} is the relativistic Lorentz factor of the electron oscillating in the laser electric field. In the numerical formula γ_{osc} is expressed in terms of I_{18} , i.e. the laser intensity in units of 10^{18} W/cm^2 . Recent measurements [49] of the photon spectrum in the MeV region performed using a 400 fs laser system at 1.06 μm focused onto solid targets at intensities greater than 10^{19} W/cm^2 show agreement with this prediction.

Finally we observe that very recent experimental measurements [53] on the interaction of high-contrast, ultrashort (30 fs) laser pulses with thin plastic foils, show evidence of the production of MeV photons even at lower laser intensities

(10^{18} W/cm²), suggesting that additional mechanisms may lead to enhancement of high energy photon generation [54].

6. – Applications

6.1. X-rays in science, technology and medicine. – Since their discovery a century ago, X-rays have played a very important role in many aspects of our lives. For example, through X-rays it is possible to reveal inaccessible details in biological structures and non-destructive characterisation of newly developed materials via X-rays is now routinely performed. More advanced X-ray spectroscopic and diffraction techniques enable matter to be probed at a microscopic level. The great advances of the last decades in the application of X-rays are due to the following aspects. Firstly, new X-ray production techniques have given rise to a wide range of sources with different physical properties. Secondly, thanks to the progress of material science, X-ray optics is now effectively enabling the manipulation of X-ray radiation in a fashion similar to conventional optics. In addition, X-ray detection and analysis techniques have developed dramatically so that X-ray imaging and spectroscopy with very fast temporal resolutions are commonly available.

From the point of view of laser-plasma sources, the recent advances in short pulse laser and X-ray optics technology is giving a great impulse to the application of fast X-ray analysis in medicine, biology, biophysics, material science, technology and electronics. The extension of high-power short laser pulses to the femtosecond regime now allows the production of hard X-rays and γ -rays up to the MeV region. On the other hand, grazing incidence, multilayer and zone plate optics are now widely used to concentrate X-rays or to perform high spatial/spectral resolution imaging. These advances make laser plasmas a flexible, inexpensive and high brightness X-ray source. In addition, due to the high repetition rate of presently available lasers, repetitive X-ray pulses with very high average power can be generated. X-ray lithography, time-resolved measurements in atomic and molecular physics, photochemistry and photobiology are examples of applications of such a regime. Most of these applications ask for techniques capable of working with X-rays in a regime as close as possible to the diffraction limit, either for flux concentration or for imaging purposes. X-ray microscopy comprises all these requirements and can be regarded as one of the basic and most promising application of X-rays.

6.1.1. X-ray microscopy. In principle, X-rays microscopy is capable of spatial resolutions comparable to that of electron microscopes, with the additional great advantage of much higher contrast [135]. In fact, high resolution (≈ 5 Å) can be achieved today by electron microscopes, but the small penetration depth of electrons and the weak dependence of attenuation lengths upon the atomic number require a complex preparation (thinning, heavy-metal staining, dehydrating). Such a pre-processing makes the observation technique somewhat indirect, since specimens cannot be studied in their natural environments. In contrast, X-rays are much more penetrating and the attenuation lengths are strongly dependent upon the atomic number. In fact, while electron beam and the atomic strength microscopes can only give surface information, soft X-ray microscopes allow information on a surface layer few wavelengths deep to be obtained.

In principle, the spatial resolution of X-ray microscopy compared to ordinary optical

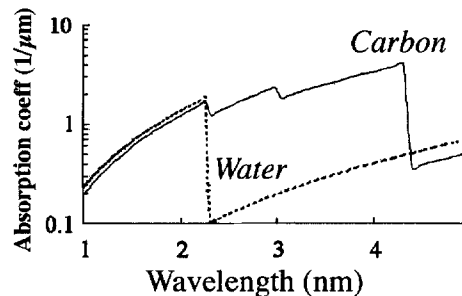


Fig. 51. – Absortion coefficients of carbon and water (oxygen) plotted as a function of the photon energy. The large difference between the absorption coefficients in the so called *water window* enables high-contrast imaging of biological samples.

microscopy can be higher by a factor $\lambda_{\text{opt}}/\lambda_X \approx 10^3$. In practice, present X-ray optics technology (Fresnel optics) is still far from such limit. Nevertheless, although the spatial resolution of an X-ray microscope is lower than that of an electron beam microscope or an atomic strength microscope, the use of X-rays to probe matter provides invaluable complementary information. For these reasons, there is a growing interest in radiation sources of high brightness in the soft and hard X-ray regime for applications in several fields of physics, material sciences, biology, and medicine.

The plot of fig. 51 shows the absorption coefficient as a function of the photon energy for elements of interest in biological and medical applications. The so-called water window ranges from the oxygen *K*-edge at 2.3 nm to the carbon *K*-edge at 4.4 nm.

According to fig. 51, photons in water window are much more effectively absorbed by carbon rather than by water. Therefore, this radiation is ideal for the observation of carbon-based organic compounds immersed in water, as in the case of the substructures of a living cell or other biological samples. This circumstances, together with the sufficiently high penetration depth, enable high-contrast X-ray imaging of micron-sized hydrated specimens.

6.1.2. Advantages of LPP X-ray sources. In general, laser-plasma X-ray sources provide unique advantages when high power, short pulse X-rays are needed or when accurate timing and/or synchronisation is required. Also, these sources are very advantageous in applications that require reduced capital costs compared to synchrotrons. Very important are the applications of laser-plasma X-rays in the radiography of the dense plasmas typical of inertial fusion experiments where picosecond timing is required along with large power and relatively energetic X-rays. Other applications that make use of a single X-ray pulse regime of high brightness include X-ray microscopy, X-ray fluorescence and radiography of biological systems [136]. Recently, the application of ultrashort pulse laser-generated hard X-rays to medical imaging and in particular to mammography and angiography, has been examined [137]. These studies show that, by using time-gated detection, scattered radiation can be strongly reduced [138] resulting in improved image quality with possibly reduced patient exposure.

On the other hand, the high brightness of laser plasma X-ray sources, joined to their short duration, makes these sources ideal for the radiography and X-ray

microscopy of micro-biological systems *in vivo* [139]. In fact, conventional X-ray sources do not allow the radiography of these systems to be performed, because the X-ray energy required for the detectors is so high that the micro-biological system is destroyed during the irradiation and its image on the X-ray detector results blurred. If a pulsed X-ray source is used whose pulse duration (≈ 1 ps) is much shorter than the characteristic time of hydrodynamic expansion (≈ 1 ns), the image will be clear because it is recorded before the “explosion” of the sample.

6.1.3. Progress in the design of LPP X-ray sources. One of the problems to overcome when using laser plasmas as radiation source is the effect of plasma debris ejected during the interaction. To this purpose several solutions have been proposed and implemented. A buffer gas transparent to the radiation of interest is used close to the plasma, which effectively stops the high-speed atomic debris particles due to momentum transfer in multiple collisions. Another method consists in using thin tape laser targets, which emit most of the debris safely backwards, while X-UV rear-side radiation is collected basically unaltered in the forward direction [113]. A third method involves the use of a fast rotating disc target [140] which adds additional side ward momentum to the larger debris particles, thereby creating an angular zone which is free from the harmful larger particles. Incidentally, this method is also promising for debris free laser deposition of thin films.

Finally, another scheme has been proposed [141] that consists in utilising a microscopic liquid droplet as target. It has been found that this technique enables the debris production to be reduced significantly. Firstly, the limited thickness of the target results in an elimination of the shock waves, typically generated in a solid bulk target, with consequent reduction of ejection of molten material from the surface. Secondly, since the whole target is ionised, the residual debris mainly consists of ions and atoms that can be easily stopped. These targets have been successfully employed (see [142] and references therein) for the generation of X-ray radiation applied to X-ray lithography and microscopy [143].

6.1.4. Examples of applications of LPP X-rays. An important and promising application of laser plasmas is the microlithography. It consists of a shadow printing process in which the fine features of an electronic circuit are transferred by X-ray exposure with a 1:1 magnification from a mask to the resist-coated Si wafer. Since the minimum spatial features are essentially determined by diffraction effects of the radiation employed for the process, the use of X-ray radiation allows to reduce the dimension of such features by a factor of 10^3 with respect to optical radiation. As a consequence the density of the fine features on the Si wafer can increase by a factor 10^6 . This is a typical application in which a high-average-power laser plasma X-ray source driven by a high-repetition-rate laser may be preferred to a synchrotron source, due to its lower capital cost. Recently, extreme UV [140] and soft X-ray [144] lithography have demonstrated the possibility of producing resist structures as small as a tenth of a micron.

Recently, a collaboration [145] between the Rutherford Laboratory (UK), the University of Edinburgh, the Kings College (London) and Leica (Cambridge) has successfully employed the RAL X-Ray Source to produce by X-ray lithography a 200 nm gate structure in a field effect transistor as shown in fig. 52.

The RAL X-Ray source produced 100 mW of X-ray power at a wavelength of 1 nm by focusing a train of picosecond KrF laser pulses onto a copper tape target. The

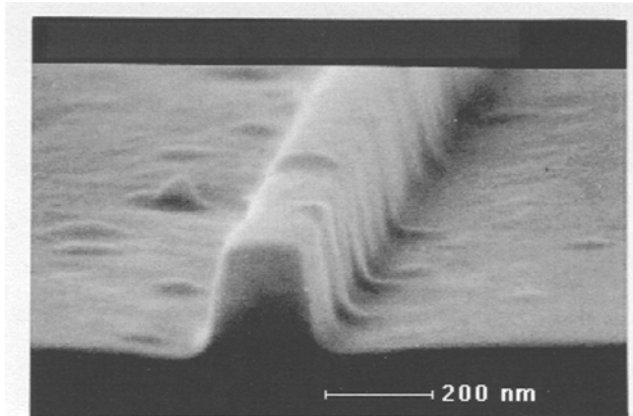


Fig. 52. – Patterned 200 nm doped polysilicon gate electrode produced by laser X-ray lithography. The X-ray lithography was carried out using 1:1 printing through an X-ray mask and employing the 1 nm X-ray source at RAL [145].

resulting device showed excellent performance and demonstrated that the laser-produced X-ray source is a credible candidate for the future 1 Gbit technology.

Laser-produced plasma X-rays have also been proposed [146] for standards and metrology applications in the soft-X-ray range. Figure 53 shows a schematic set-up of a reflectometer for measurement of X-ray reflectivity of samples. The X-ray radiation is generated by the interaction of a 8 ns, 10 Hz repetition rate, frequency-doubled Nd:Yag laser focused onto a rotating target at an intensity of approximately 10^{13} W/cm². The X-ray radiation is collected and collimated by a cylindrical mirror and sent onto a grazing incidence grating which selects the required photon energy to be relayed in the reflectometer chamber. Systems like this one can provide a continuously tunable source of radiation and are a convenient alternative to synchrotron radiation.

Special attention is being devoted recently to the possibility of using ultra-short, laser-plasma X-rays to probe fast chemical reactions. Ultrafast hard X-rays pulses (1.5 ps FWHM) from a laser-driven plasma have been used to probe [147] photo-induced dissociation of SF₆ molecules, detected by ultrafast near-edge X-ray absorption spectroscopy.

6.2. Main X-ray sources. – Present laser technology delivers table top high power laser systems capable of generating pulses ranging from several nanoseconds down to a few femtoseconds, *i.e.* over six orders of magnitude. In the ultrashort pulse regime, in particular, the power can easily be at the Terawatt level giving a power density at focus up to 10^{20} W/cm². From what discussed so far, it is clear that the properties of the X-ray source will be strongly dependent upon the particular regime, *i.e.* pulse-length and power density, chosen. These circumstances give to laser-plasma X-ray sources an enormous potential in terms of the flexibility of basic radiation source parameters like spectrum, duration, flux, size, etc. These properties should then be compared with the performances of other commonly used X-ray sources, namely conventional X-ray tubes and synchrotron radiation.

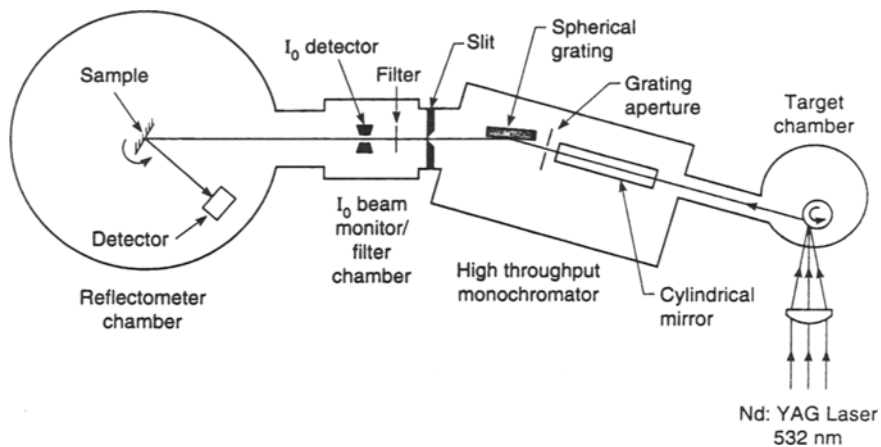


Fig. 53. – Schematic arrangement of a reflectometer based upon laser produced plasma X-ray source. The laser is focused upon a rotating target rod. The monochromator collects and selects the required photon energy [146].

6.2.1. X-ray tubes. In such tubes a beam of electrons, accelerated by electric fields up to tens of keV, impinges on a metal anode. The electron impact on the target produces bremsstrahlung continuum, and inner shell emission. The spectrum of the bremsstrahlung continuum essentially depends on the value of the accelerating electric potential, while the spectrum of the shell emission depends on the electric potential and the anode material. Up to the early fifties these incoherent X-ray sources have been the only available ones for research and applications. Today they are still employed in medical diagnostics and in applications that require a CW X-ray source.

The spectral brightness of these conventional X-ray tubes can vary over two orders of magnitude going from the traditional stationary-anode tube to the rotating-anode tube up to the brightest rotating-anode tube with micro focusing [148]. In addition, due to their spectral sharpness, line emission can overcome the continuum up to a factor of 10^4 . One way of characterising an X-ray source is to give the photon flux per unit solid angle in a bandwidth $\Delta\lambda/\lambda = 10^{-3}$. This is referred to as spectral brightness and is regarded as the most relevant figure of merit of an X-ray beam. For example, for the Cu K-shell emission a spectral brightness up to 10^{10} photons $s^{-1} mm^{-2} mrad^{-2}$ (0.1% bandwidth) $^{-1}$, can be reached in a conventional X-ray tube.

6.2.2. Synchrotron radiation. Synchrotron radiation was first observed as a parasitic emission from an electron synchrotron accelerator [149]. Since then many accelerator facilities have been built to provide this kind of radiation for scientific purposes and applications. The radiation is produced when electrons, forced to follow a circular path by means of magnetic fields, undergo a radial acceleration. The radiation emitted by an electron beam of relativistic energy circulating in ultrahigh vacuum is very powerful into the X-ray range. Moreover this radiation is strongly directional in the forward direction tangential to the electron orbit, and is highly polarised in the plane of the orbit. The natural radiation opening angle, in the plane perpendicular to

the orbit plane, is

$$\psi = \frac{m_0 c^2}{E} ,$$

where m_0 is the electron rest mass and E the beam energy. The horizontal divergence is determined by the width of the slit used to define the angle $\Delta\theta$ from which radiation is taken.

Synchrotron radiation facilities are usually built around storage rings in which an electron beam, pre-accelerated by a linear accelerator followed by a synchrotron accelerator, is injected and accumulated, up to a few hundred mA current. The storage ring is an ultrahigh vacuum tube consisting of arcs of circle joined by straight sections. In the turning points there are high magnetic field dipole bending magnets, which keep the electrons in their orbits. Light is generated at the turning points and is extracted through gaps in the magnet yokes. The radiation then impinges on a grazing incidence grating and the required frequency is selected by a slit and then used at the experiment station. In the straight sections of the ring there are RF cavities which provide the electron beam with the energy lost through radiation emission. The RF accelerating cavities produce the bouncing of the electron beam into short packets of current. So, synchrotron radiation is in the form of a train of pulses, typically 50–500 ps long, separated by a longer period, 2 ns–1 μ s, depending on the ring parameter.

The spectrum of the radiation extracted from a bending magnet is a continuum, similar to that of a black body. To characterise this spectrum it is useful to introduce a critical wavelength λ_c , defined as the wavelength which has half the emitted power above and half below it. The maximum of the emission is at $\lambda_{\max} = 2\lambda_c/3$ and, for a fully relativistic electron beam, the following relationships hold:

$$\lambda_c = \frac{20.7}{\varrho^2 B^2} , \quad B\varrho = \frac{E}{300} ,$$

where λ_c (nm) is the critical wavelength, ϱ (m) is the magnetic bending radius, B (T) is the magnetic bending field and E (MeV) is the electron energy. For typical values of a storage ring, $B = 1$ T, $\varrho = 5$ m, so the electron energy is $E = 1.5$ GeV, while the critical wavelength $\lambda_c = 0.8$ nm.

The quite large dimension (several metres in diameter) and cost of a conventional storage ring for synchrotron radiation make this source suitable only for large facilities. The use of a higher magnetic field (≈ 5 T) by means of superconducting magnets allows to reduce the size of the storage ring to a few metres in diameter. The reduced dimensions make this synchrotron radiation sources accessible also for smaller research laboratories.

In order to enhance the brightness in the X-UV region, periodic magnetic structures may be inserted in the straight sections of a storage ring in order to produce oscillations of the electron beam in the plane of its orbit. There are different types of structures and are referred to as the wavelength shifter, the wiggler and the undulator. The wavelength shifter consists of a three-pole magnet with a magnetic field much stronger than a bending magnet. As a consequence of the stronger magnetic field the critical wavelength is shifted to a shorter value, even if the source brightness stays the same. The other two insertion devices (wiggler and undulator), consist of multipole magnetic structures that induce several oscillations on the electron beam and are

capable of increasing the source brightness. In the case of a wiggler the process of radiation amplification is incoherent and therefore the brightness is $2N$ times higher than that a single bending magnet, where N is the number of the magnet periods. The brightness of undulators can be enhanced by a factor up to N^2 compared with a single bending magnet of the same magnetic field. In addition the undulator radiation is highly collimated and is almost laser-like. As an indicative example of brightness, we consider the radiation from a synchrotron source [150]. Typical values of the spectral brightness, in the energy range 0.1–5 keV, are 10^{15} photons $\text{s}^{-1} \text{mm}^{-2} \text{mr}^{-2}$ (0.1% bandwidth) $^{-1}$ for the bending magnet source, 10^{16} for the wiggler, 10^{17-18} for the undulator.

6.2.3. Comparison of X-ray sources. Until a few years ago, laser-produced plasma X-ray sources were regarded as the brightest pulsed sources while synchrotron radiation, due to their high-repetition-rate available, were considered the sources with the highest time-averaged brightness [151, 1]. Due to the dramatic increase of the repetition rate of presently available ultrashort laser systems, the average power of laser plasma X-ray sources is also increasing rapidly and is becoming more and more competitive. In addition, the combination of high-power and short-pulse durations makes it possible to extend the emission of LPP sources to the high photon energy, *i.e.* in a region inaccessible to both synchrotrons and conventional X-ray tubes. On the other hand, the peak laser power accessible today and the recent discovery of new X-ray generation mechanisms including high order harmonics from gas jets and solids, offer a unique tool for generating the brightest pulses of coherent, soft X-ray emission.

Clearly, the X-ray sources described above are characterised by different properties and therefore a direct comparison cannot be made. However, it is instructive to compare the average and peak spectral brightness of these sources in the spectral range from $1-10^6$ eV. Figure 54 shows schematically the regions of average brightness *vs.* photon energy for different sources. The boxes labelled “undulators” and “bending magnets and wigglers” represents schematically the output features of several installations including the European Synchrotron Radiation Facility (Grenoble, France), the Advanced Light Source (Lawrence Berkeley Laboratory, USA) [150] and the National Synchrotron Light Source (BNL, Brookhaven, NY, USA).

The parameters of standard laser-produced plasma X-ray sources are those typical of European laboratories including the X-ray and UV Laboratory at Rutherford Appleton Laboratory (UK), the Laser Plasma X-UV source at the FOM Institute for Atomic and Molecular Physics (The Netherlands). In these cases high-average-power KrF excimer laser beams (*e.g.*, 100 W average power, $\approx 1\text{J}$, ≈ 10 ns pulses at ≈ 100 Hz repetition rate) are focused onto high- Z target (*e.g.* W or Au) at a peak pulse irradiance of $I \approx 10^{12}$ W/cm 2 . Finally, the box corresponding to X-ray emission from fs interactions refers to the results obtained in recent experiments [93, 52, 106, 152] performed using femtosecond Ti:Sapphire lasers operating in laboratories world-wide and in European laser facilities including the Laboratoire d’Optique Appliquée ENSTA (France) and the Lund Institute of Technology (Sweden). In general we can say that the average brightness of continuum and line emission from laser plasmas is several orders of magnitude higher than the corresponding emission from conventional X-ray tubes. The storage ring source is sizeably brighter than standard laser-plasma sources. If low repetition rate (≈ 10 Hz), multi TW femtosecond lasers are used, the emission shifts towards the higher energy. In this case, higher average brightnesses rely on the availability of higher (kHz) repetition rate lasers. In general, we can state that laser

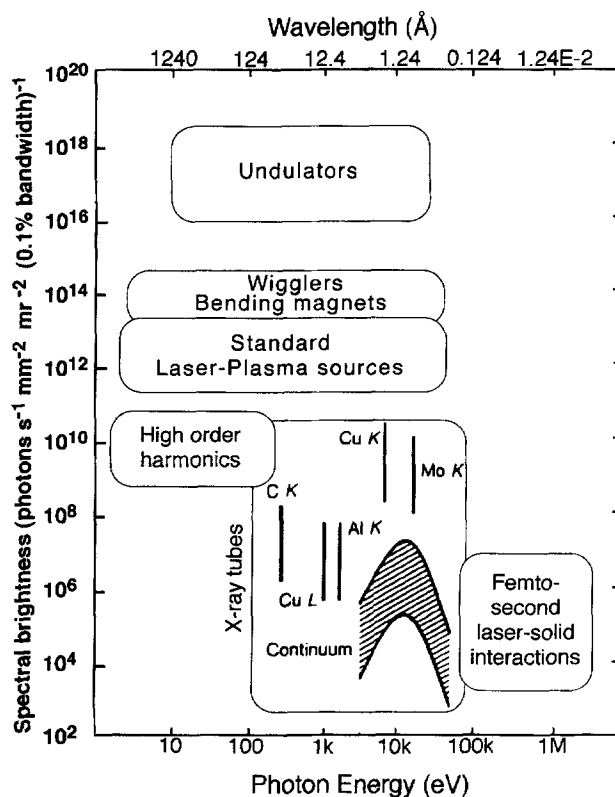


Fig. 54. – Schematic comparison of *average* spectral brightness for synchrotron radiation sources, conventional X-ray tubes and laser plasma X-ray sources including estimates from recent experiments with ultrashort pulses.

plasma X-ray sources are very attractive as a low-cost laboratory X-ray generators in the 1–10 keV spectral range and in particular when accurate (ps) synchronisation is required.

In the pulsed regime the X-ray tubes show a peak spectral brightness several orders of magnitude lower than the other available sources. As shown in fig. 55, the peak spectral brightness of laser-plasma continuum exceeds that from the bending magnet source, while the undulator brightness is still greater than X-ray emission from laser-produced plasmas. Line emission from laser plasmas becomes competitive with the corresponding undulator emission over a wide range of photon energies. The plasma X-ray laser is the brightest source in the soft X-ray region, being orders of magnitude brighter than both undulator emission and high-order harmonics. The latter however, is the brightest source of coherent, soft X-ray radiation easily accessible on a laboratory scale. It is orders of magnitude higher than both laser-plasma X-ray continuum and line emission at wavelengths shorter than 100 Å. In fact, in this spectral range, the lower intrinsic conversion efficiency of harmonics generation is largely compensated by their narrower bandwidth. Finally, femtosecond

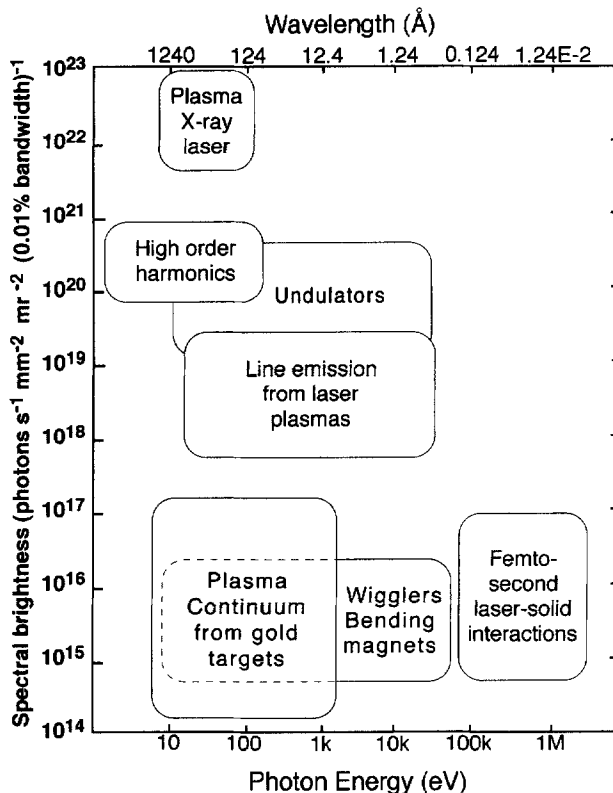


Fig. 55. – Schematic comparison of *peak* spectral brightness for synchrotron radiation sources, conventional X-ray tubes and laser plasma X-ray sources including estimates from recent experiments with ultrashort pulses.

laser-driven sources extend the parameter range of pulsed, ultrabright, hard X-ray sources to the MeV region.

7. – Conclusions

The interaction of intense laser light with matter is now widely recognised as the most versatile and promising way of generating intense pulsed X-ray radiation. The scale of presently available laser systems required to set up a powerful X-ray source in a small-size laboratory, has made it possible to conceive and develop a wide range of multidisciplinary applications. Further, the fast development of powerful lasers towards higher efficiency and compact designs is giving a strong impulse to the implementation of LPP X-ray sources in advanced industrial applications.

On the other hand, an intense activity is being devoted to this field by many laboratories world-wide within internationally coordinated programmes. These joint initiatives are continuously producing important scientific results. Hard X-ray emission and high-order harmonics from fs interactions are only examples of recent achievements of laser-matter interaction studies which represent a breakthrough in the field

of X-ray generation.

* * *

The authors acknowledge the support given by the colleagues of the Laser-Plasma Interaction Group in which they operate at Istituto di Fisica Atomica e Molecolare (CNR). In particular they are grateful to A. Giulietti for enlightening discussions and for his invaluable contribution to the manuscript. The authors also wish to acknowledge the role played by the TMR European Networks "Generation and Application of Ultra-Short X-ray Pulses" (GAUSEX, Contract N.ERBFMRXCT960080) and "Super Intense Laser Pulse-Solid Interactions" (SILASI, Contract N.ERBFMRXCT960043), to which they participate, in promoting and supporting advanced studies and applications of X-ray emission from laser-produced plasmas.

REFERENCES

- [1] O'NEIL F., in *Laser-Plasma Interactions 4, Proceedings of the 35th Scottish Universities Summer School in Physics*, edited by HOOPER M. B. (SUSSP publications, Edinburgh) 1989, p. 285.
- [2] MATTHEWS D. L. et al., *Phys. Rev. Lett.*, **54** (1985) 110.
- [3] MACKLIN J. J., KMETEC J. D. and GORDON III C. L., *Phys. Rev. Lett.*, **70** (1993) 766.
- [4] L'HUILLIER A. and BALCOU PH., *Phys. Rev. Lett.*, **70** (1993) 774.
- [5] KEY M. H., *Handbook of Plasma Physics*, edited by RUBENCHIK A. and WITKOWSKY S., Vol. 3 (North-Holland, Amsterdam) 1991, p. 575-611.
- [6] SPITZER L. jr. and HARM R., *Phys. Rev.*, **89** (1953) 977.
- [7] LONDON R. A. and ROSEN M. D., *Phys. Fluids*, **29** (1986) 3813.
- [8] CHRISTIANSEN J. P., ASHBY D. E. T. F. and ROBERTS K. V., *Comput. Phys. Commun.*, **7** (1974) 271.
- [9] RODGERS P. A., ROGOYSKI A. M., ROSE and S. J., Rutherford Appleton Laboratory Internal Report, RAL-89-127, (1989).
- [10] GIZZI L. A., GIULIETTI D., GIULIETTI A., AFSHAR-RAD T., BIANCALANA V., CHESSA P., SCHIFANO E., VIANA S. M. and WILLI O., *Phys. Rev. E*, **49** (1994) 5628.
- [11] BORGHESI M., GIULIETTI A., GIULIETTI D., GIZZI L. A., MACCHI A. and WILLI O., *Phys. Rev. E*, **54** (1996) 6769.
- [12] KRUER W. L., *Bull. Am. Phys. Soc.*, **21** (1976) 1048.
- [13] LANGDON A. B., *Phys. Rev. Lett.*, **44** (1980) 575.
- [14] DAWSON J. and OBERMAN C., *Phys. Fluids*, **6** (1963) 394.
- [15] KRUER W. L., *The Physics of Laser Plasma Interactions* (Addison Wesley, New York) 1988.
- [16] BRUNEL F., *Phys. Rev. Lett.*, **59** (1987) 52.
- [17] BALDIS H. A. in *Handbook of Plasma Physics*, edited by RUBENCHIK A. and SAGDEEV R. Z., Vol. 3 (North-Holland, Amsterdam) 1991, p. 361.
- [18] KRUER W. L., in *Laser-Plasma Interactions 3, Proceedings of the 29th Scottish Universities Summer School in Physics*, edited by HOOPER M. B. (SUSSP publications, Edinburgh) 1986, p. 79.
- [19] GIULIETTI D., BIANCALANA V., BATANI D., GIULIETTI A., GIZZI L., NOCERA L. and SCHIFANO E., *Nuovo Cimento D*, **13** (1991) 845.
- [20] GIZZI L. A., BATANI D., BIANCALANA V., GIULIETTI A. and GIULIETTI D., *Laser Part. Beams*, **10** (1992) 65.
- [21] GIULIETTI A., COE S., AFSHAR-RAD T., DESSELBERGER M., WILLI O., DANSON C. and GIULIETTI D., in *Laser Interaction and Related Plasma Phenomena*, edited by HORA H. and MILEY G. H., Vol. 9 (Plenum Press, New York) 1991, p. 261.

- [22] GIZZI L. A., BATANI D., BIANCALANA V., BORGHESI M., CHESSA P., DEHA I., GIULIETTI A., GIULIETTI D., SCHIFANO E. and WILLI O., in *Laser Interaction and Related Plasma Phenomena*, edited by HORA H. and MILEY G. H., Vol. 10 (Plenum, New York) 1992, p. 171.
- [23] GIULIETTI D., GIULIETTI A., LUCCHESI M. and VASELLI M. J., *Appl. Phys.*, **58** (1985) 2916.
- [24] AFSHAR-RAD T., GIZZI L. A., DESSELBERGER M., KHATTAK F. and WILLI O., *Phys. Rev. Lett.*, **68** (1992) 942.
- [25] EPPERLEIN E. M., *Phys. Fluids B*, **3** (1991) 3082.
- [26] EPPERLEIN E. M., *Phys. Rev. Lett.*, **65** (1990) 2145.
- [27] BIANCALANA V. et al., *Europhys. Lett.*, **22** (1993) 175.
- [28] GIULIETTI A., GIULIETTI D., BATANI D., BIANCALANA V., GIZZI L., NOCERA L. and SCHIFANO E., *Phys. Rev. Lett.*, **63** (1989) 524.
- [29] DRAGILA R. and GAMALIY E. G., *Phys. Rev. A*, **44** (1991) 6828.
- [30] SPITZER L., *Physics of Fully Ionized Gases* (Interscience, New York) 1962.
- [31] MALONE R. C., MC CRORY R. L. and MORSE R. L., *Phys. Rev. Lett.*, **34** (1975) 751.
- [32] MANHEIMER W. M. and KLEIN H. H., *Bull. Amer. Phys. Soc.*, **19** (1974) 920.
- [33] DENEEF C. P. and DEGROOT J. S., *Phys. Fluids*, **18** (1977) 1151.
- [34] FORSLUND D. W., KINDEL J. M. and LEE K., *Phys. Rev. Lett.*, **39** (1977) 284.
- [35] TABAK M., HAMMER J., GLINSKY M. E., KRUER W. L., WILKS S. C., WOODWORTH J., CAMPBELL E. M., PERRY M. D. and MASON R. J., *Phys. Plasmas*, **1** (1994) 1626.
- [36] STRICKLAND D. and MOUROU G., *Opt. Commun.*, **56** (1985) 216.
- [37] LE BLANC C., GRILLON G. et al., *Opt. Lett.*, **18** (1993) 140.
- [38] PERRY M. D. and MOUROU G., *Science*, **264** (1994) 917.
- [39] MULSER P., in *Laser-Plasma Interactions 5, Proceedings of the 45th Scottish Universities Summer School in Physics*, edited by HOOPER M. B. (SUSSP publications, Edinburgh) 1995, p. 231.
- [40] AUGST S., STRICKLAND D., MAYERHOFF D., CIN S. L. and EBERLY J., *Phys. Rev. Lett.*, **63** (1989) 2212.
- [41] PROTOPAPAS M., KEITEL C. H. and KNIGHT P. L., *Rep. Progr. Phys.*, **60** (1997) 389.
- [42] PESSOT M., MAINE P. and MOUROU G., *Opt. Commun.*, **62** (1987) 419.
- [43] MILCHBERG H. M. and FREEMAN R. R., *Phys. Rev. A*, **41** (1990) 2211.
- [44] GIZZI L. A., GIULIETTI D., GIULIETTI A., AUDEBERT P., BASTIANI S., GEINDRE J. P. and MYSYROVICZ A., *Phys. Rev. Lett.*, **77** (1996) 2278.
- [45] ROZMUS W. and TIKHONCHUK V., *Phys. Rev. A*, **42** (1990) 7401.
- [46] LEFEVRE E. and BONNAUD G., *Phys. Rev. Lett.*, **74** (1995) 2002.
- [47] WILKS S. C., KRUER W. L., TABAK M. and LANGDON A. B., *Phys. Rev. Lett.*, **69** (1992) 1383.
- [48] KODAMA R., TAKANASHI K., TANAKA K. A., TSUKAMOTO M., HASHIMOTO H., KATO Y. and MIMA K., *Phys. Rev. Lett.*, **77** (1996) 4906.
- [49] MALKA G. and MIQUEL J. L., *Phys. Rev. Lett.*, **77** (1996) 75.
- [50] WEIBEL E. S., *Phys. Fluids*, **10** (1967) 741.
- [51] MA G. and TAN W., *Phys. Plasmas*, **3** (1996) 349.
- [52] MATTE J. P. and AGUENOU K., *Phys. Rev. A*, **45** (1992) 2558.
- [53] GIULIETTI D., GIZZI L. A., GIULIETTI A., MACCHI A., TEYCHENNÉ D., CHESSA P., ROUSSE A., CHERIAUX G., CHAMBARET J. P. and DARPENTIGNY G., *Phys. Rev. Lett.*, **79** (1997) 3194.
- [54] TEYCHENNÉ D., GIULIETTI A., GIULIETTI D. and GIZZI L. A., submitted to *Phys. Rev. E*, **58** (1998) R 1245.
- [55] GRIEM H. R., *Plasma Spectroscopy* (McGraw-Hill, New York) 1964.
- [56] MARTIN G. A. and WIESE W. L., *J. Chem. Ref. Data*, **15** (1983) 537.
- [57] RILEY D., GIZZI L. A., KHATTAK F. Y., MACKINNON A. J., VIANA S. M. and WILLI O., *Phys. Rev. Lett.*, **69** (1992) 3739.
- [58] TONDELLO G., JANNITTI E. and MALVEZZI A. M., *Phys. Rev. A*, **16** (1977) 1705.
- [59] BAYANOV V. C., GULIDOV S. S., MAK A. A., PEREGUDOV G. V., SOBELMAN I. C. M., STARIKOV A. D. and CHIRKOV V. A., *JETP Lett.*, **33** (1976) 183.

- [60] McWHIRTER W. P., in *Plasma Diagnostic Techniques*, edited by HUDDLESTONE R. H. and LEONARD S. L. (Academic Press Inc., London) 1965.
- [61] MEWE R., in *Astrophysical & Laboratory Spectroscopy, Proceedings of the 33rd Scottish Universities Summer School in Physics*, edited by BROWN R. and LANG J. (SUSSP publications, Edinburgh) 1988, p. 129.
- [62] VAN DER SIJDE B. and VAN DER MULLEN J. A. M., *J. Quantum. Spectros. Radiat. Transfer*, **44** (1990) 39.
- [63] LEE R. W., WHITTEEN L. and STOUT II R. E., *J. Quant. Spectr. Radiat. Transfer*, **32** (1984) 91.
- [64] LOTZ W., *Z. Phys.*, **220** (1969) 486.
- [65] SIGEL R., *Handbook of Plasma Physics*, edited by RUBENCHICK A. and WITKOWSKY S. (North-Holland) 1991.
- [66] KUNZE H. J., in *Astrophysical & Laboratory Spectroscopy, Proceedings of the 33rd Scottish Universities Summer School in Physics*, edited by BROWN R. and LANG J. (SUSSP publications, Edinburgh) 1988, p. 187.
- [67] DUSTON D., CLARK R. W. and DAVIS J., *Phys. Rev. A*, **31** (1985) 3220.
- [68] EIDMANN K. and KISHIMOTO T., *Appl. Phys. Lett.*, **49** (1986) 377.
- [69] ROSEN M. D., *Proc. SPIE*, **1229** (1990) 160.
- [70] CELLIERS P. and EIDMANN K., *Phys. Rev. A*, **41** (1990) 3270.
- [71] LANDEN O. L., CAMPBEL E. M. and PERRY M. D., *Opt. Commun.*, **63** (1987) 253.
- [72] MURNANE M., KAPTEYN H. C. and FALCONE R. W., *Phys. Rev. Lett.*, **62** (1989) 155.
- [73] TOOMAN T. P., *Proc. SPIE*, **664** (1986) 186.
- [74] DAVIS G. M., GOWER M. C., O'NEILL F. and TURCU I. C. E., *Appl. Phys. Lett.*, **53** (1988) 1583.
- [75] MURNANE M., KAPTEYN H. C., ROSEN M. D. and FALCONE R. W., LLNL preprint, UCRL-JC-104870 (1990).
- [76] GIZZI L. A., *Ph. D. Thesis*, University of London, 1994.
- [77] KAUFMANN R., *Handbook of Plasma Physics*, edited by RUBENCHICK A. and WITKOWSKY S., Vol. 3 (North-Holland, Amsterdam) 1991.
- [78] GLIBERT K. M., ANTHES J. P., GUSINOW M. A., PALMER M. A., WHITLOCK R. R. and NAGEL D. J., *J. Appl. Phys.*, **51** (1980) 1449.
- [79] MOCHIZUKI T. and YAMANAKA C., *Proc. SPIE*, **733** (1987) 23.
- [80] KODAMA R., OKADA K., IKEDA N., MINEO M., TANAKA K. A., MOCHIZUKI T. and YAMANAKA C., *J. Appl. Phys.*, **59** (1986) 3050.
- [81] YAAKOBI B. et al., *Opt. Commun.*, **38** (1981) 196.
- [82] CHAKER M. et al., *Proc. SPIE*, **733** (1986) 58.
- [83] BATANI D., BIANCALANA V., CHESSA P., DEHA I., GIULIETTI A., GIULIETTI D. and GIZZI L. A., *Nuovo Cimento D*, **15** (1993) 753.
- [84] EIDMANN K. and SCHWANDA W., *Laser Part. Beams*, **9** (1991) 551.
- [85] NISHIMURA H. et al., *Phys. Fluids*, **26** (1983) 1688.
- [86] GIZZI L. A., GIULIETTI A. and WILLI O., *J. X-Ray Sci. Technol.*, **7** (1997) 186.
- [87] GIZZI L. A., MACKINNON A. J., RILEY D., VIANA S. M. and WILLI O., *Laser Part. Beams*, **13** (1995) 511.
- [88] BASTIANI S., GIULIETTI D., GIULIETTI A., GIZZI A., CECCOTTI T. and MACCHI A., *Laser Particle Beams*, **13** (1995) 493.
- [89] MACCHI M., GIULIETTI D., BASTIANI S., GIULIETTI A. and GIZZI L., *Nuovo Cimento D*, **18** (1996) 727.
- [90] GIULIETTI A., BENEDUCE C., CECCOTTI T., GIZZI L. A. and MILDREN R., to be published in *Laser Part. Beams* (1998).
- [91] ZOLENTS A. A. M. S. ZOLOTOREV M. S., *Nucl. Instrum. Methods A*, **358** (1995) 455.
- [92] MURNANE M. and KAPTEYN H. C., *Phys. Fluids*, **3** (1991) 2409.
- [93] KMETEC J. D., GORDON III C. L., MACKLIN J. J., LEMOFF B. E., BROWN G. S. and HARRIS S. E., *Phys. Rev. Lett.*, **68** (1992) 1527.

- [94] HAMSTER H., HAMSTER H., SULLIVAN A., GORDON S., WHITE W. and FALCONE R. W., *Phys. Rev. Lett.*, **71** (1993) 2725.
- [95] NICKLES P., SCHNUERER M., KALACHNIKOV M. and SCHLEGEL T., *Opt. Quantum Electron.*, **28** (1996) 229.
- [96] CHICHKOV B., MOMMA C., TUNNERMANN A., MEYER S., MENZEL T. and WELLEGEHAUSEN B., *Appl. Phys. Lett.*, **68** (1996) 2804.
- [97] SPIELMANN C., BURNETT N. H., SARTANIA S., KOPPITSCH R., SCHNURER M., KAN C., LENZNER M., WOBRAUSCHEK P. and KRAUSZ F., *Science*, **278** (1997) 661.
- [98] GODWIN R. P., *Appl. Optics*, **33** (1994) 1063.
- [99] ANDREEV A. A. et al., *Sov. Phys. JETP*, **74** (1992) 963.
- [100] SANPERA A., JONSSON P., WASTON J. B. and BURNETT K., *Phys. Rev. A*, **51** (1995) 3148.
- [101] CHANG Z., RUNDQUIST A., WANG H., MURNANE M. M. and KAPTEYN H. C., *Phys. Rev. Lett.*, **79** (1997) 2967.
- [102] MURNANE M., *Proceedings of the International Conference on Superstrong Fields in Plasmas, Varenna, Italy*, edited by LONTANO M. (AIP publish., New York) 1998.
- [103] WILKS S. C., KRUER W. L. and MORI W. B., *IEEE Trans. Plasma Sci.*, **21** (1993) 120.
- [104] VON DER LINDE D. et al., *Phys. Rev. A*, **52** (1995) R25.
- [105] GIBBON P., *Phys. Rev. Lett.*, **76** (1996) 50.
- [106] NORREYS P. A., ZEPF M., MOUSTAKIS S., FEWS A. P., ZHANG J., LEE P., BAKAREZOS M., DANSON C. N., DYSO A., GIBBON P., LOUKAKOS P., NEELY D., WALSH F. N., WARK J. S. and DANGOR A. E., *Phys. Rev. Lett.*, **76** (1996) 1832.
- [107] NISOLI M., STAGIRA, S., DESILVESTRI S., SVELTO O., SARTANIA S., CHENG Z., LENZNER M., SPIELMANN C. and KRAUSZ F., *Appl. Phys. B*, **65** (1997) 189.
- [108] MATTHEWS D. L. et al., *Nucl. Instrum. Methods B*, **98** (1995) 91.
- [109] LEWIS C. L. S., NEELY D., UHOMOIBHI J., O'NEILL D. M., RAMSDEN S. A., TALLENTS G. J., HADITHY Y. A., KEY M. H., ROSE S. J. and PERT G. J., in *X-ray Lasers 1990*, edited by TALLENTS G. J. (Adam Hilger, Bristol) 1991, p. 231.
- [110] MACPHEE A. G., BEHJAT A., CAIRNS G. F., HEALY S. B., KEY M. H., KIM N., KURKCUOGLU M. E., LAMB M. J., LEWIS C. L. S., MCCABE S. P., NEELY D., PERT G. J., PLOWES J., TALLENTS G. J., WARWICK P. J., WOLFRUM E. and ZHANG J., *IOP Conf. Ser.*, No. 151 (1996) p. 250-254.
- [111] ELTON R. C., *X-Ray Lasers* (Academic Press, London) 1990.
- [112] BUDIL K. S., PERRY T. S., BELL P. M., HARES J. D., MILLER P. L., PEYSER T. A., WALLACE R., LOUIS H. and SMITH D. E., *Rev. Sci. Instrum.*, **67** (1996) 485.
- [113] GIULIETTI D., BASTIANI S., CECCOTTI T., GIULIETTI A., GIZZI L. A. and MACCHI A., *Nuovo Cimento*, **17** (1995) 401.
- [114] NAKANO N., KURODA H., KITA T. and HARADA T., *Appl. Optics*, **23** (1984) 2386.
- [115] GIULIETTI A., GIULIETTI D., GIZZI L. A. and WILLI O., in *Spectral Line Shapes*, edited by ZOPPI M. and ULIVI L., Vol. 9 (AIP press, New York) 1997, p. 53-56
- [116] CHEVOKIN K., *Sov. J. Quantum Electron.*, **20** (1990) 1013.
- [117] HENKE B. L., LIESEGANG J. and SMITH S. D., *Phys. Rev.*, **19** (1979) 3004.
- [118] TAKEDA M., INA H. and KOBAYASKI S., *J. Opt. Soc. Am.*, **72** (1982) 156.
- [119] BENATTAR R., POPOVICS C. and SIGEL R., *Rev. Sci. Instrum.*, **50** (1979) 1583.
- [120] NOMARSKI M. G., *J. Phys. Radium*, **16** (1955) 95.
- [121] WILLI O., in *Laser-Plasma Interactions 4, Proceedings of the 35th Scottish Universities' Summer School in Physics*, edited by HOOPER M. B. (SUSSP publications, Edinburgh) 1989, p. 213.
- [122] WIZA L., *Nucl. Instrum. Methods*, **162** (1979) 587.
- [123] KILKENNY J. D., *Laser Part. Beams*, **9** (1991) 49.
- [124] BORN M. and WOLF E. *Principles of Optics* (Pergamon Press, London) 1970.
- [125] ROCKLETT D., BIRD C. R., HAILEY C. J., SULLIVAN D., BROWN D. B. and BURKHALTER P. G., *Appl. Optics*, **24** (1985) 2536.

- [126] HENKE B. L., GULLIKSON E. M. and DAVIS J. C., *At. Data Nucl. Data Tables*, **54** (1993) 181.
- [127] BRADLEY D. K., BELL P. M., LANDEN O. L., KILKENNY J. D. and OERTEL J., *Rev. Sci. Instrum.*, **66** (1995) 716.
- [128] Kentech Instruments Ltd. Hall Farm Workshops, Dideot (UK), Internal Report, 1992.
- [129] MATZEN M. K. and PEARLMAN J. S., *Phys. Fluids*, **22** (1979) 449.
- [130] SLIVINSKI V. W., BROOKS K. M., AHLSTROM H. G., STORM E. K., KORNBLUM H. N. and LEIPELT G. R., *Appl. Phys. Lett.*, **30** (1977) 555.
- [131] SLATER D. C., *Appl. Phys. Lett.*, **31** (1977) 196.
- [132] CEGLIO N. M. and COLEMAN L. W., *Phys. Rev. Lett.*, **39** (1977) 20.
- [133] SIGEL R., *Proceedings of the 20th Scottish Universities Summer School in Physics*, edited by CAIRNS R. A. and SANDERSON J. J. (SUSSP publications, Edinburgh) 1980, p. 661.
- [134] MODENA A., NAJMUDIN Z., DANGOR A. E., CLAYTON C. E., MARSH K. A., JOSHI C., MALKA V., DARROW C. B., DANSON C., NEELY D. and WALSH F. N., *Nature (London)*, **377** (1995) 606.
- [135] ARISTOV V. V. and ERKO A. C. (Editors) *X-Ray Microscopy IV* (Chernogolovka, Russia) 1994.
- [136] TILLMAN C., MERCER I., SVANBERG S. and HERRLIN K., *J. Opt. Soc. Am. B*, **13** (1996) 1.
- [137] BARTY C. P. J., GORDON III C. L., LEMOUFF B. E., ROSE-PETRUCK C., RAKSI F., BELL P. M., WILSON K. R., YAKOVLEV V. V., YAMAKAWA K. and YIN G. Y., *Proc. SPIE - The International Society for Optical Engineering, SPIE*, **2523** (1995) 286.
- [138] GRÄTZ M., PIFFERI A., WAHLSTRÖM C. G. and SVANBERG S., *IEEE J. Quantum Electron.*, **2** (1996) 1041.
- [139] RAJYAGURU J. M., KADO M., RICHARDSON M. C. and MUSZYNSKI M. J., *Biophys. J.*, **72** (1997) 1521.
- [140] BIJKERK F., SHMAENOK L. A., SHEVELKO A. P., BASTIAENSEN R. K. F. J., BRUINEMAN C. and VAN HONK A. G. J. R., *Microelectron. Eng.*, **27** (1995) 299.
- [141] RYMELL L. and HERTZ H. M., *Opt. Commun.*, **103** (1993) 105.
- [142] BERGLUND M., RYMELL L. and HERTZ H. M., *Appl. Phys. Lett.*, **69** (1996) 1683.
- [143] MALMQVIST L., BOGDANOV A. L., MONTELIUS L. and HERTZ H. M., *J. Vac. Sci. Technol. B*, **15** (1997) 814.
- [144] BIJKERK F. *et al.*, *Microelectronic Eng.*, **30** (1996) 183.
- [145] TURCU I. C. E., ALLOT R. M., MANN C. M., REEVES C., ROSS I. N., LISI N., MADDISON B. J., MOON S. W., PREWETT P., STEVENSON J. T. M., ROSS A. W. S., GUNDLACH A. M., KOEK B., MITCHELL P., ANASTASI P., MCCOARD C. and KIM N. S., *J. Vac. Sci. Technol. B*, **15** (1997) 2495.
- [146] GULLIKSON E. M., UNDERWOOD J. H., BATSON P. C. and NIKITIN V., *J. X-Ray Sci. Technol.*, **3** (1992) 283.
- [147] JIANG Z., IKHLEF A., KIEFFER J. C., RAKSI F. and WILSON K. R., *Ultrafast Phenomena X*, edited by FUJIMOTO J., ZINTH W., BARBARA P. F. and KNOX W. H. (Springer-Verlag, Berlin) 1996, p. 274.
- [148] POTTS A. W., in *X-ray Science and Technology*, edited by MICHETTE A. G. and BUCKLEY C. J. (IOP Publishing, Bristol) 1993, p. 48-63.
- [149] ELDER F. R., GUREWITSCH A. M., LANGMUIR R. V. and POLLOCK H. C., *Phys. Rev.*, **71** (1947) 829.
- [150] Lawrence Berkeley Lab. Rep. No. PUB-5172 Rev. (1986)
- [151] KIRZ J. *et al.*, *X-Ray data booklet*, Lawrence Berkeley Lab. Rep. No. PUB-490 Rev. (1986).
- [152] SCHNÖRER M., KALASHNIKOV M. P., NICKLES P. V., SCHLEGEL TH., SANDNER W., DEMCHENKO N., NOLTE R. and AMBROSI P., *Phys. Plasmas*, **2** (1995) 3106.